relative to acoustic vibrations, shows that the peak is associated with an optical mode of vibration, in which the atoms of a unit cell vibrate "against" each other, relatively independently of other atoms.

Since the scattering from zirconium hydride is primarily the result of the hydrogen, the inelastically scattered neutrons that have gained energy from acoustic vibrations form a continuous spectrum typical of incoherent scattering. In this case, a gain of energy from an optical vibration can be easily identified if present, for only an optical mode can produce a sharp peak. Such a peak is observed with a sample of polycrystalline ZrH at 0.134 ev (Fig. 2) with an energy of ± 0.015 ev, of which ± 0.005 results from resolution and incident energy spread. The corresponding energy of the lattice vibration is $E=0.130$ ev. It is interesting to note that this transition, which is so prominent in the present measurements, does not appear in infrared absorption measurements. Further discussion of the ZrH results is contained in the accompanying Letter by Andresen, McReynolds, Nelkin, Rosenbluth, and Whittemore.

Thus the cold neutron energy gain technique appears to be a useful method of detecting optical lattice vibrations up to energies of about 0.25 ev, this limit being set by the characteristics of the present chopper. Experiments with other materials are planned to investigate the value of these measurements to solid state investigations.

* Work performed under contract with U. S. Atomic Energy Commission.

† On leave from Weizmann Institute, Rehovoth, Israel and the Israel Atomic Energy Commission.

[1] Carter, Palevsky, and Hughes, Phys. Rev. **106**, 1168 (1957).

[2] Pelah, Eisenhauer, Hughes, and Palevsky, Bull. Am. Phys. Soc. Ser. II, **2**, 43 (1957).

[3] A study of the scattering of cold neutrons from vanadium has been completed and will be submitted for publication shortly.

[4] We wish to thank H. P. R. Frederikse of the National Bureau of Standards and S. M. Christian of RCA laboratories for supplying single crystals of Ge for this measurement. A detailed analysis of the Ge data in cooperation with F. Herman of RCA is now under way.

Neutron Investigation of Optical Vibration Levels in Zirconium Hydride*

A. Andresen,† A. W. McReynolds, M. Nelkin, M. Rosenbluth, and W. Whittemore‡

John Jay Hopkins Laboratory for Pure and Applied Science, General Atomic Division of General Dynamics Corporation, San Diego, California

(Received October 2, 1957)

We have investigated certain properties of zirconium hydride by studying the spectrum of neutrons scattered elastically and inelastically from polycrystalline samples. A consideration of the zirconium hydride lattice shows that its thermal vibration spectrum should include in addition to the usual band

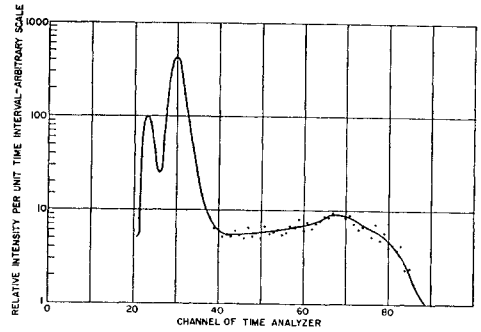

Fig. 1. Distribution of flight time for neutrons scattered by $ZrH_{1.5}$. Channel number 6 is zero time, each channel is 40 μsec, and flight path is 487 cm.

of acoustical frequencies also a sharp "optical" frequency, ν, corresponding approximately to vibrations of the individual hydrogen atoms in an isotropic harmonic well. This implies a set of optical energy levels for the lattice, $E_n = nh\nu$. Peaks corresponding to transitions between these optical energy levels are seen in Fig. 1, which shows the spectrum of neutrons scattered at 90° from zirconium hydride. The average incident energy was 0.004 ev. Measurements were made in collaboration with Pelah, Eisenhauer, Hughes, and Palevsky on the Brookhaven Laboratory slow chopper, which they described in the preceding Letter. The $ZrH_{1.5}$ sample for Fig. 1 was heated to 393°C to make evident the second level (Channel No. 23), as well as the first level (Channel No. 30). Still higher levels should exist but the equipment discriminates so severely against neutrons of these higher energies that the levels do not appear.

By transforming the coordinate from time of flight to energy, we obtain Fig. 2. From this figure, we can see the shape of the optical levels and their location as well as the acoustical Debye cutoff which occurs at about 0.02 ev. For comparison, we have shown the results obtained at $T=24$°C and 393°C. At 393°C the width of the first level at half its maximum value is about 0.037 ev. The Doppler broadening of the level due to simultaneous acoustical and optical transitions has been estimated to be 0.031 ev, a value about three

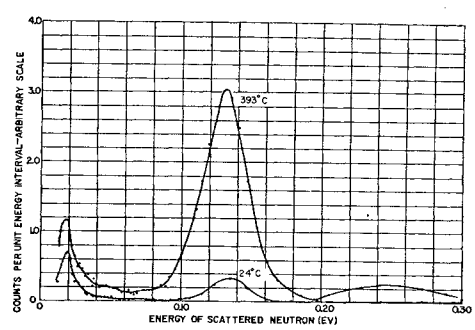

Fig. 2. Energy distribution of neutrons scattered by $ZrH_{1.5}$ at 90° angle. The average incident neutron energy is 0.004 ev.

times the instrumental resolution. The observed level is somewhat broader than these combined widths, but not significantly so. The level width is predicted to vary as $\sqrt{T}$, as it appears to do within the accuracy of the measurements.

To good accuracy, the population of the first level (and hence scattering from this level) varies with temperature according to the Boltzmann function $e^{-E/kT}$, where E is the energy of the level. In order to determine this energy, the intensity of the neutrons scattered from the first optical level has been measured as a function

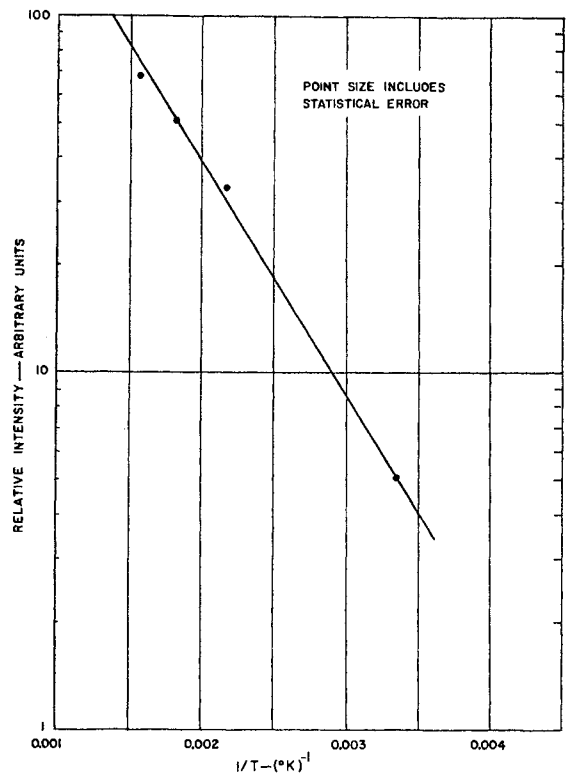

FIG. 3. Intensity of neutrons scattered from the optical level of $ZrH_{1.5}$ as function of sample temperature. Slope of curve gives optical energy level as 0.130±0.005 ev.

of temperature. These data are plotted in Fig. 3 and yield a value of $E=0.130\pm0.005$ ev.

The cross section for energy gain from the optical level can be readily calculated for a one-phonon process. This yields a cross section of about 0.9 barn at 24°C for neutrons incident with 0.004 ev. The experimental determination of this cross section for the present samples of zirconium hydride is rendered difficult because of the multiple scattering in the thick samples. From the data we can determine the ratio of the inelastic to the elastic cross section, taking account of the multiple scattering. Since one can assume that the elastic cross section for this case is 80 barns, we find that the total inelastic cross section is about 2 barns. Of this the experiment shows that between 35% to 50% is due to the optical level at 24°C. This yields a cross section of 0.7 to 1.0 barn in good agreement with the theoretical value.

* Experimental observations taken at the Brookhaven Nationa Laboratory.
† Present address: JENER, Kjeller, Norway.
‡ Guest Scientist, Brookhaven National Laboratory, Upton, New York.

Mechanism for Production of X-Rays by Ion Clouds Striking the Earth*

PAUL J. KELLOGG
University of Minnesota, Minneapolis, Minnesota, and the Naval Research Laboratory, Washington, D. C.
(Received July 25, 1957)

IN this letter we point out a mechanism, based on the Chapman-Ferraro[1,2] model for geomagnetic storms, for the production of x-rays in auroras, of energies comparable to those of the incoming protons.

We here give an argument which applies not to the initial stages of the phenomenon as discussed by Chapman and Ferraro, but to a steady state established sometime after the beginning of the phenomenon. For simplicity we consider a very large uniform cloud incident along the direction of the earth's magnetic axis. The mechanism will also clearly work for clouds incident in other directions, and also for clouds with nonuniform density. We neglect the thermal and turbulent motion of the cloud particles. If the density of the cloud is very low, then the particles will not affect each other, and the electrons and protons will follow the orbits investigated by Størmer. This means that the protons will be able to penetrate $(1836)^{\frac{1}{2}}$ times closer to the earth before being turned away by the earth's magnetic field. This situation is sketched (not to scale) in Fig. 1, where

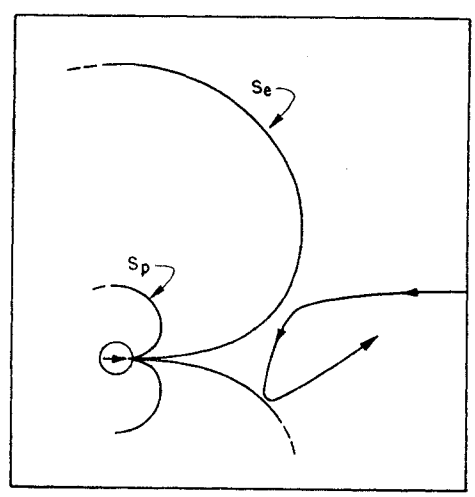

FIG. 1. Approach of electrons and positrons to the earth. For explanation see text.

Physica 120B (1983) 131–135
North-Holland Publishing Company

CRYSTAL ANALYSER TOF SPECTROMETER (CAT)

Susumu IKEDA and Noboru WATANABE
National Laboratory for High Energy Physics, Oho-machi, Tsukuba-gun, Ibaraki-ken, 305, Japan

Kenzo KAI
The Research Institute for Iron, Steel and Other Metals, Tohoku University, Sendai, 980, Japan

This paper reports the design and performance of a high resolution crystal analyzer spectrometer (CAT) which has been built and operated at KENS. Energy resolution of the instrument is $\Delta\varepsilon/\varepsilon = 0.02$–$0.03$ in the range of energy transfer $\varepsilon = 0.05$–1 eV. The local modes of hydrogen in various metallic hydrides have been measured by this spectrometer. Higher harmonics of the local modes have been observed, with their fine structure, up to 5th order for TiH_2, $ZrH_{1.41}$ and $ZrH_{1.93}$. Anharmonicity parameters of the hydrogen potential for $ZrH_{1.41}$, TiH_2 and $TaH_{0.1}$ (30 K) have been determined from their energy shifts relative to the harmonic values.

1. Instrument

A high resolution crystal spectrometer has been built and operated at KENS. The instrument makes it possible to measure incoherent neutron scattering with large energy transfer in the range $\varepsilon = 0.05$–1 eV, with a resolution of about $\Delta\varepsilon/\varepsilon = 0.02$–$0.03$ in the entire range of energy transfer [1]. The instrument is of inverted geometry type; the scattered neutrons are detected at a fixed energy by a large analyzer crystal, while the incident neutron energy is determined from the measured total time of flight, t, using the following relation:

$$t = \frac{L_i}{V_i} + \frac{L_f}{V_f}, \tag{1}$$

where L_i, L_f, V_i, and V_f are incident (i) and scattered (f) flight path lengths and neutron velocities, respectively.

In this type of spectrometer, generally speaking, uncertainty in the second term becomes large due to the finite extents of sample, analyzer and detector. This reflects on the first term through the relation (1) and results in the poor definition of the incident energy. If we put the sample and the detector on a plane, and set the analyzer parallel to this plane, then two-dimensional focussing is realized in time of flight between sample and detector [1]. This focussing geometry makes it possible to improve the energy resolution without sacrificing the geometric counting efficiency. A prototype spectrometer of this type was developed and operated at Tohoku linac [2–4]. In the new machine at KENS, signal-to-background ratio has been greatly increased with an improved energy resolution [1]. Momentum transfer Q is rapidly increased with energy transfer ε, due to the low final energy, but the spectrometer will be useful for the measurements of the local mode of hydrogens in metallic hydrides, for the molecular spectroscopy, etc., where the value of Q is not crucial and the Q-dependence not so important. Similar instruments were operated also at the pulsed neutron facilities of Harwell linac [5], ZING-P′ at Argonne [6], and WNR, at Los Alamos [7].

Fig. 1 shows the spectrometer configuration. The instrument has been installed at H-7 beam hole which views the surface of a moderator (polyethylene slab at room temperature) perpendicularly. Maximum beam size at the sample position is $7\,\mathrm{cm}^{W} \times 7\,\mathrm{cm}^{H}$. In order to minimize the ambiguity of the incident flight path length, a

0378-4363/83/0000–0000/$03.00 © 1983 North-Holland and Yamada Science Foundation

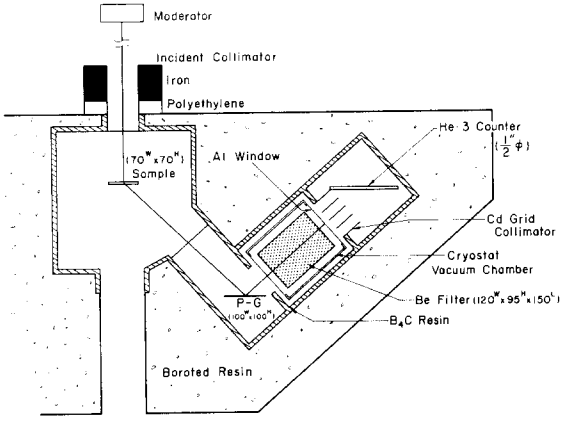

Fig. 1. Configuration of spectrometer (CAT).

plane sample is set perpendicular to the beam at $L_1 = 5.299$ m. The analyzer crystal is a 10 cm × 10 cm pyrographite (mosaic spread 1.2°). A Bragg angle of $\theta_B \sim 43°$ is used, and the (002) reflection corresponds to $E_f = 4$ meV. Eight He-3 proportional counters, 1/2 inches in diameter and 12 inches in active length filled to 20 atm pressure, are set horizontally to form a detector plane. In the present configuration, the center-line distance between sample and analyzer, and that between analyzer and detector are 36 cm respectively which correspond to inter-plane distance $a = 24.2$ cm. A beryllium filter ($9.5\,\mathrm{cm}^H \times 12\,\mathrm{cm}^W \times 15\,\mathrm{cm}^L$) cooled to liquid-nitrogen temperature is used between analyzer and detector with a post cross collimator made of cadmium, in order to eliminate neutrons due to higher order reflections. Sample–analyzer–detector system is buried in a shield box of 2-cm-thick B_4C and 25-cm-thick borated resin wall.

Extensive studies of the energy resolution were performed by a Monte Carlo computer simulation for a sample–analyzer–filter detector system. Fig. 2(a) shows the effect of the mosaic spread, β, in the analyzer crystal on the time distribution of the scattered neutrons. This indicates that mismatch in time focussing due to the finite value of β is not significant in this spectrometer. The most probable value of t_f is determined to be $t_f = 821$ μs from this result.

Fig. 2(b) shows the calculated energy spectrum of the scattered neutrons. The width is fairly

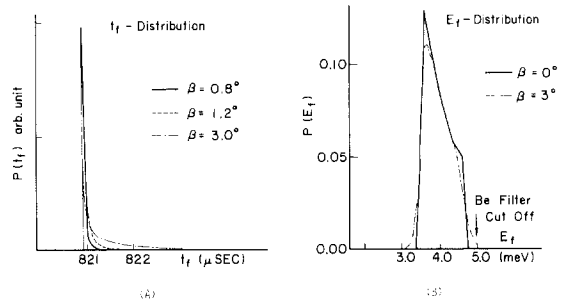

Fig. 2. Time distribution (a) and energy distribution (b) of detected neutrons.

wide which is consistent with the measurement, and from this distribution, the mean value of E_f is determined to be $\bar{E}_f = 3.9$ meV.

The effect of the finite size and circular cross section of the detector was also studied. Even with 1/2″ diameter counter, the effect seems significant, and if necessary we can improve the resolution by using a proper cadmium mask, with a sacrifice in counting efficiency of about 30%. Calculated values of the total resolution $\Delta\varepsilon/\varepsilon$ are shown in fig. 3 as a function of energy transfer ε, with partial contributions due to the finite thickness of detector, analyzer and sample, neutron pulse width from moderator, and so on.

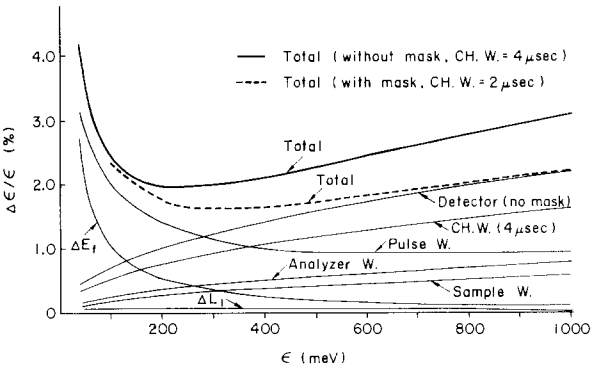

Fig. 3. Total and partial energy resolutions.

2. Measurements

In order to test the performance of the spectrometer, the local vibration mode of hydrogens in various metallic hydride samples has been

measured [1, 8, 11, 12]. In fig. 4(a) is shown a typical raw data of TOF spectrum obtained from TiH_2 at room temperature which demonstrates the extremely low background level compared to the results obtained at other laboratories. Even at the time corresponding to $\varepsilon = \infty$, background is low enough to observe a small step increase in the spectrum. Fig. 4(b) shows the energy spectrum which demonstrates the higher resolution of the instrument. Higher harmonics up to 5th order are clearly observed with their fine structures. It is obvious that the frequencies for higher harmonics are shifted by appreciable amounts from the respective harmonic positions, and from these frequency shifts we can determine the anharmonicity parameters of the hydrogen potential. $ZrH_{1.41}$ and $ZrH_{1.93}$ have been measured and the results are shown in fig. 5. In the fundamental peak of $ZrH_{1.93}$, there are two sub-peaks at about 138 and 145 meV with a shoulder at about 154 meV. The results are consistent with the reported values by Couch et al. [9]. There exists a distinct difference between the fine structures of $ZrH_{1.41}$ (cubic) and those of $ZrH_{1.93}$ (tetragonal), especially in the 2nd harmonics.

Fig. 6 shows the energy spectra of $TaH_{0.1}$ at room temperature (α-phase) and at 30 K (β-phase). At room temperature the fundamental peaks are fairly broad and the peak positions of the lower and the higher fundamentals are 114 meV and 163 meV, respectively. At low temperature these peaks become very sharp, and considerable shift in the peak position occurrs;

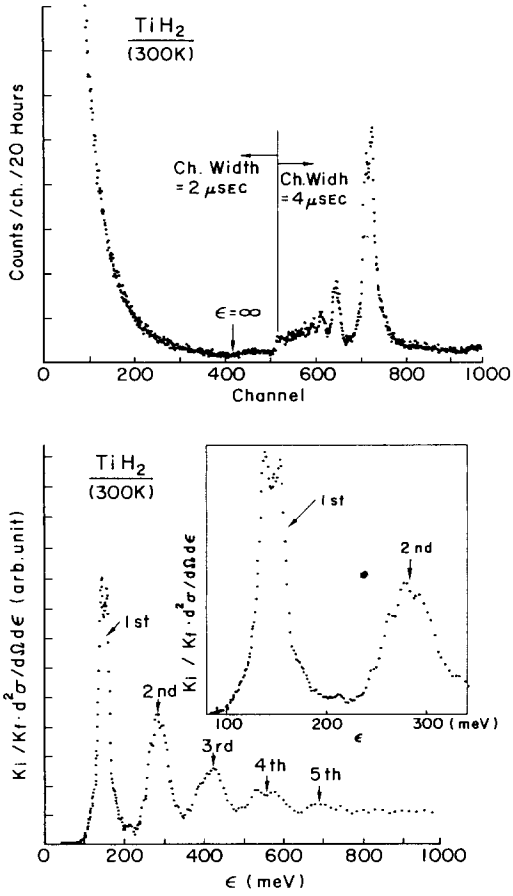

Fig. 4. TOF raw data (upper) and double differential cross section (lower) of TiH_2.

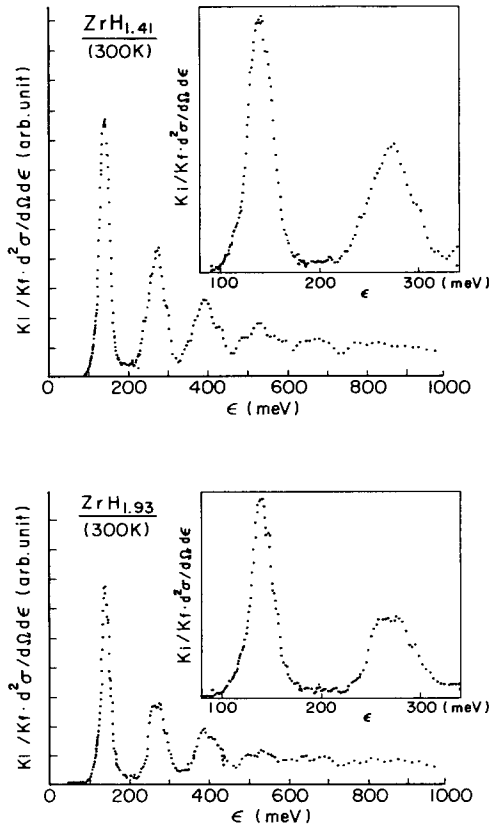

Fig. 5. Double differential cross section of $ZrH_{1.41}$ (upper) and $ZrH_{1.39}$ (lower).

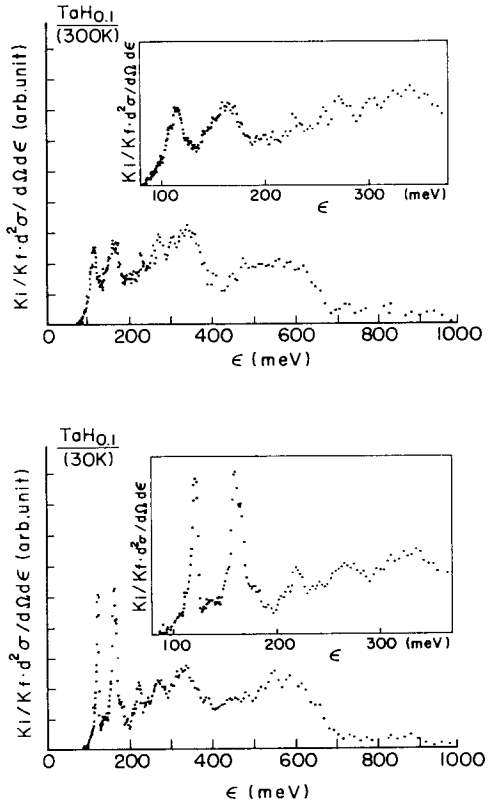

Fig. 6. Double differential cross section of $TaH_{0.1}$ at 30 K (upper) and at 300 K (lower).

the lower fundamental is found at 121 meV with the line width of 7 meV (FWHM). The energy resolution of the instrument is 2.7 meV at $\varepsilon \simeq$ 120 meV, then the intrinsic width of the peak is about 6.5 meV, the higher fundamental splits into two peaks at 159 and 165 meV. Hempelmann et al. [10] have measured $TaH_{0.08}$ at 77 K and fitted the unresolved higher fundamental peak by two gaussians. Present result supports their results with an experimental evidence. They also reported that second harmonics of the lower fundamental was detected at 227 meV.

We can observe a distinct peak of the second harmonics at about 220 meV in the energy spectra at low temperature. Small discrepancy in the peak position may be due to different temperature. Many peaks can be observed above this energy. Careful assignment of the peaks is under way. It may be noticed that no discrete level is observed beyond $\varepsilon \sim 700$ meV. The results suggest that the barrier height of the hydrogen potential is about 700 meV, which is consistent with the value of the proposed potential by Sugimoto and Fukai [13].

If we consider a small anharmonic disturbance of ${}^4a_4x$, nth vibration level ε_n relative to the ground state is given by

$$\varepsilon_n = \hbar\omega_0 n + \beta(n^2 + n) \qquad (n = 1, 2, 3, \ldots), \qquad (2)$$

where $\beta = 3\hbar^2 a_4/2m_H^2\omega_0^2$, m_H is the hydrogen mass and ω_0 the harmonic frequency.

In fig. 7 are plotted the measured values of ε_n (center of the nth peak) versus n for TiH_2. We have obtained anharmonicity parameter β of -2.4 meV with $\hbar\omega_0 = 147.6$ meV by fitting as shown in the figure. Corresponding values are also determined to be $\beta = -3.5$ meV with $\hbar\omega_0 =$ 147.3 meV for $ZrH_{1.41}$, and $\beta = -11$ meV with $\hbar\omega_0 = 143.3$ meV for $TaH_{0.1}$ at 30 K. Present value of β for $TaH_{0.1}$ (30 K) is larger than the reported value of 7.8 meV for $TaH_{0.08}$ (77 K) [10]. The discrepancy suggests a temperature dependence of the anharmonicity.

Note that the anharmonicity for $TaH_{0.1}$ at 30 K (bcc) is found to be somewhat larger than for TiH_2 (fcc) and $ZrH_{1.41}$ (fcc).

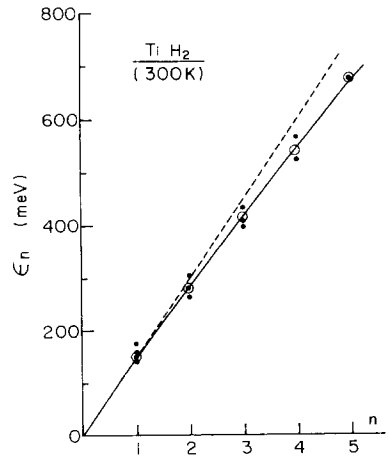

Fig. 7. Peak positions of TiH_2: (○) center of macro peak; (●) peak of fine structure; solid line: mean square fitting; broken line: harmonic energy level.

References

[1] S. Ikeda, N. Watanabe, K. Kai and S. Yamaguchi, KENS Report III, KEK Internal (1982) 104.
[2] N. Watanabe, M. Furusaka and M. Misawa, Res. Rep. Lab. Nucl. Sci., Tohoku Univ. 12 (1979) 72 (in Japanese).
[3] M. Furusaka, N. Watanabe and H. Asano, Res. Rep. Lab. Nucl. Sci., Tohoku Univ. 12 (1979) 83 (in Japanese).
[4] N. Watanabe and M. Furusaka, KENS Report I, KEK Internal 80-1 (1980) 181.
[5] D.H. Day and R.N. Sinclair, J. Chem. Phys. 55 (1971) 2870.
[6] K. Sköld, K. Crawford and H. Chen, Nucl. Instr. and Meth. 145 (1977) 117.
[7] J. Eckert, R.N. Silver, A. Soper, P.J. Vergamini, J. Goldstone, A. Larson, P.A. Seeger and J. Yarnell, Proc. ICANS-IV (1981) 434.
[8] S. Ikeda, N. Watanabe and K. Kai, KENS Report III, KEK Internal (1982) 109.
[9] J.G. Couch, O.K. Harling and L.C. Clune, Phys. Rev. B4 (1981) 159.
[10] R. Hempelmann and D. Richter, Z. Phys. B: Condensed Matter 44 (1981) 159.
[11] K. Kai, S. Ikeda, N. Watanabe and K. Suzuki, KENS Report III, KEK Internal (1982) 112.
[12] N. Watanabe, S. Ikeda and K. Kai, Proc. ICANS-VI.
[13] H. Sugimoto and Y. Fukai, J. Phys. Soc. Jap. 50 (1981) 3709.

Journal of the Physical Society of Japan
Vol. 56, No. 2, February, 1987, pp. 565-576

Local Modes and Hydrogen Potentials in Metal Hydrides

Susumu IKEDA and Noboru WATANABE

National Laboratory for High Energy Physics, Oho-machi, Tsukuba-gun, Ibaraki-ken 305

(Received October 9, 1986)

Hydrogen local modes in metal hydrides of $TaH_{0.1}$, $NbH_{0.31}$, $VH_{0.33}$ and TiH_2 have been measured up to about 1 eV using a high-resolution TOF-type neutron spectrometer coupled with a pulsed spallation neutron source. Measured spectra are discussed in terms of a simple anharmonic parameter. Hydrogen potentials $V(x, y, z)$ for $NbH_{0.31}$ and $VH_{0.33}$ are derived using experimental values.

§1. Introduction

Measurements of the local vibrational modes of hydrogen in metal hydrides by neutron scattering provide important information about the hydrogen potential in these system.[1-7] The local-mode spectrum esentially reflects the whole aspect of a hydrogen potential which strongly depends on the chemical and topological environment around a hydrogen atom; i.e. crystal symmetry, hole radius, lattice distortion and the kinds of host metals.

The aim of the present work was to study the hydrogen potential for typical metal hydrides by observing the local vibrational modes of hydrogen up to higher energies (about 1 eV). For this purpose we constructed a high-resolution time-of-flight (TOF) type crystal analyzer spectrometer coupled with a pulsed spallation neutron source which could provide narrow pulses of intense epithermal neutrons. The spectrometer can realize inelastic neutron scattering measurements over a wide range of energy transfers (0.05-1.0 eV) with a high energy-resolution (about 2 percent).[9] We performed minute measurements of local vibrational modes of hydrogen in powder samples of $NbH_{0.31}$, $VH_{0.33}$, $TaH_{0.1}$ and TiH_2 using this spectrometer.

Generally, the motion of hydrogen in metal hydrides has been considered to behave as decoupled oscillators with three degrees of freedom: x, y and z. Here, the simplest form of anharmonic hydrogen potential $V(X)$ in a given direction X can be expressed as

$$V(X)=A_2X^2+A_4X^4. \tag{1}$$

The n-th excitation energy ε_n can be approximated by

$$\varepsilon_n=n\hbar\omega+\beta(n^2+n), \tag{2}$$

with $\omega^2=2A_2/m$ and $\beta=3\hbar^2A_4/4m^2\omega^2$. The term of A_4X^4 shifts the n-th excitation energy relative to the harmonic energy $n\hbar\omega$ by the amount $\beta(n^2+n)$. For a latter discussion we classify the hydrogen potential defined by eq. (1) into three types, depending upon the anharmonic parameter β (Fig. 1); these are

(a) $\beta=0$: Harmonic potential (Fig. 1(a)),

(b) $\beta<0$: Trumpet like potential (Fig. 1(b)) and

(c) $\beta>0$: Well like potential (Fig. 1(c)).

The energy spectrum of hydrogen local modes also exhibits a characteristic feature corresponding to the type of potential (Fig. 1). Thus, the type of potential can be immediately determined from the measured energy spectrum. We determine the anharmonic parameter β from the measured energy spectrum of the local modes and classify the hydrogen potential into three types. A more exact approach would be to describe the hydrogen motion as a three-dimentional anharmonic oscillator where the x-, y- and z-motions of the hydrogen are no longer decoupled. In terms of this realistic model we discuss the hydrogen potentials in $NbH_{0.31}$ and $VH_{0.33}$ using the measured excitation energies of the local-mode peaks.

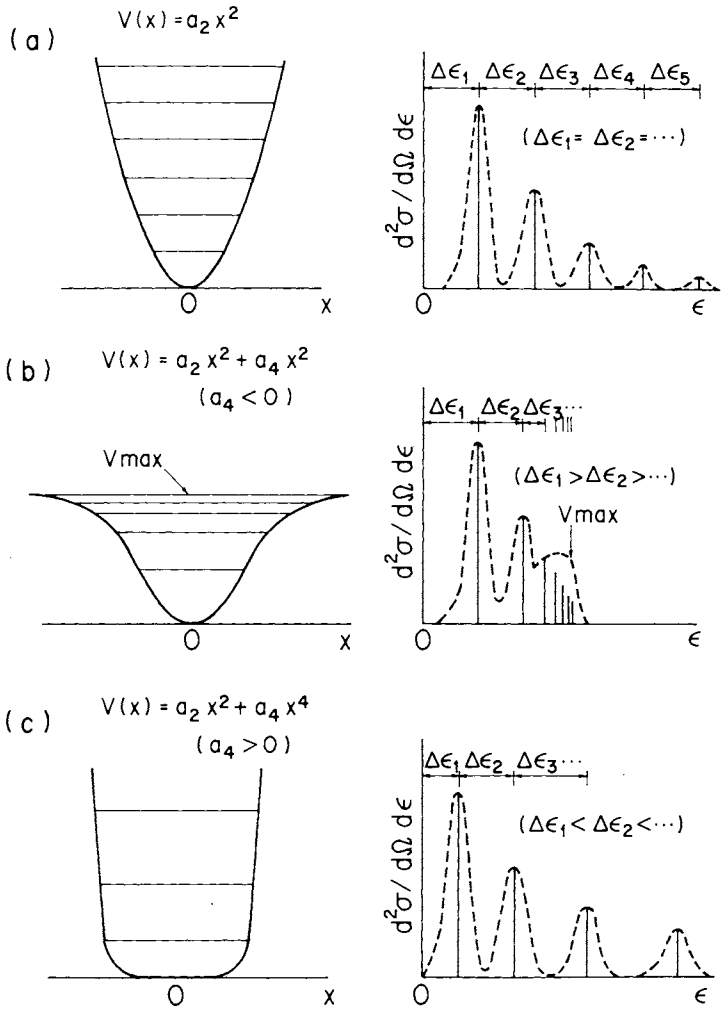

Fig. 1. Three types of hydrogen potential: (a) Harmonic potential, (b) trumpet like potential and (c) well like potential.

An assignment of the local-mode peaks with quantum numbers is very important for determining the hydrogen potential. This could be more reliably achieved by using a single-crystal sample in which hydrogen is oriented to a symmetrical axis of the host lattice. With a single-crystal sample one can selectively observe the local modes parallel to the scattering vector. We also tried a feasibility experiment with the single-crystal $NbH_{0.31}$ using this spectrometer.

§2. Instrument

Figure 2 shows the configuration of the high-resolution TOF type crystal analyzer spectrometer, CAT, which is installed at the pulsed spallation neutron source, KENS, at the National Laboratory for High Energy Physics, KEK (Japan). The spectrometer is an inverted-geometry type, in which white neutrons are incident upon the sample. Scattered neutrons of fixed energy E_f are selected by an analyzer crystal, while the incident neutron energy is determined by the time-of-flight. In this spectrometer the energy transfer ε is given by

$$\varepsilon(\mathrm{meV}) = 5.182 \cdot 10^6 L_i / (t(\mu\mathrm{s}) - 821)^2 - 3.9, \quad (3)$$

where L_i is an incident flight-path length of 5.299 m and t the total time of flight.[9] In order to realize a higher counting rate, as well as a higher energy resolution, a time-focussing

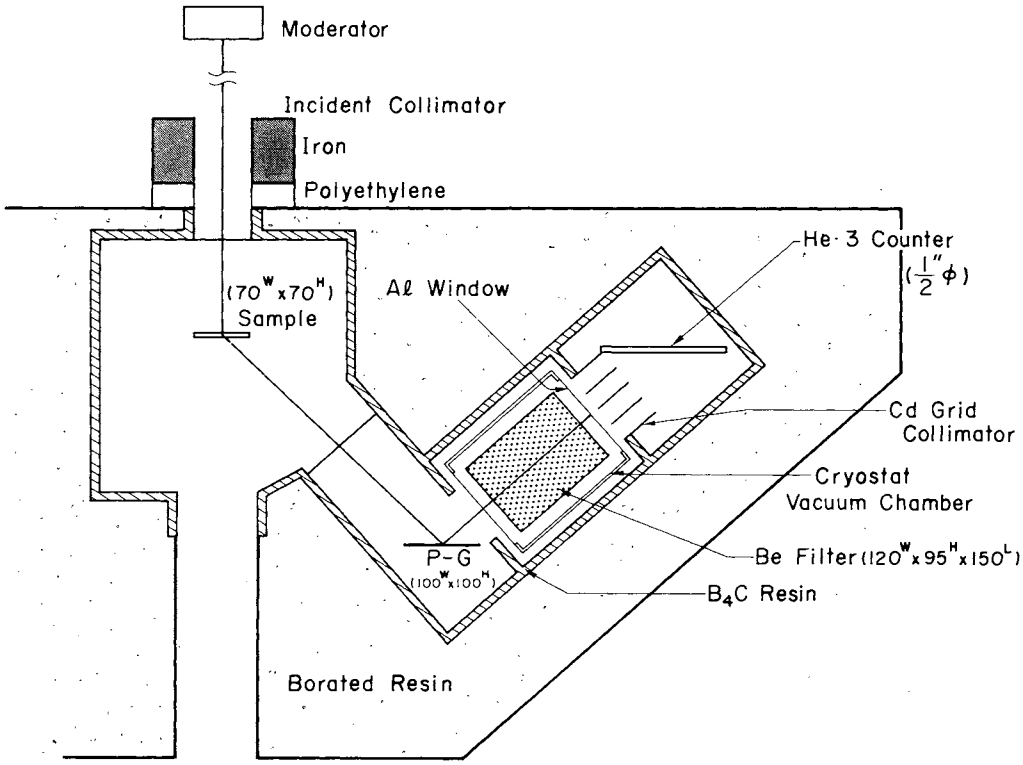

Fig. 2. Configuration of the CAT spectrometer.

principle was adopted in the sample-analyzer-detector system.[9] The spectrometer made it possible to measure incoherent neutron scattering with a large energy transfer in the range $\varepsilon=0.05$–1.0 eV, with a resolution $\Delta\varepsilon/\varepsilon\approx0.02$ over the entire energy-transfer range.

§3. Experiment

Powder samples of metal hydride were prepared as follows: Nb, Ta and V metals were melted by an electron beam and then rolled to 0.2-mm thick foils. The foils were outgassed under a high vacuum in quartz tubes at a high temperature and then exposed to purified hydrogen gas. Fine-powder samples of $NbH_{0.31}$, $TaH_{0.1}$ and $VH_{0.33}$ were obtained by crashing the hydride foils. A fine-powder sample of TiH_2 was commertially avairable with high quality. Since the CAT spectrometer is optimized for a planner sample, a powder sample was contained in a flat aluminum cell 8.5-cm wide × 9-cm high × 0.1–0.5-cm thick. The maximum beam size at the sample position was 7-cm wide × 7-cm high. As a single crystal, a hydrogen doped single-crystal Nb ($NbH_{0.33}$) was prepared. Ten rods of single-crystal Nb of 0.6 cm in diam. and 5 cm in length were grown with the crystal axis ⟨110⟩ parallel to the rod axis. They were also outgassed under a high vacuum in a qualtz tube and then exposed to purified hydrogen gas at a high temperature. The hydride rods of single-crystal Nb were alined in a plane to form a planner sample with the same orientation. The counting time for each sample was about 2 days.

Figure 3 shows an energy spectrum of the local modes in TiH_2 at 300 K; it was obtained from a measured TOF spectrum.[9] We can observe local modes up to the 5-th excitation at about 700 meV. The peak positions are plotted against the quantum number n in the inset of the figure; this shows that the energies for the higher harmonics are shifted by small amounts from their respective harmonic positions. We determined the anharmonic

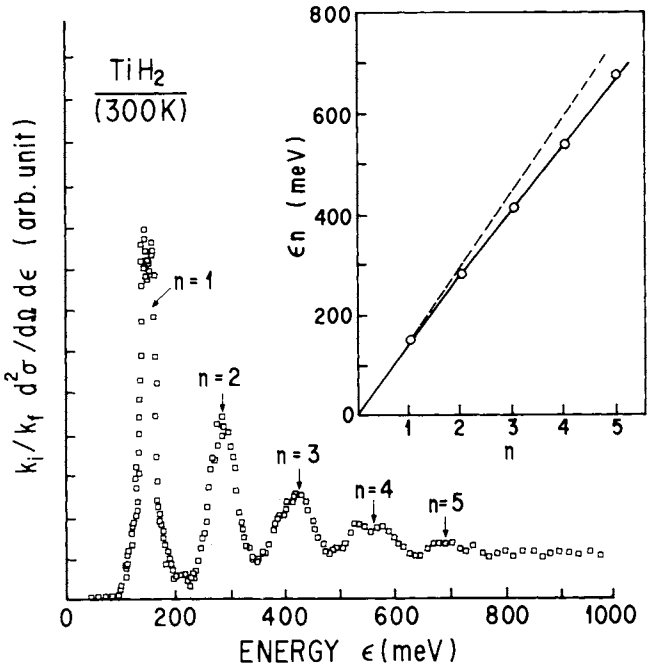

Fig. 3. Energy spectrum of local modes in TiH_2 at room temperature.

parameter β using eq. (2) and obtained $\beta = -2.4$ meV with $\hbar\omega = 147.6$ meV for TiH_2 (300 K). The energy spectra of $ZrH_{1.43}$ and $ZrH_{1.91}$ were also measured up to the 5-th excitation and results similar to TiH_2 were obtained in both measurements.[5] The results indicate that the hydrogen potential for a tetrahedral site (T-site) in an fcc structure is close to type (c), i.e. almost harmonic.

Figure 4 shows the energy spectrum of $TaH_{0.1}$ at 30 K. Hydrogen atoms of $TaH_{0.1}$ (30 K) exist at the T-side of a bcc structure.[8] The peak at 121.1 meV corresponds to the first excitation of z-motion and the peak at about 160 meV to that of x- and y-motions refrecting the symmetry of the T-site. The definitions for the x-, y- and z-directions are the same as that for the T-site of $NbH_{0.31}$ shown in Fig. 8(a). The higher first excitation peak splits into two peaks at 159 and 165 meV due to an orthorhombic distortion in β-$TaH_{0.1}$ (see the enlarged spectrum in the figure). This is the first observation for a splitting of the higher first excitation peak. Hempelmann *et al.*[6] calculated the energy ratio of the splitting to be $\varepsilon_3/\varepsilon_2 = 1.044$, using the results of X-ray and electron diffraction. Our experimental value of 1.041 is consistent with their calculated value. The result demonstrates that the local modes of hydrogen vibrations are very sensitive to the environment. A distinct peak corresponding to the second excitation of the z-motion was observed at about 220 meV. Many broad peaks at higher energies were also observed up to 700 meV; however, the spectrum rappidly decreased beyond 700 meV. The anharmonic parameter β for $TaH_{0.1}$ (30 K) was also calculated using the measured peak energies of 121.1 and 220 meV; $\beta = -11$ meV was obtained with $\hbar\omega = 143$ meV. The absolute value of the anharmonic parameter is much larger than that of TiH_2 and the sign of β is negative. This indicates that the hydrogen potential of $TaH_{0.1}$ is type (b), i.e. trumpet like. These experimental results (the potential is a trumpet type and the intensity of the energy spectrum goes down to almost zero at about 700 meV) suggest, perhaps, that the barrier height of the hydrogen potential for β-$TaH_{0.1}$ is about 700 meV. This value is consistent with the potential proposed by Sugimoto and Fukai.[10]

Figure 5 shows the energy spectrum of $VH_{0.33}$ at 30 K. Hydrogen atoms in $VH_{0.33}$ (30 K)

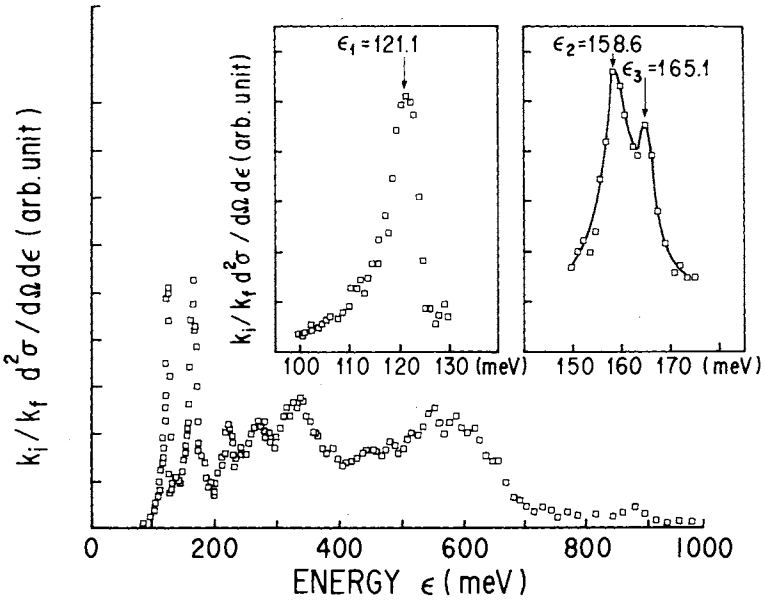

Fig. 4. Energy spectrum of local modes in $TaH_{0.1}$ at 30 K.

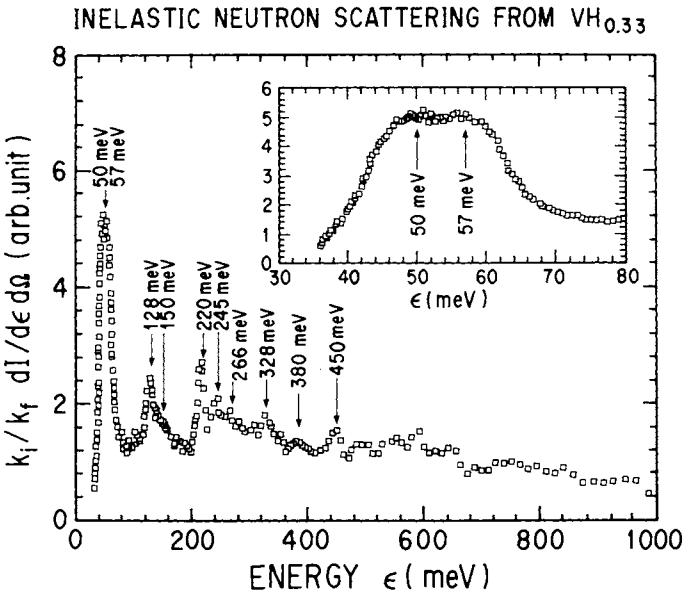

Fig. 5. Energy spectrum of local modes in $VH_{0.33}$ at 30 K.

exist at the octahedral site (O-site) of a bcc structure, as shown in Fig. 8(b).[8] The peaks at about 53.5 and 220 meV correspond to the first excitation of the x- and y-motions and that of the z-motion, reflecting the symmetry of the O-site, respectively.[11] The x, y and z directions are also defined in Fig. 8(b). Some higher excitation peaks were also observed at 128, 150, 245, 266, 328, 380 and 450 meV (Table I). The lower first excitation peak at about 53.5 meV was observed for the first time upon splitting into two peaks at 50 and 57 meV (see the enlarged spectrum in the figure). The splitting may be caused by a small monoclinic distortion in β-$VH_{0.33}$. Since the broad peak at about 128 meV is considered to

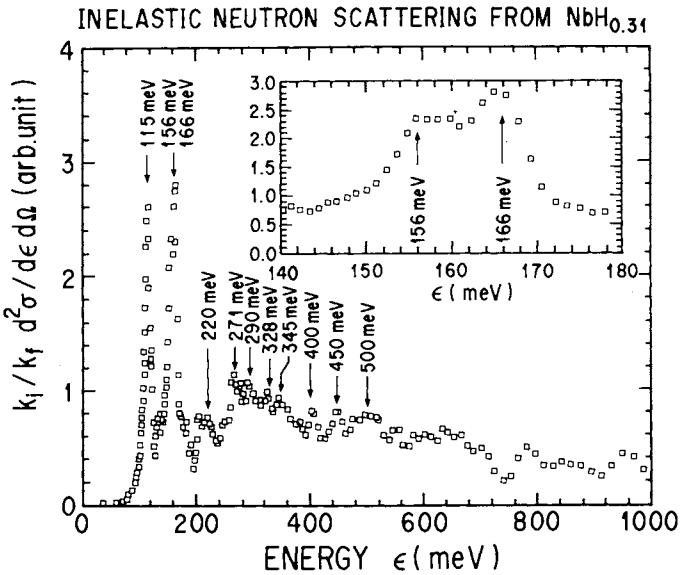

Fig. 6. Energy spectrum of local modes in $NbH_{0.31}$ at 30 K.

be a second order-excitation peak of x- and y-motions,[11] the anharmonic parameter β was determined to be $+11$ meV, using the measured values of $(50+57)/2$ and 128 meV. Note that the absolute value of the anharmonic parameter is very large and that the sign is positive in contrast with that of $TaH_{0.1}$. Thus, the shape of the hydrogen potential for β-$VH_{0.33}$ is type (c), i.e. well like.

Figure 6 shows the energy spectrum from a powder sample of $NbH_{0.31}$ at 30 K. The spectrum is very similar to that of $TaH_{0.1}$ (30 K) since the hydrogen in $NbH_{0.31}$ also exists at the T-sites of a bcc structure.[8] The peak at 115 meV corresponds to the first excitation of the z-motion and the peak at about 160 meV to that of the x- and y-motions. The directions of x, y and z are shown in Fig. 8(a). The higher first excitation was observed for the first time as two distinct peaks at 156 and 166 meV due to the orthorhombic distortion (see the enlarged spectrum in the figure). A distinct peak corresponding to the second excitation of the z-motion was observed at 220 meV and, moreover, some higher excitation peaks were observed at 271, 290, 328, 345, 400, 450 and 500 meV (Table II). The anharmonic parameter β was determined to be -5 meV using peak energies of 115 and 220 meV. The absolute value of β was larger than that of TiH_2 but smaller than that of $TaH_{0.1}$. The result indicates that the shape of the hydrogen potential for an ordered phase $NbH_{0.31}$ is trumpet-type with an anharmonicity less than that of $TaH_{0.1}$.

In measurements on the powder samples all local modes due to the x-, y- and z-motions can be simultaniously observed in the energy spectrum. The assignments of the local mode peaks, especially higher-order ones, are therefore not so easy; they are sometimes accompanied by ambiguities. In order to overcome this weak point, we proposed the following method and then examined the feasibility. If the x-, y- and z-motions of the hydrogen are considered to be decoupled oscillators with three degrees of freedom, the double differential neutron cross section for the excitations of ω_x, ω_y and ω_z can be given by

$$d^2\sigma/d\varepsilon\, d\Omega \approx \{Q_x\delta(\varepsilon-\hbar\omega_x)+Q_y\delta(\varepsilon-\hbar\omega_y)+Q_z\delta(\varepsilon-\hbar\omega_z)\}\, k_i/k_f, \quad (4)$$

where $\boldsymbol{k}_f$ and $\boldsymbol{k}_i$ are the final and the initial neutron wave vectors, respectively, and $\boldsymbol{Q}=\boldsymbol{k}_i-\boldsymbol{k}_f$ is the momentum transfer. Here, the Debye Waller factor and the population factor are neglected for simplicity. Since the final energy ($E_f=3.9$ meV) is much smaller than the initial energy ($E_i>50$ meV), the

amplitude of $\boldsymbol{Q}$ is almost equal to k_i and the direction of $\boldsymbol{Q}$ is approximately parallel to $\boldsymbol{k}_i$ (through the high-energy transfer measurements by the CAT). If the sample is a perfectly oriented single crystal of the metal hydride (hydrogen atoms are oriented along the symmetrical axis of the host metal) and the direction of $\boldsymbol{k}_i$ is set parallel to the z-direction of the hydrogen potential, the local modes due to the z-motion only can be observed in the spectrum without any contamination due to the x- and y-motions. This experiment is useful for a more reliable assignment of the higher-order peaks as well as the fundamental peaks. The feasibility experiment was performed using the hydrogen doped single-crystal Nb since it is expected to have, more or less, a prefered orientation of the hydrogen.

Figure 7 shows two raw TOF spectra obtained from the hydrogen-doped single-crystal Nb($NbH_{0.33}$ at 300 K) with two different sample settings. Closed and open circles indicate the measured spectra for $\langle 110\rangle \| \boldsymbol{k}_i$ and $\langle 001\rangle \| \boldsymbol{k}_i$, respectively. In these spectra two distinct peaks at about 880 and 965 channels correspond to the first excitations at 160 and 115 meV, resprectively, as observed in the powder sample. We observed an appreciable change of the energy spectrum between the two settings. In the case of $\langle 001\rangle \| \boldsymbol{k}_i$ the peak intensity at 115 meV due to z-motion grows, while the peak intensity at 160 meV due to x- and y-motions goes down. On the other hand the intensity change is reversed in the case of $\langle 110\rangle \| \boldsymbol{k}_i$. The intensity modulation was about 10 percent at each peak position. This means that the hydrogen in this sample was partially orientated (by about 10 percent). An intensity modulation of 10 percent can also be expected for the higher excitation peaks (beyond 200 meV). However, it was not possible to observe an appreciable intensity modulation of the higher-order peaks because of poor statistics. In the present experiment we confirmed, at least, the feasibility of this method by the intensity modulation of the fundamental local modes. A further measurement with better statistics is under progress in order to certify the assignment of the higher-order peaks.

§4. Discussion

We measured the local modes of typical metal hydrides and classified the hydrogen potential into three types. However eq. (1) is too simple to express an actual hydrogen potential. It should be described by a more realistic function involving the deviation x, y and z with their cross terms. J. Eckert *et al.* introduced a novel Hamiltonian for the hydrogen motions in the T-site and discussed

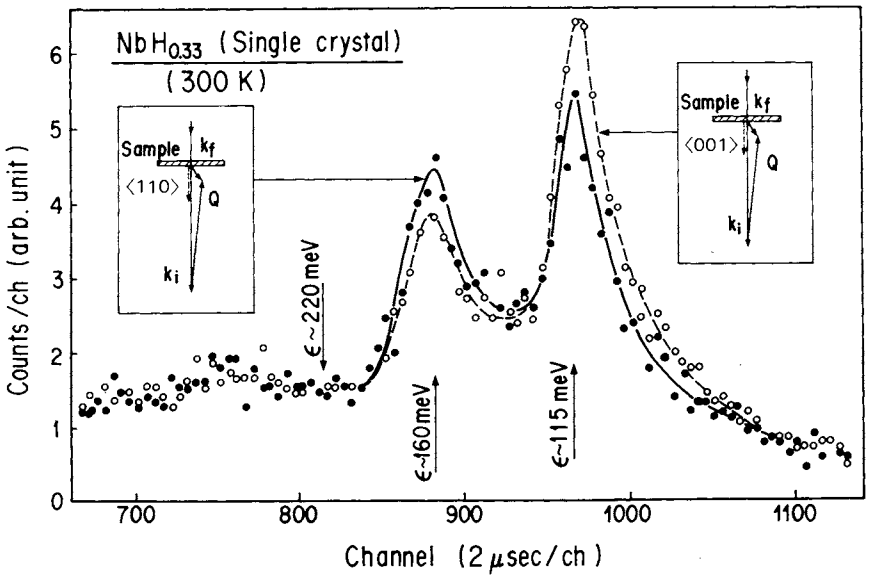

Fig. 7. TOF spectra of local modes in single crystal $NbH_{0.33}$ at room temperature.

the anharmonic parameters.[7] Here, we added a $C_{6z}z^6$ term to their formulation in order to make a good representation of the z-dependence of the hydrogen poential; we tried to derive the hydrogen potential using the measured excitation energies, including the higher orders. The Hamiltonian H can be described as

$$H=H_0+H_1,$$
$$H_0=P^2/2m+m\omega_x^2X^2/2+m\omega_y^2Y^2/2+m\omega_z^2Z^2/2,$$

and

$$H_1=eZ(X^2-Y^2)+fX^2Y^2+g(X^2+Y^2)Z^2+C_{4x}(X^4+Y^4)+C_{4z}Z^4+C_{6z}Z^6, \quad (5)$$

where ω_x, ω_y and ω_z are the harmonic frequencies and $\omega_x=\omega_y$ is satisfied for the T-site. It is straight forward to calculate the excitation energy $\varepsilon(lmn)=E(lmn)-E(000)$, where $E(lmn)$ is the perturbed energy of the vibrational state corresponding to the (lmn) harmonic level. The l, m and n are the quantum numbers for vibrational excitations in x-, y- and z-motions, respectively. In our measurement on the powder sample of $NbH_{0.31}$ we observed slightly different excitation energies concerning $\varepsilon(100)$ and $\varepsilon(010)$; these arise from an orthorhombic distortion of $NbH_{0.31}$(30 K). However, for simplicity, we neglected the effect of the distortion and used the value $(\varepsilon(100)+\varepsilon(010))/2$ as the fundamental excitation energy of the x- and y-motions, since the splitting is small. Figure 8 shows the T-sites (T_1, T_2, T_3 and T_4) on the (010) plane in $NbH_{0.31}$. We assumed the following three conditions regarding hydrogen potential $V(x, y, z)$ and the occupation: (1) Hydrogen occupies only a T_1-site, (2) $V(x, 0, 3.3/4)$ has a minimum at the T_2- and T_3-sites and (3) $V(0, 0, z)$ has a minimum at the T_1-site and a maximum at the O_1- and O_2-sites. The parameters in the hydrogen potential of $NbH_{0.31}$ were calculated using six experimental values of the excitation energies listed in Table II (with asterisks). These were assigned by the quantum numbers l, m and n in the last column. The calculated parameters of the hydrogen potential in $NbH_{0.31}$ at 30 K are listed in Table III. Measured excitation energies with no asterisks should be compared with the excitation energies $(l+m+n\leq 3)$ calculated using the derived potential. The calculated values are listed in the second column of Table II. The agreements with the experimental values are fairly good. It is remarkable that the values of $\hbar\omega_x$ and $\hbar\omega_z$ are close to each other and are almost the same as those of TiH_2 and $ZrH_{1.43}$,[5] in which the hydrogen exists at the T-site of an fcc structure (see Table III). Figure 9 shows four contour maps of the derived hydrogen potential on the planes of $y=0$, 0.2, 0.4, 0.6 A. In the contour map of $y=0$, we can see the smallest minimum point at the T_1-site, two minimum

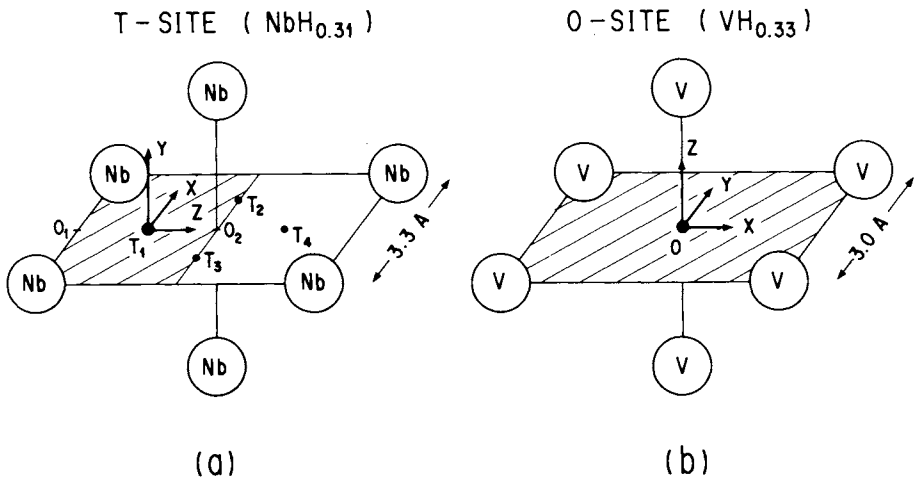

Fig. 8. T-site(a) and O-site(b) in bcc structure.

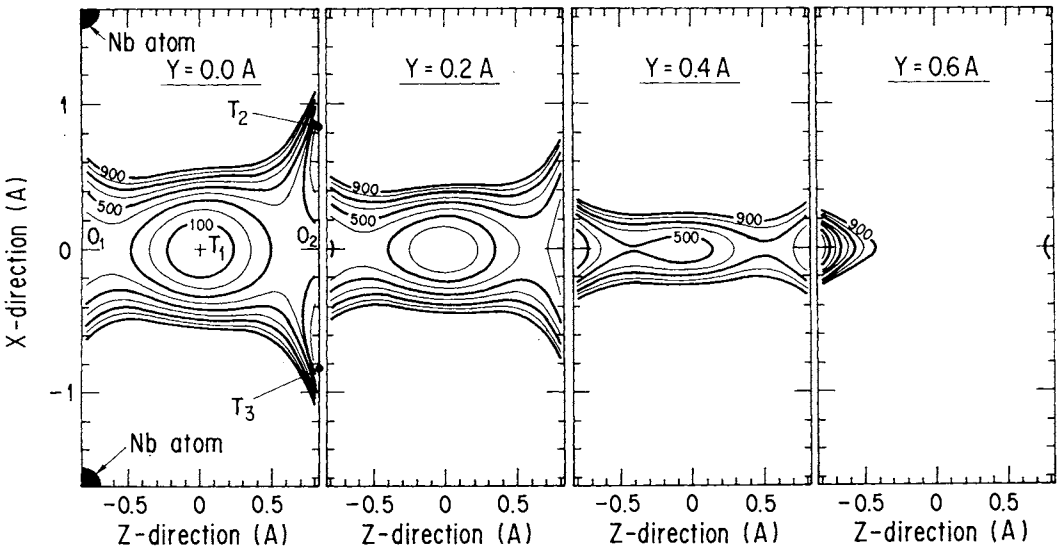

Fig. 9. Contour maps of the hydrogen potential in $NbH_{0.31}$. Contour lines are 100, 200, 300, 400, 500, 600, 700, 800 and 900 meV.

points at T_2 and T_3 as apparent from the initial conditions, and two saddle points of about 400 meV around T_1. The smallest minimum point moves from the T_1-site to the left (-z-direction) with increasing y and settles on the plane for $z=-0.825$ A when y becomes about 0.4 A.

The wave functions ψ_{lmn} were expressed by linear combinations of the harmonic wave function Ψ_{lmn}; their coefficients were determined in the analysis as

$$\psi_{000} \approx \Psi_{000} - 0.007(\Psi_{021} - \Psi_{201}),$$
$$\psi_{001} \approx \Psi_{001} - 0.02(\Psi_{200} - \Psi_{020}) - 0.01(\Psi_{022} - \Psi_{202}),$$

and

$$\psi_{100} \approx \Psi_{100} + 0.03\Psi_{301} - 0.007\Psi_{121}, \qquad (6)$$

where ψ_{000}, ψ_{001} and ψ_{100} are wave functions of the ground state, the lower first excited state and the higher first excited state, respectively. The wave functions are shown in Fig. 10. ψ_{000} is almost the same as the harmonic wave function Ψ_{000} and is approximately isotropic since $\omega_x(=\omega_y) \approx \omega_z$. ψ_{001} is polarized only to the z-direction, while ψ_{100} is almost polarized along the x-direction with a small polarization of z-direction (eq. (6)).

In the case of $VH_{0.33}$, we can put $\omega_x = \omega_y$ and $e=0$ in eq. 5 from the symmetry of the O-site. We obtained the parameters of the hydrogen potential of $VH_{0.33}$ (Table III) using six experimental values of the excitation energies listed in Table I (with asterisks); these were assumed to be assigned by the quantum numbers l, m and n as listed in the last column. Measured excitation energies with no asterisks should also be compared with the excitation energies ($l+m+n \leq 3$, $n<3$) calculated using the derived potential. The calculated values are listed in the second column of Table I. The agreements with the experimental values are also good. Note that the value of $\hbar\omega_z$ is much different from that of $\hbar\omega_x$, contrary to the case of $NbH_{0.31}$. Figure 11 shows contour maps of the derived hydrogen potential on the planes $y=0$ (Fig. 11(a)) and $z=0$, 0.2, 0.27, 0.29 A (Fig. 11(b)). In Fig. 12 are depicted the calculated wave function of the ground state in $VH_{0.33}$ on the planes of $z=0$ ($x-y$ plane) and $x=0$ ($y-z$ plane). The hydrogen potential and the ground-state wave function are highly anisotropic. The potential has a narrow bottom with a steep gradient in the z-direction, but a flat bottom with a modest slope in the $x-y$ plane (note that the scale of z-axis in Fig. 11(a) is enlarged by three times than that of x-axis). Correspondingly, the ground-state wave function is strongly lo-

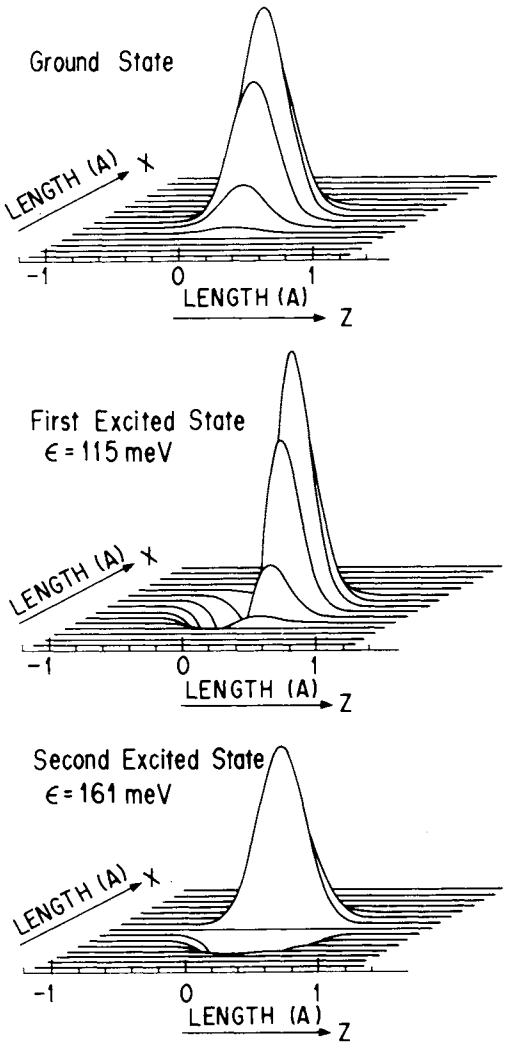

Fig. 10. Wave functions of hydrogen for ground state and excited states in $NbH_{0.31}$.

calized in the z-direction but spreads out widely in the $x-y$ plane. The characteristic feature of the potential shape in the present work is qualitatively consistent with the deuterium density distribution in $VD_{0.51}$ determined by a neutron diffraction.[12,13] The density distribution is localized in z-direction but expands in x- and y-directions with skirts covering the four neighbouring T-sites.[12,13] Contour lines above near 300 meV exhibit small depressions around $x=0$ (Fig. 11(a)). The minimum point of the potential moves sensitively from O-site onto T-site with increasing z and settles on T-site when z becomes about 0.27 A. These results may correspond to the interpretation

Table I. Measured and calculated values of local modes of $VH_{0.33}$ (30 K).

Experimental value (meV)	Calculated value (meV)	Quantum numbers (lmn)
53.5*	53.5	(100)(010)
128*	128	(200)(020)
150*	150	(110)
220*	220	(001)
245	224	(210)(120)
245	223	(300)(030)
266*	266	(101)(011)
380	355	(111)
450*	450	(002)

Table II. Measured and calculated values of local modes of $NbH_{0.31}$ (30 K).

Experimental value (meV)	Calculated value (meV)	Quantum numbers (lmn)
115*	115	(001)
160*	160	(100)(010)
220*	220	(002)
271*	271	(101)(011)
290	316	(003)
323*	323	(200)(020)
345*	345	(110)
400	372	(102)(012)
450	452	(111)
500	489	(300)(030)
500	508	(210)(120)

Table III. Hydrogen potential parameters.

	$NbH_{0.31}$	$VH_{0.33}$	TiH_2	$ZrH_{1.43}$
$\hbar\omega_x$ (eV)	0.147	0.0152	0.148	0.147
$\hbar\omega_z$ (eV)	0.130	0.218	0.148	0.147
e (eV/A^4)	1.246			
f (eV/A^4)	30.77	0.565		
g (eV/A^4)	−4.23	−1.438		
C_{4x} (eV/A^4)	1.373	0.092		
C_{4z} (eV/A^4)	−3.807	9.032		
C_{6z} (eV/A^6)	2.272			

that hydrogen atoms in bcc metals tend to prefer O-sites to T-sites as the lattice parameter is reduced and, in particular, vanadium is the borderline in this respect.[10]

In this paper we reported the energy spectra of the hydrogen local modes in typical metal hydrides TiH_2, $TaH_{0.1}$, $NbH_{0.31}$ and $VH_{0.33}$ up to higher excitations. We demonstrated that the local mode is very sensitive to the environment with a distinct splitting of the local

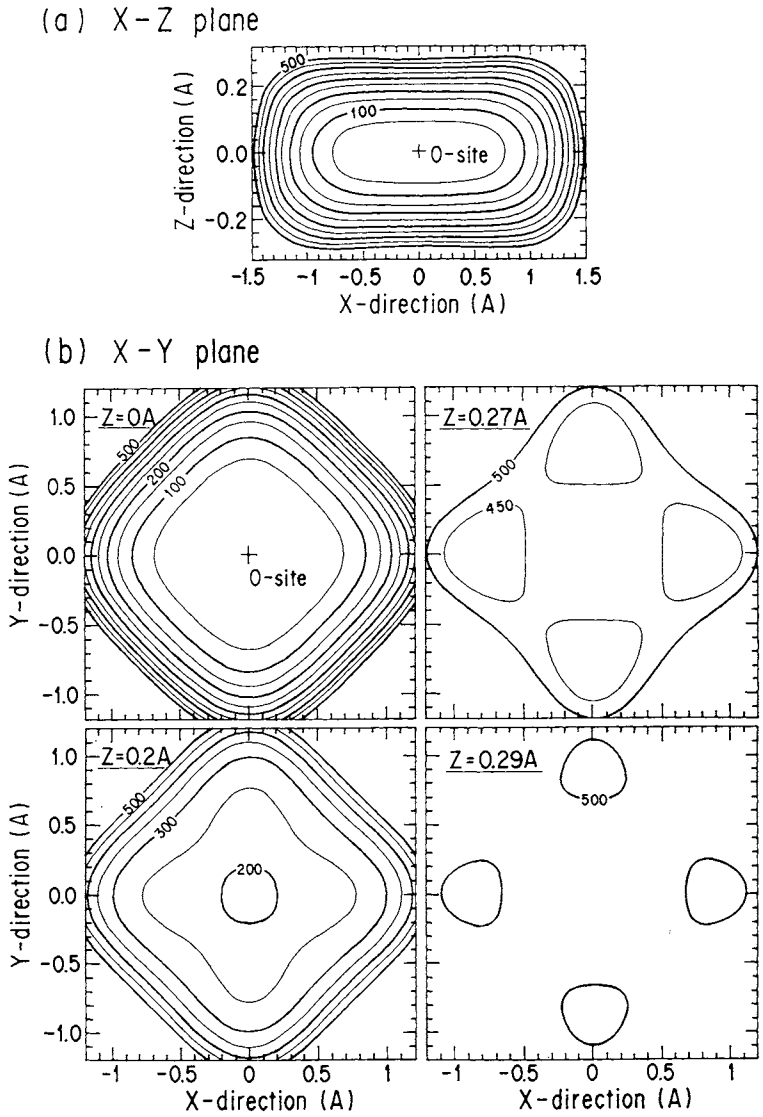

Fig. 11. Contour maps of the hydrogen potential in $VH_{0.33}$. Contour lines are 50, 100, 150, 200, 250, 300, 350, 400, 450 and 500 meV. Positions of vanadium atoms are (−1.5, −1.5, 0), (−1.5, 1.5, 0), (1.5, −1.5, 0), (1.5, 1.5, 0), (0, 0, −1.5) and (0, 0, 1.5).

modes due to a distortion of the host lattice. We determined the anharmonic parameters β and discussed the hydrogen potentials with β. We further discussed the hydrogen potentials of $NbH_{0.31}$ and $VH_{0.33}$ using a three-dimentional model. However, the assignments of local modes are not well-grounded, especially for the higher excitation peaks. It should be determined whether those are correct or not. The best method for doing this would be to use a single crystal of metal hydride in large energy-transfer measurements and to separate the peaks due to the z-motion in the energy spectrum from those due to x- and y-motions (as demonstrated in previous section). We will undertake the further experiments using better single crystals in order to exactly assign the excitation peaks and the confirm our proposed hydrogen potentials.

Acknowledgements

The authors gratefully acknowledge the

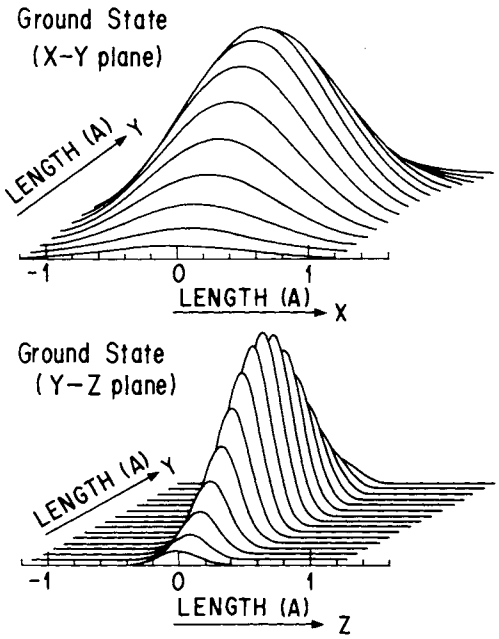

Fig. 12. Wave function of hydrogen for the ground-state in $VH_{0.33}$.

kind cooparation of Professor H. Asano and Dr. K. Kai for sample preparation and discussions.

References

1) K. Kai, S. Ikeda, T. Fukunaga, N. Watanabe and K. Suzuki: Physica **120B** (1983) 342.
2) D. Richter: *Proc. 1984 Workshop on High Energy Excitation in Condensed Matter* (Los Alamos, Feb. 13–15, 1984), LA-10227 (1984) 559.
3) D. Richter and S. M. Shapiro: Phys. Rev. B**22** (1980) 599.
4) D. Richter, J. J. Rush and J. M. Rowe: Phys. Rev. B**27** (1983) 6227.
5) S. Ikeda, N. Watanabe and K. Kai: Physica **120B** (1983) 131.
6) R. Hempelmann, D. Richiter and A. Kollmar: Z. Phys. B**44** (1981) 159.
7) J. Eckert, J. A. Goldstone, D. Tonks and D. Richter: Phys. Rev. B**27** (1983) 1980.
8) T. Schober and H. Wenzl: *Hydrogen in Metals II*, ed. G. Alfled and J. Volkl (Springer-Verlag, Berlin, 1978) p. 11.
9) S. Ikeda and N. Watanabe: Nucl. Inst. Meth. **221** (1984) 571.
10) H. Sugimoto and Y. Fukai: J. Phys. Soc. Jpn. **50** (1981) 3709.
11) D. Klauder, V. Lottner and H. Scheuer: Solid State Commun. **32** (1979) 617.
12) I. Okada, H. Asano and M. Hirabayashi: *Proc. 2nd JIM Int. Symp. on Hydrogen in Metals*, Suppl. Trans. JIM **21** (1980) 89.
13) M. Hirabayashi and H. Asano: *Metal Hydrides*, ed. G. Bambakids (Plenum Press, N.Y., 1981) p. 53.

IOPscience iopscience.iop.org

Home Search Collections Journals About Contact us My IOPscience

Hydrogen wave functions in the metal hydrides ZrH_2 and $NbH_{0.3}$

This article has been downloaded from IOPscience. Please scroll down to see the full text article.

1990 J. Phys.: Condens. Matter 2 4675

(http://iopscience.iop.org/0953-8984/2/21/002)

View the table of contents for this issue, or go to the journal homepage for more

Download details:
IP Address: 128.219.49.9
The article was downloaded on 09/11/2010 at 18:29

Please note that terms and conditions apply.

J. Phys.: Condens. Matter 2 (1990) 4675–4684. Printed in the UK

Hydrogen wave functions in the metal hydrides ZrH_2 and $NbH_{0.3}$

Susumu Ikeda†, Michihiro Furusaka†, Toshiharu Fukunaga‡ and A D Taylor§

† National Laboratory for High Energy Physics, Oho, Tsukuba-shi, Ibaraki-ken 305, Japan

‡ Department of Crystalline Materials Science, Nagoya University, Furo-cho, Chikusa-ku, Nagoya 464, Japan

§ Rutherford Appleton Laboratory, Oxfordshire, UK

Received 4 December 1989

Abstract. The hydrogen local vibrational modes of ZrH_2 and $NbH_{0.3}$ were observed by using a chopper neutron spectrometer coupled with a pulsed spallation neutron source. From the momentum transfer dependence of their modes, it was confirmed that the hydrogen wave functions for the first, second and third excited states in ZrH_2 are completely harmonic, and found that those for $\varepsilon = 220$ meV and $\varepsilon = 161$ meV in $NbH_{0.3}$ are very different from simple harmonic, although that for the first excited state ($\varepsilon = 115$ meV) seems to be harmonic.

1. Introduction

Measurements of the hydrogen vibrational local modes in metal hydrides [1–8] have provided important information about the hydrogen potential which strongly depends on the chemical and topological environments around a hydrogen atom. In the early investigations [5, 6], the hydrogen potential was discussed simply in terms of an anharmonic parameter, β. If the shape of the hydrogen potential, $V(X)$, in a given direction X is expressed as $V(X) = A_2X^2 + A_4X^4$, the nth excitation energy, ε_n, can be approximated as $\varepsilon_n = n\hbar\omega + \beta(n^2 + n)$, with $\omega^2 = 2A_2/m$ and $\beta = 3\hbar^2A_4/4m^2\omega^2$. The term A_4X^4 shifts the nth excitation energy relative to the harmonic energy, $n\hbar\omega$, by the amount $\beta(n^2 + n)$. Therefore, the hydrogen potential can be classified according to the value of β into three types: harmonic ($\beta = 0$), trumpet-like ($\beta < 0$) and well-like ($\beta > 0$). In fact, detailed measurements of the local vibrational modes had been performed, and their anharmonic parameters determined, for example, the β-values of TiH_2 and ZrH_2 were almost zero (harmonic); the β-values of $NbH_{0.31}$ and $TaH_{0.1}$ were determined to be -5 meV and -11 meV, respectively (trumpet-like); the β-value of $VH_{0.33}$ was determined to be $+11$ meV (well-like) [8]. Recently, a more exact approach for metal hydrides NbH and TaH has been taken, assuming that the hydrogen motion is like a three-dimensional (3D) anharmonic oscillator, where the x, y and z motions of the hydrogen are no longer decoupled [7]. A similar approach with some modifications has been applied to $NbH_{0.31}$ and $VH_{0.33}$, in order to extract the parameters of their hydrogen potentials using the measured excitation energies of the local modes [8]. From this

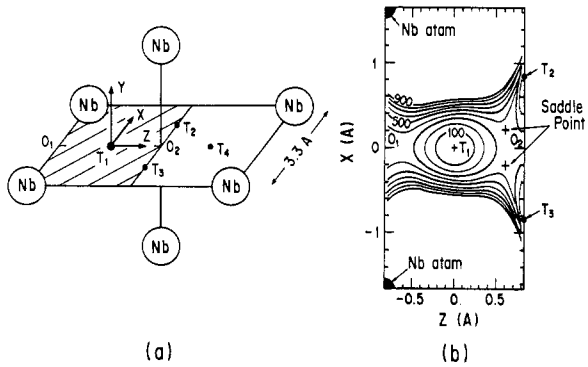

Figure 1. T and O sites in $NbH_{0.3}$ (*a*) and a two-dimensional display of the hydrogen potential proposed in [8] (*b*).

approach, it was found that the ground state and the first excited state in $NbH_{0.3}$ can be approximately described as harmonic [8]. The hydrogen potential, $V(x, y, z)$, for $NbH_{0.3}$ was also derived as

$$V(x,y,z) = m\omega_x^2x^2/2 + m\omega_y^2y^2/2 + m\omega_z^2z^2/2 + ez(x^2-y^2) + fx^2y^2 + g(x^2+y^2)z^2 + C_{4x}(x^4+y^4) + C_{4z}z^4 + C_{6z}z^6$$

where $\hbar\omega_x = 147$ meV, $\hbar\omega_z = 130$ meV, $e = 1.246$ eV Å^{-4}, $f = 30.77$ eV Å^{-4}, $g = -4.23$ eV Å^{-4}, $C_{4x} = 1.373$ eV Å^{-4}, $C_{4z} = -3.807$ eV Å^{-4} and $C_{6z} = 2.272$ eV Å^{-6}. However, there were a few assumptions made in this approach: that the potential also has minima at the T_2 and T_3 sites in $NbH_{0.3}$ (see figure 1); that the calculations are performed only considering diagonal terms; and that the wave function can be described by linear combinations of harmonic functions. If the actual hydrogen wave functions of the ground and excited states are, for example, extremely different from harmonic functions, the previous approach should be improved. It is, therefore, required to confirm the proposed potential and wave functions by using other approaches.

The aim of the present work was to observe the momentum transfer dependence (*Q*-dependence) of local vibrational mode intensities in $NbH_{0.3}$ and ZrH_2, and to derive the wave functions directly. In the case of an excitation energy $\gg$ kT, without any contribution from the host metal vibration, the inelastic neutron scattering intensity of the local modes of a powder sample, $I(Q, \varepsilon_n)$, is given by the transition probability from the initial state $(\phi_0(X), \exp(\mathrm{i}\boldsymbol{k}_\mathrm{i}\cdot\boldsymbol{X}))$ to the final state $(\phi_\mu(X), \exp(\mathrm{i}\boldsymbol{k}_\mathrm{f}\cdot\boldsymbol{X}))$, where $\exp(\mathrm{i}\boldsymbol{k}_\mathrm{i}\cdot\boldsymbol{X})$ and $\exp(\mathrm{i}\boldsymbol{k}_\mathrm{f}\cdot\boldsymbol{X})$ are the wave functions of the incident and scattered neutrons, respectively. $\phi_0(x)$ is the wave function of the ground state and $\phi_\mu(x)$ is that of an excited state with a transition energy from the ground state of ε_n. Since the interaction between a neutron and the hydrogen nucleus is given by a constant value $(=V_0)$, $I(Q, \varepsilon_n)$ can be expressed as

$$I(Q,\varepsilon_n) = N_0\sum_\mu\left\langle\left|\int(\phi_\mu(X)\exp(\mathrm{i}\boldsymbol{k}_\mathrm{f}\cdot\boldsymbol{X}))^*V_0\exp(\mathrm{i}\boldsymbol{k}_\mathrm{i}\cdot\boldsymbol{X})\phi_0(X)\,\mathrm{d}X\right|^2\right\rangle = AP(Q,\varepsilon_n)$$

and

$$P(Q,\varepsilon_n) = \sum_\mu\left\langle\left|\int\phi_\mu(X)\exp(\mathrm{i}\boldsymbol{Q}\cdot\boldsymbol{X})\phi_0(X)\,\mathrm{d}X\right|^2\right\rangle \tag{1}$$

where $\boldsymbol{Q} = \boldsymbol{k}_\mathrm{i} - \boldsymbol{k}_\mathrm{f}$ and $A = N_0V_0^2$. N_0 is the number of hydrogen nuclei in a sample. $\langle\cdots\rangle$

indicates averaging over the angle between $\boldsymbol{Q}$ and the direction of motion of the hydrogen. It should be noted that $I(Q, \varepsilon_n)$ is explicitly expressed in terms of the wave functions of the hydrogen. Therefore, measurements of $I(Q, \varepsilon_n)$ make possible a direct investigation of the wave functions. In the following sections we report on measurements of $I(Q, \varepsilon_n)$ for ZrH_2 and $NbH_{0.3}$, and applications of (1) for estimating their wave functions.

2. Measurements

Experiments were performed using the chopper neutron spectrometer HET at the Rutherford Appleton Laboratory. In the chopper spectrometer, the incident energy E_i was fixed and the final energy E_f was determined by the time of flight of the scattered neutrons. The energy transfer (ε) and momentum transfer ($\hbar\boldsymbol{Q}$) at a scattering angle of θ were obtained from

$$\varepsilon = E_i - E_f \qquad \hbar^2 Q^2 = E_i + E_f - 2\sqrt{E_i E_f}\cos(\theta). \tag{2}$$

In the HET, 10 detector banks were installed in the small-angle region, $3° < \theta < 7°$, and 25 detector banks were set up in the large-angle region, $10° < \theta < 30°$. Therefore, in one experiment we could measure $I(Q, \varepsilon_n)$ ($n = 1, 2, \ldots$) for 35 different values of Q. A powder sample of ZrH_2 was packed into many small holes, each with diameter 1 mm, in a boron nitride plate with 1 mm thickness (area $50 \times 50\ \mathrm{mm}^2$), in order to reduce multiple scattering, and fixed in aluminium sample holders. The sample holder was cooled down to about 20 K. A powder sample of $NbH_{0.3}$ was also packed into holes, each with a diameter of 3 mm. The incident energy used in both measurements was about 630 meV. Each neutron scattering spectrum of ZrH_2 and $NbH_{0.3}$ was obtained by subtracting the scattering from the sample holder, including the boron nitride plate, and normalised using the vanadium scattering intensity. Here no multiple-scattering correction was made.

Figure 2 shows local mode spectra of ZrH_2 observed in both the small-angle and large-angle regions. The first, second and third excitations were observed at about 147, 294, 441 meV, respectively, consistently with previous measurements [8]. Figure 3 shows typical spectra summed over the small-angle (a) and large-angle (b) regions. In this figure, it is clear that the intensities of the local modes become larger at larger angles (i.e. for higher Q). The neutron scattering intensity $I(Q, \varepsilon_n)$ can be given by $(k_i/k_f)i(Q, \varepsilon_n)/\eta(E_f)$, where $i(Q, \varepsilon_n)$ is the observed intensity of the local mode and $\eta(E_f)$ the detector efficiency. In order to achieve good statistics, the spectra observed at the two detector banks were summed, and the $i(Q, \varepsilon_n)$ ($n = 1, 2, 3$) were obtained by integrating the intensity of each local mode around the peak. Figure 4 shows the measured $I(Q, \varepsilon_n)$ for ZrH_2. Here, the $\boldsymbol{Q}$ are calculated from (2) using the centre energies of the peaks and the centre angles of the detector banks. (Note that the scattering intensities for different energy levels, $I(Q, \varepsilon_n)$, as shown in figure 4 are plotted on the same scale although the figure is given in arbitrary units.) In the case of $NbH_{0.3}$, the local mode spectrum was obtained by summing over 10 detector banks in the small-angle region and by summing over 5 detector banks in the large-angle region. Figure 5 shows typical raw data obtained by this method. One can see three peaks at 115, 160 and 220 meV, which correspond to the first excitation of the z motion, that of the x and y motions and the second excitation of the z motion. The $I(Q, \varepsilon_n)$ of $NbH_{0.3}$ were obtained by fitting their peaks to Gaussians (see figure 5), and are shown in figure 6.

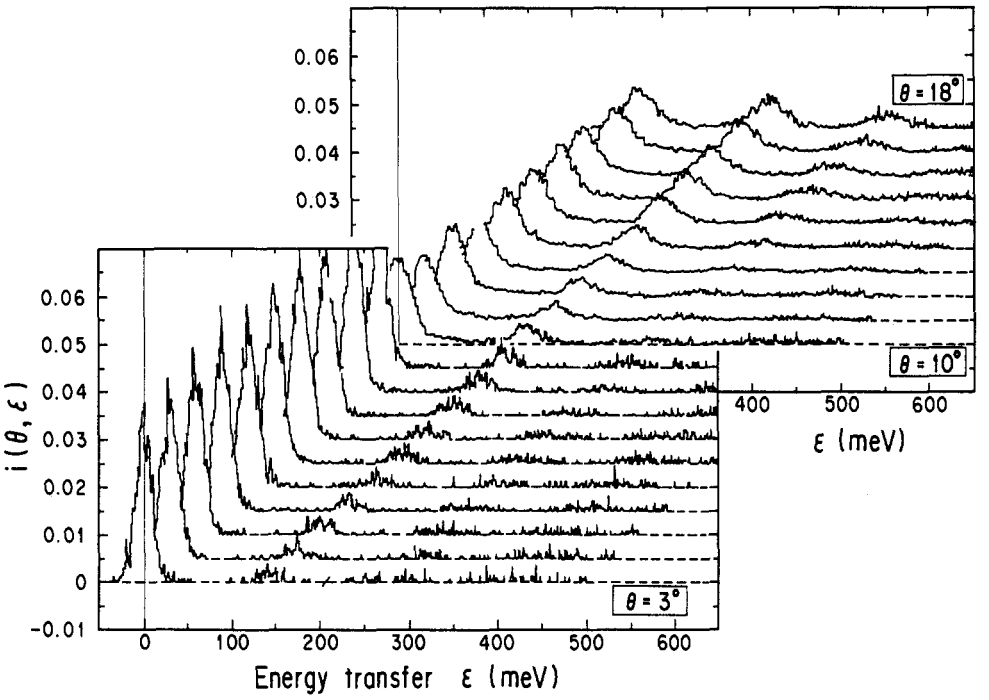

Figure 2. Neutron scattering spectra of ZrH_2 obtained from a chopper spectrometer. The 10 spectra on the left-hand side of the figure were observed in the small-angle region, and the others were observed in the large-angle region.

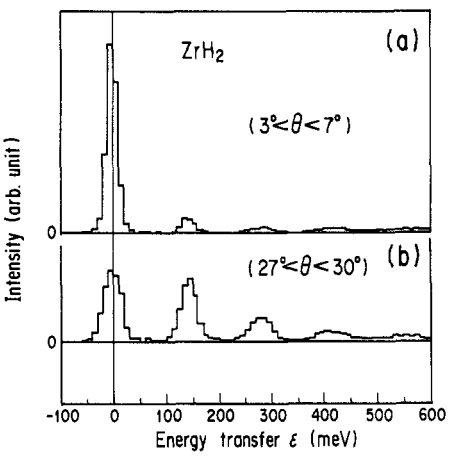

Figure 3. Typical spectra of ZrH_2 obtained at small and large angles. (*a*) Spectrum summed over the region $3° < \theta < 10°$. (*b*) Spectrum summed over the region $27° < \theta < 30°$.

3. Discussion

At the start of the present approach, we can confirm that the Q-dependence of the local modes observed using the neutron scattering spectrometer HET can be completely described by (1). We selected a powder sample of ZrH_2 as the standard sample to be

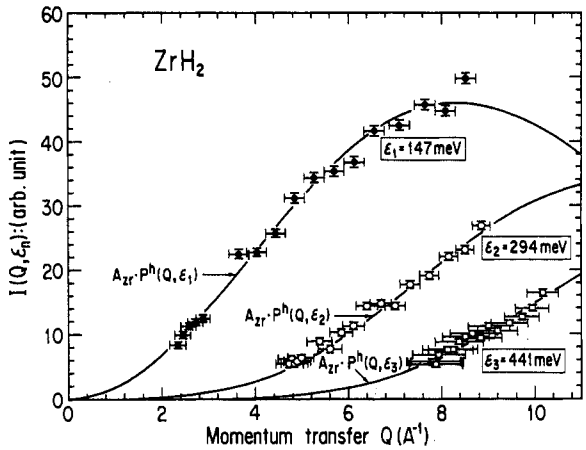

Figure 4. The neutron scattering intensity $I(Q, \varepsilon_n)$ of ZrH_2. Closed circles, open circles and open squares show observed values of $I(Q, \varepsilon_n)$ for $\varepsilon = 247$, 294 and 441 meV, respectively.

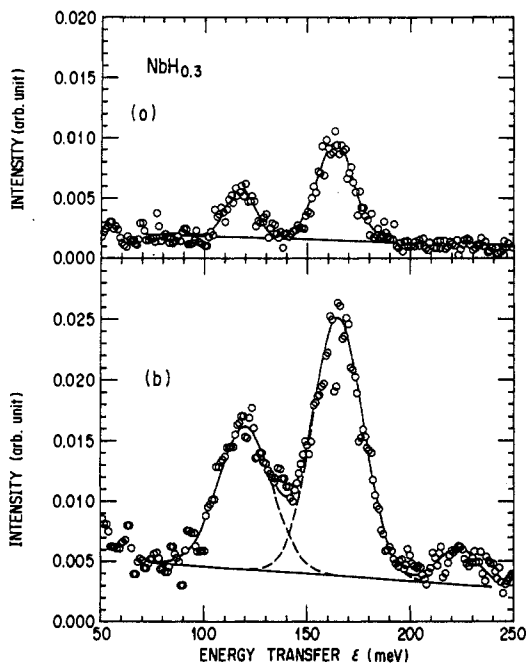

Figure 5. Typical spectra of $NbH_{0.3}$ at small and large angles. (*a*) Spectrum summed over the region $3° < \theta < 10°$. (*b*) Spectrum summed over the region $27° < \theta < 30°$. Full and broken curves indicate the results of the fitting.

used in this approach. Since the anharmonic parameter β of ZrH_2 is almost zero and no large split in the peaks at $\varepsilon = 147$, 294 and 441 meV has been observed, the hydrogen motion in ZrH_2 can be considered as being an isotropic harmonic oscillator. Therefore, the hydrogen wave functions are described as being of harmonic type, $\phi_{ijk}(X) = \Psi_i(\omega_x, x)\Psi_j(\omega_y, y)\Psi_k(\omega_z, z)$, with a normal vibration of $\hbar\omega$ $(=\hbar\omega_x = \hbar\omega_y = \hbar\omega_z) =$ 147 meV [8]. In such a simple case, one can easily calculate $P^h(Q, \varepsilon_n)$. The suffix h indicates that $P(Q, \varepsilon_n)$ in (1) is calculated using harmonic wave functions. Since the

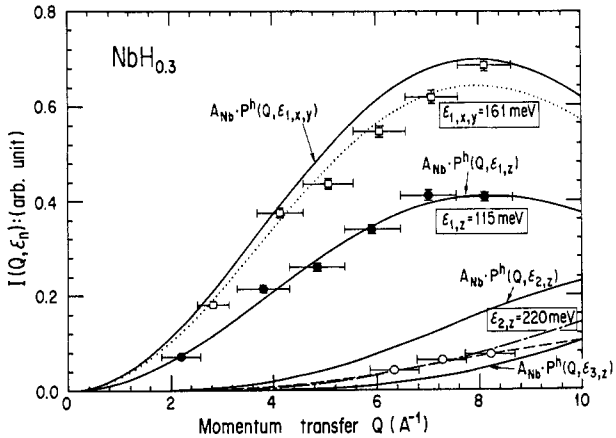

Figure 6. The neutron scattering intensity $I(Q, \varepsilon_n)$ of $NbH_{0.3}$. Closed circles, open squares and open circles show observed values of $I(Q, \varepsilon_n)$ for $\varepsilon = 115, 161$ and 220 meV, respectively.

peaks observed at $\varepsilon = 147$, 294 and 441 meV are considered to correspond to the transitions from the ground state to $i + j + k = 1, 2$ and 3 states, the Q-dependence of local modes, $I(Q, \varepsilon_n)$, can be obtained as $A_{Zr}P^h(Q, \varepsilon_n)$, where A_{Zr} is a constant for this ZrH_2 sample. The $P^h(Q, \varepsilon_n)$ $(n = 1, 2, 3)$ are derived from (1) as follows:

$$\begin{aligned} P^h(Q, \varepsilon_1 = 147\ \text{meV}) &= (Q^{*2}/2)\exp(-Q^{*2}/2) \\ P^h(Q, \varepsilon_2 = 294\ \text{meV}) &= (Q^{*4}/8)\exp(-Q^{*2}/2) \\ P^h(Q, \varepsilon_3 = 441\ \text{meV}) &= (Q^{*6}/48)\exp(-Q^{*2}/2) \end{aligned} \tag{3}$$

where $Q^* = Q/\alpha$ and $\alpha = \sqrt{m\omega/\hbar}$. It is remarkable that the Q-dependence of the transition probability for the isotropic harmonic oscillator can be scaled by $1/\alpha$. The three full curves in figure 4 indicate $A_{Zr}P^h(Q, \varepsilon_n)$ $(n = 1, 2, 3)$ calculated with $\hbar\omega = 147$ meV [8] and $A_{Zr} = 12.5$. The consistency between the measured and calculated values is very good. This result makes clear that the wave functions for the first, second and third excited states in ZrH_2 are perfectly harmonic, and strongly indicates that the wave function can be directly investigated by measurements of $I(Q, \varepsilon_n)$.

Let us apply this approach to a more general system: $NbH_{0.3}$. In this case, the three peaks observed at 115, 161 and 220 meV correspond to the first excitation of the z motion, that of the x and y motion, and the second excitation of the z motion, respectively. The results of the previous approach [8] have suggested that the wave functions of the ground and excited states can be approximately expressed using harmonic forms, $\phi_{ijk}(X) = \Psi_i(\omega_x, x)\Psi_j(\omega_x, y)\Psi_k(\omega_z, z)$, with two kinds of normal vibration: $\hbar\omega_z = 130$ meV and $\hbar\omega_x$ $(=\hbar\omega_y) = 147$ meV [8]. From (1) we can also derive $P^h(Q, \varepsilon_n)$ for the first, second and third excitations of the z motion, and the first excitation of x and y motion. These are $P^h(Q, \varepsilon_{1,z})$, $P^h(Q, \varepsilon_{2,z})$, $P^h(Q, \varepsilon_{3,z})$ and $P^h(Q, \varepsilon_{1,x,y})$:

$$P^h(Q, \varepsilon_{1,z}) = (Q^2/2\alpha_z^2)\exp(-\Delta)\tfrac{1}{2}(I_0(\gamma) + I_1(\gamma))$$

$$P^h(Q, \varepsilon_{1,x,y}) = (Q^2/2\alpha_x^2)\exp(-\Delta)(I_0(\gamma) - I_1(\gamma))$$

$$P^h(Q, \varepsilon_{2,z}) = (Q^4/8\alpha_z^4)\exp(\Delta)\tfrac{1}{4}(\tfrac{3}{2}I_0(\gamma) + 2I_1(\gamma) + \tfrac{1}{2}I_2(\gamma))$$

$$P^{\mathrm{h}}(Q, \varepsilon_{3,z}) = (Q^6/48\alpha_z^6)\exp(-\Delta)\tfrac{1}{8}(\tfrac{5}{2}I_0(\gamma) + 4I_1(\gamma) + \tfrac{3}{2}I_2(\gamma) + (8/\pi)\exp(-\gamma)B(\tfrac{3}{2}, \tfrac{5}{2})\,{}_1F_1(\tfrac{5}{2}; 4; 2\gamma) - (4/\pi)\exp(-\gamma)B(\tfrac{3}{2}, \tfrac{3}{2})\,{}_1F_1(\tfrac{3}{2}; 3; 2\gamma)) \tag{4}$$

where $\alpha_x = \sqrt{m\omega_x/\hbar}$, $\alpha_z = \sqrt{m\omega_z/\hbar}$, $\gamma = Q^2(\frac{1}{4}\alpha_z^2 - \frac{1}{4}\alpha_x^2)$ and $\Delta = Q^2(\frac{1}{4}\alpha_z^2 + \frac{1}{4}\alpha_x^2)$. $I_n(x)$ $(n = 0, 1, \ldots)$ is a modified Bessel function, ${}_1F_1$ a hypergeometric function and B a B-function. In the previous study [8], it was concluded that the wave functions for the ground and first excited state of the z motion ($\varepsilon = 115$ meV) are almost harmonic. Therefore, we calculated $A_{\mathrm{Nb}}P^{\mathrm{h}}(Q, \varepsilon_{1,z})$, using $\hbar\omega_z = 130$ meV and $\hbar\omega_x$ $(=\hbar\omega_y) =$ 147 meV obtained in a previous work [8]. The results are shown by a full curve in figure 6. Here, A_{Nb} was 36. The consistency between the measured and calculated values is fairly good. This means that the ground state and the first excited state of the z motion should be represented by harmonic functions. This is perfectly consistent with the previous result [8]. $A_{\mathrm{Nb}}P^{\mathrm{h}}(Q, \varepsilon_{1,x,y})$ and $A_{\mathrm{Nb}}P^{\mathrm{h}}(Q, \varepsilon_{2,z})$ were also calculated using the same values of $\hbar\omega_x$ $(=\hbar\omega_y)$, $\hbar\omega_z$ and A_{Nb}. These results are shown as full curves in figure 6. There is a clear difference between the calculated and measured values. This means that the wave functions of the excited states are very different from the 'normal' harmonic ones. In order to determine the difference, $0.92A_{\mathrm{Nb}}P^{\mathrm{h}}(Q, \varepsilon_{1,x,y})$ and $0.47A_{\mathrm{Nb}}P^{\mathrm{h}}(Q, \varepsilon_{2,z})$ were plotted and are shown in figure 6 as a dotted curve and a broken curve, respectively. The consistency between the modified lines and the measured values is good. This result can be explained well if the wave functions of the second excited state of the z motion and the first excited state of the x (y) motion are 'small' harmonic functions with two normal frequencies of $\hbar\omega_x$ $(=\hbar\omega_y) = 147$ meV and $\hbar\omega_z = 130$ meV, but with small amplitudes. In the previous study [8], the hydrogen potential of $NbH_{0.3}$ was classified as a trumpet-like potential and numerically estimated as $V(x, y, z)$ (see figure 1). The estimated potential $V(0, 0, z)$ is displayed with the energy levels of the ground and excited states in figure 7. This figure indicates that the potential deforms at a height of about 350 meV (from the bottom) and that excited states higher than $\varepsilon = 161$ meV exist above 350 meV although the ground state and the first excited state with $\varepsilon = 115$ meV exist below. Moreover, figure 1 shows that there are saddle points with a height of about 350 meV (from the bottom) between the T_1 site and the other T sites. It is, therefore, expected that the hydrogen waves for the excited states at energies higher than $\varepsilon =$ 161 meV can 'escape' from the T_1 site to the T_2 and T_3 sites or, at least, change from being harmonic. Assuming a linear combination of one-dimensional harmonic wave functions, $\varphi_i(x) = p\Psi_i(\omega, x) + q\Psi_i(\omega, x - a)$, we will calculate the Q-dependence of

$$P_i(Q) = \left| \int \varphi_i(x)\exp(\mathrm{i}\boldsymbol{Q}\cdot\boldsymbol{x})\Psi_0\,\mathrm{d}x \right|^2.$$

Here, $p^2 + q^2 = 1$ and a is the distance between T sites. $P_1(Q)$ is expressed as

$$P_i(Q) = \left| \int \varphi_1(x)\exp(\mathrm{i}\boldsymbol{Q}\cdot\boldsymbol{x})\Psi_0(\omega, x)\,\mathrm{d}x \right|^2$$
$$= P_1(\mathrm{normal})[p^2 + q^2(1 + \alpha^4a^2/Q^2)\exp(-\alpha^2a^2/2) + 2pq(\cos(aQ/2) - \alpha^2a/Q\sin(aQ/2))\exp(-\alpha^2a^2/4)] \tag{5}$$

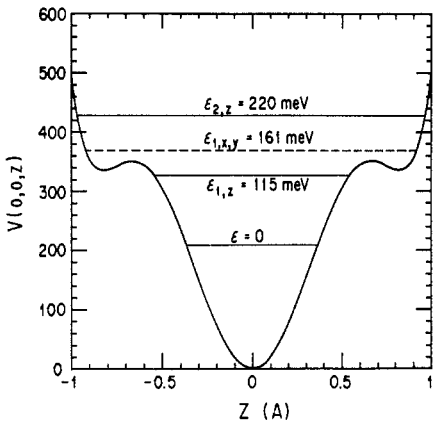

Figure 7. The hydrogen potential and excited level in $NbH_{0.3}$. The full lines of the energy levels indicate the ground state ($\varepsilon = 0$) and the excited states of the z motion ($\varepsilon = 115$ and 220 meV), and the broken line the excited state of x (y) motion ($\varepsilon = 161$ meV).

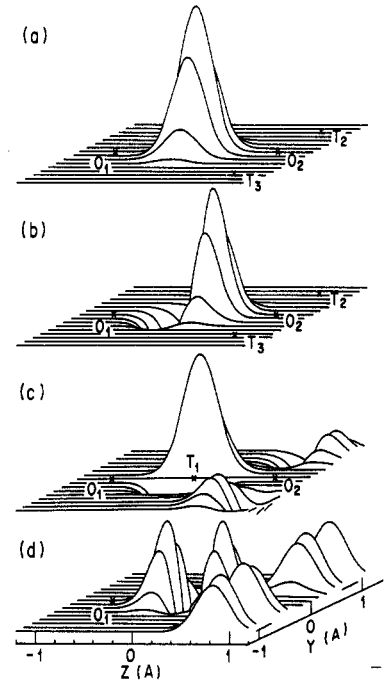

Figure 8. Hydrogen wave functions in $NbH_{0.3}$. (*a*) ground state; (*b*) excited state of $\varepsilon = 115$ meV; (*c*) excited state of $\varepsilon = 161$ meV; (*d*) excited state of $\varepsilon = 220$ meV.

where $\alpha = \sqrt{m\omega/\hbar}$. P_1(normal) is $Q^2/2\alpha^2 \exp(-Q^2/2\alpha^2)$, which is the transition probability of a normal harmonic oscillator without 'escape'. If $a = 1.155$ Å and $\hbar\omega = 130$ meV (in the case of $NbH_{0.3}$), $P_1(Q)$ can be approximated as

$$P_1(Q) = P_1(\text{normal})\, p^2(1 + O(10^{-2})) \qquad (\text{for } Q > 1\ \text{Å}^{-1}). \tag{6}$$

Generally, a relation similar to (6) can be obtained for $P_i(Q)$ ($i = 2, 3, \ldots$). It indicates that the probability of transition to an excited state, $\varphi_i(x) = p\Psi_i(\omega, x) + q\Psi_i(\omega, x - a)$, has a Q-dependence analogous to that of the normal case, although the amplitude is decreased by a factor p^2. This feature is just that of $I(Q, \varepsilon = 160\ \text{meV})$ and $I(Q, \varepsilon = 220\ \text{meV})$ observed for $NbH_{0.3}$. It may therefore be reasonable to define the excited states due to $\varepsilon = 160$ and 220 meV, $\varphi_1^x(X)$ (and $\varphi_1^y(X)$) and $\varphi_2^z(X)$, by $p\phi_{ijk}(X) + q\phi_{ijk}(X - X_2) + q\phi_{ijk}(X - X_3)$, where $p^2 + 2q^2 = 1$ and X_2 and X_3 are the coordinates of the T_2 and T_3 sites. Since the values obtained for p^2 for $\varepsilon = 160$ and 220 meV are 0.92 and 0.47, respectively, their wave functions should be described as

$$\varphi_1^x(X) = 0.96\phi_{100}(X) + 0.2\phi_{100}(X - X_2) + 0.2\phi_{100}(X - X_3)$$

and

$$\varphi_2^z(X) = 0.69\phi_{002}(X) + 0.51\phi_{002}(X - X_2) + 0.51\phi_{002}(X - X_3) \tag{7}$$

where $\phi_{ijk}(X) = \Psi_i(\omega_x, x)\Psi_j(\omega_y, y)\Psi_k(\omega_z, z)$, $\phi_{ijk}(X - X_2) = \Psi_i(\omega_x, z - b)\Psi_j(\omega_y, y)\Psi_k(\omega_z, x - b)$ and $\phi_{ijk}(X - X_3) = \Psi_i(\omega_x, -z - b)\Psi_j(\omega_y, y)\Psi_k(\omega_z, -x - b)$.

Here, b is 0.825 Å. The proposed hydrogen wave functions on the $x = 0$ plane are shown in figure 8. From these proposed wave functions, the same values as for the dotted and broken curves shown in figure 6 can also be obtained. These results indicate that it is possible to propose (7) as the wave function for $\varepsilon = 161$ and 220 meV. Note that the value of p in $\varphi_1^x(X)$ is approximately 1. That the wave function for $\varepsilon = 161$ meV is approximately harmonic is not so very different from the previous result [8]. Sugimoto and Fukai [9] assumed a double Born–Mayer potential and calculated the wave functions for the ground and excited states (Ψ_0, Ψ_1^x and Ψ_1^y in [9]) by the method of Kimball and Shortley [10]. Their results (figure 3(a) and (b) in [9]) also show that the small portion of the hydrogen wave corresponding to $\varepsilon = 161$ meV exists at the neighbouring pair of T sites, although the ground state and the first excited state corresponding to $\varepsilon =$ 115 meV are completely localised at the original T site. The feature of 'escape' at $\varepsilon =$ 161 meV estimated by the present measurement corresponds to their result very well.

Since the wave functions for $\varepsilon = 220$ meV, unfortunately, have not been explicitly discussed, we cannot here compare our result with the others. Note that the wave functions for $\varepsilon = 220$ meV are still not identified exactly by the present measurements. For example, if $\varphi_2^z(X)$ is given by a 'mixture' state $r\phi_{002}(X) + s\phi_{003}(X)$, $I(Q, \varepsilon_n =$ 220 meV) should be expressed as $r^2 A_{\mathrm{Nb}} P^{\mathrm{h}}(Q, \varepsilon_{2,z}) + s^2 A_{\mathrm{Nb}} P^{\mathrm{h}}(Q, \varepsilon_{3,z})$, where $r^2 + s^2 =$ 1. The chain curve in figure 6 shows calculated values for the case where $r^2 = 0.3$. In order to identify it exactly, one must observe the Q-dependence in a wider Q-range, for example, $1 < Q < 12$ Å^{-1} (see figure 6). However, the present measurement at least suggests that the wave function for $\varepsilon = 220$ meV is very different from the simple harmonic wave function, and that it should be calculated by a more exact method.

Generally, if one wants to obtain exact wave functions from the local mode spectrum, one must observe many local mode peaks, assume a very complicated potential with many parameters and calculate the energy levels with a large linear combination of the harmonic wave functions. Since the wave functions are indirectly determined under the many assumptions used in this procedure, it seems difficult to investigate their exact features. In principle, our present approach makes a direct investigation of the wave function possible. This point is a big advantage and the best use of this may be in ascertaining whether the wave functions proposed on the basis of other experimental results and theories are appropriate or not.

In this paper we reported on the Q-dependence of local modes, confirmed that the hydrogen wave functions for the first, second and third excited states in ZrH_2 are completely harmonic, and proposed for the first time the wave functions due to the higher excited state of $NbH_{0.3}$. Our results suggest that the measurement of the Q-dependence is very useful for confirmation or estimation of wave functions.

Acknowledgments

The measurements were performed as a test experiment under the UK–Japan collaboration. We wish to offer many thanks to Professor N Watanabe and Professor A J Leadbetter for their kindness as regards the arrangements of the experiment.

References

[1] Kai K, Ikeda S, Fukunaga T, Watanabe N and Suzuki K 1983 *Physica* B **120** 342

[2] Richter D 1984 *Proc. Workshop on High Energy Excitation in Condensed Matter (Los Alamos, 1984)* LA-10227 p 559
[3] Richter D and Shapiro S M 1980 *Phys. Rev.* B **22** 599
[4] Richter D, Rush J J and Rowe J M 1983 *Phys. Rev.* B **27** 6227
[5] Ikeda S, Watanabe N and Kai K 1983 *Physica* B **120** 131
[6] Hempelmann R, Richter D and Kollmar A 1981 *Z. Phys.* B **44** 159
[7] Eckert J, Goldstone J A, Tonks D and Richter D 1983 *Phys. Rev.* B **27** 1980
[8] Ikeda S and Watanabe N 1987 *J. Phys. Soc. Japan* **56** 565
[9] Sugimoto H and Fukai Y 1981 *J. Phys. Soc. Japan.* **50** 3709
[10] Kimball G E and Shortley G H 1934 *Phys. Rev.* **45** 815

HYDROGEN VIBRATION IN CUBIC DIHYDRIDES MH_2 (M=Ti, Zr), AND LOCALIZATION IN CUBIC LAVES PHASES $ZrM_2H_{1/2}$ (M=V, Cr, Fe, Co)

C. ELSÄSSER*, S. SCHWEIZER**, M. FÄHNLE**
* Institut für Werkstoffwissenschaft, Max-Planck-Institut für Metallforschung, Seestrasse 92, D-70174 Stuttgart, Germany; ** Institut für Physik, Max-Planck-Institut für Metallforschung, Heisenbergstrasse 1, D-70569 Stuttgart, Germany.

ABSTRACT

A study of cubic dihydrides TiH_2 and ZrH_2 and of H in cubic Laves-phase compounds by means of ab-initio total-energy calculations in the local density-functional approximation is presented. First, for optic vibrational modes in the two dihydrides the calculated local potentials and excitation energies are compared to experimental results obtained by inelastic neutron scattering. Second, the relative stabilities of H on three types of interstitial sites in the cubic Laves-phase compounds, denoted by b, e and g, are investigated. Theoretically, a preference of g sites is found for M=V, Cr, and of e sites for M=Fe, Co. These results are discussed with respect to experimental observations and to empirical criteria for H accomodation in transition-metal compounds.

INTRODUCTION

The quantitative determination of occupied interstitial sites and excitation spectra with corresponding potentials for vibrations of light particles like hydrogen isotopes absorbed in metal lattices has been a topic of research for many years. (For reviews on metal-hydrogen systems we refer to the books [1], [2] and [3].) Experimentally, most informations were obtained via inelastic neutron scattering (INS) techniques, in which the excitation energies for transitions from the vibrational ground state (zero-point motion) to excited states can be measured directly (see, e.g., ch. 3 in [2], vol. II). The shapes of the local potential wells were usually determined from the measured excitation energies under the assumption that the vibrations are only weakly anharmonic and, hence, can be treated via first-order perturbation theory (see, e.g., ch. 4 in [3]).

The quantitative theoretical prediction of the vibrational potentials and the resulting quantum states for H isotopes in metals without the assumption of weak anharmonicity is now possible by means of ab-initio total-energy calculations based on the local-density-functional theory [4]. For instance, Ho et al. [5] have calculated the vibrational spectra of H in body-centered cubic (bcc) Nb with excitation energies in very good agreement with INS data. Similar calculations for H states in face-centered cubic (fcc) Pd were done by Elsässer et al. [6]. They found that the vibrations can be strongly anharmonic and anisotropic, and they demonstrated the limitations of the common practice of perturbation theory to obtain informations about the potential shapes from INS spectra. Their prediction of a noticeable threefold splitting of the second excited state because of strong anharmonicity and anisotropy, for which there was no evidence in the INS data available then, has been confirmed in a more recent INS experiment [7].

Based on these two paradigmatic metal hydrides, NbH and PdH, a systematic investigation of vibrational quantum states of H isotopes in transition metals (hexagonal close-packed (hcp) Zr and Ti; bcc Nb, Cr and $\alpha - Fe$; fcc Pd, Ni and $\gamma - Fe$) and intermetallic compounds ($FeTi$ and $NiTi$) [8] using an ab-initio mixed-basis pseudopotential method [9] has led to a quantitative microscopic insight into the local interstitial H environments through the transition-metal series. In the present contribution, after a short outline of the computational method, results of ab-initio calculations for vibrational states of protons in the cubic dihydrides ZrH_2 and TiH_2 are presented as one example. As a second example the occupation of intersitital sites by protons in the cubic Laves-phase compounds $ZrM_2H_{1/2}$, with M=V, Cr, Fe, Co, is discussed [10].

Mat. Res. Soc. Symp. Proc. Vol. 453 © 1997 Materials Research Society

COMPUTATIONAL METHOD

The calculation of quantum-mechanical states of a transition-metal–hydrogen system can be decoupled into three steps because of large mass differences between the three constituents, i.e. light electrons, H nuclei and heavy metal ions (Born-Oppenheimer approximation).

In the first step, total energies are calculated with the metal ions and the H nuclei placed and fixed at specific positions in the unit cell of a crystal. The electronic structure of the (valence) electrons is calculated using the local density-functional approximation [4]. The interactions between the metal ions and the electrons are incorporated by non-local norm-conserving ionic pseudopotentials [11]. A local pseudopotential is used for the interaction of the electrons with the H nuclei [6]. Perfect translational symmetry of the crystals is assumed by using Born-von-Kármán boundary conditions, and the Bloch electron states are represented by a mixed basis set [9] containing a limited but for the considered properties sufficiently large number of plane waves and a few atom-centered functions constructed from atomic pseudowavefunctions and strictly confined to muffin-tin spheres. Integrals over the electron Brillouin zone are calculated by sampling and Gaussian broadening [12]. In the second step, quantum states of the H nuclei in the electron gas and the rigid lattice of metal ions are calculated. With a choice of crystal unit cells in the first step, which describe frozen displacements of the H and metal sublattices relative to each other according to normal modes of the crystal, this problem reduces to solutions of a single-particle Schrödinger equation. The "particles" move in Born-Oppenheimer or "adiabatic" potentials, which are mapped out by the total energies from the first step [5]. These vibrations belong to optic modes at the center of the phonon Brillouin zone (Γ point). For the third step, at the Γ point acoustic vibrations of the crystal have zero energy (rigid-body translations) and thus require no further computation.

It is essential to map out accurately the adiabatic potentials by ab-initio total-energy calculations for sufficiently many different H positions in the unit cell (e.g. 51 for ZrH_2 and 162 for $ZrFe_2H_{1/2}$).

HYDROGEN IN CUBIC DIHYDRIDES

By loading with hydrogen the fcc transition metals Pd and Ni can form stoichiometric monohydrides, PdH and NiH, where all octahedral interstitial sites of the fcc metal lattices are filled with H atoms (cf. the $NaCl$ structure). The hcp transition metals Ti, Zr and Hf, on the other hand, can be converted to stoichiometric dihydrides, TiH_2, ZrH_2 and HfH_2, with fcc lattices, in which all tetrahedral interstitial sites are occupied by H atoms (cf. the CaF_2 structure).

Experimentally, Ikeda et al. [13] measured excitation spectra of H vibrations in cubic TiH_2 and $ZrH_{1.41}$ as well as in tetragonally distorted $ZrH_{1.93}$ by means of inelastic neutron scattering (INS) over an energy range of 1 eV with a relative energy resolution of about 2 % . These INS spectra are quantitatively very similar and exhibit up to five distinct lines. The lines are spaced almost equidistantly in energy, like for a particle in a harmonic potential well, and the spaces become slightly smaller towards higher energies because of a weak anharmonicity.

Theoretically, in the present work [8] the vibrational H states were calculated for the normal modes at the Γ point of the phonon Brillouin zone of fcc dihydrides. Besides the rigid-body translations of the crystal, the three acoustic Γ modes, there are six optic modes because of the three atoms per formula unit. In one set of three optic modes the two H sublattices move in phase relative to the metal sublattice. The corresponding adiabatic potential has the symmetry of a simple cubic (sc) lattice with half of the lattice constant of the fcc metal lattice (called "sc" modes in the following). In the other set of three optic modes the two H sublattices move in antiphase relative to the metal sublattice at rest, leading to an adiabatic potential with fcc symmetry and the same lattice constant as the metal sublattice (called "fcc" modes).

The adiabatic potentials, i.e. ab-initio total energies as function of H sublattice displacements δ from the tetrahedral positions of the metal sublattice along high-symmetry directions in the cubic crystal according to the two optic modes in ZrH_2 (whose calculated lattice constant is a=4.79Å) are displayed in figure 1. (The corresponding curves for TiH_2, with a=4.38Å, are quantitatively very similar.) For small relative displacements δ/a the adiabatic potential curves of both optic modes nearly coincide and form local potential wells with almost isotropic and harmonic shapes. Anharmonicity and anisotropy become obvious for energies above 0.3 eV.

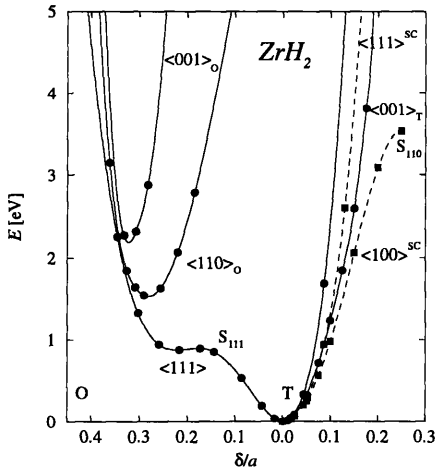

Figure 1: Adiabatic potentials for both types of optic Γ modes of ZrH_2: Energy change E as function of relative displacements δ/a (a=4.79Å is the equilibrium lattice constant). For δ=0 both H sublattices are located at tetrahedral sites T of the fcc Zr lattice. The ab-initio data are marked by black symbols and connected by cubic spline curves: circles and solid lines for the fcc modes, squares and broken lines for the sc modes. $< \ldots >$ denote directions in a cubic crystal. The subscripts T and O mark directions passing through tetrahedral or octahedral sites, respectively. The superscript sc indicates the two directions of the sc modes. Left at $\delta=\sqrt{3}/4$ both H sublattices come together at an octahedral site O. S_{111} and S_{110} mark saddle points in the adiabatic potentials.

Vibrational H states were calculated by solving a single-particle Schrödinger equation for H isotopes moving in the two adiabatic potentials. The resulting excitation energies for protons in ZrH_2 are displayed in figure 2. (Again the results for TiH_2 are almost the same.) For better comparison with the INS spectra, densities of states (DOS) were formed from the discrete Γ-point energy levels ε_ν by broadening with Gaussians, whose width Δ_ν was chosen to be $\Delta_\nu/\varepsilon_\nu$=2% to mimic the energy resolution of an INS spectrometer [13]. The positions of the peak maxima can be compared to those in the measured INS spectra. (The calculated peak heights and experimental intensities, however, should not be compared directly because transition matrix elements between different states were not included in the calculated DOS.) In the INS experiment both types of optic modes are excited, and in general a vibration is a superposition of the two modes. Consequently the INS spectra can be imagined as being formed from a superposition of both DOS. The sharpness of the INS peaks may be attributed to the sc modes, and some fine structures to the fcc modes (except for a tetragonal splitting in the case of $ZrH_{1.93}$ [13]).

In table 1 the peak-maximum positions of the sc modes and of the INS spectra are compared for ZrH_2 and TiH_2. The quantitative agreement between experiment and theory is very good for the lowest excitation. The almost equidistant spacing due to the nearly harmonic potential is also well reproduced. The influence of the weak anharmonicity, however, leads to slightly smaller intervals between the higher excitation lines in the INS spectra, whereas in the DOS the intervals are increasing, but by a smaller amount. This can partly be attributed to the numerical representation of the adiabatic potential and the solution of the Schrödinger equation in a plane-wave basis. Part of the deviation may also be due to the fact that in the INS experiment the intensity decreases strongly with energy, and the peak maxima become less sharp. Within these considerations, however, it can be stated that both ab-initio theory and INS experiment yield the same microscopic picture: The

lowest six excited H vibrational states originate from almost harmonic and isotropic local potential wells in the cubic dihydrides. This behaviour is different from the case of cubic monohydrides like PdH and NiH, where strong anharmonicities and anisotropies are noticeable for the lowest two excitation states [6,8].

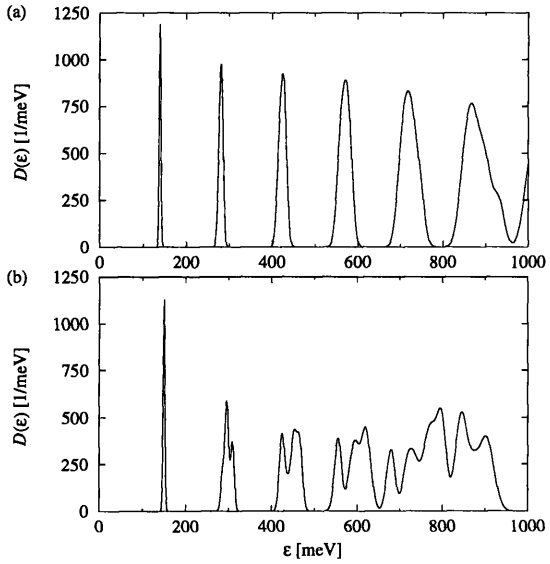

Figure 2: Densities of states of vibrations for protons in ZrH_2, formed by broadening the calculated discrete energy levels ε_ν with Gaussians of relative width $\Delta_\nu/\varepsilon_\nu$=2% : (a) sc modes; (b) fcc modes.

Table 1: Comparison of the energies of the line maxima, as multiples of the first excitation energy, in the calculated DOS of sc-modes and in the measured INS spectra of ZrH_2 and TiH_2 (energies in meV; the experimental data were obtained from equation (2) in [13], with parameters for the harmonic frequency and the anharmonicity quoted there).

line	ZrH_2 sc modes	$ZrH_{1.41}$ INS [13]	TiH_2 sc modes	TiH_2 INS [13]
1	140	140	148	143
2	281≈ 2·141	274≈ 2·137	298≈ 2·149	281≈ 2·141
3	426≈ 3·142	400≈ 3·133	450≈ 3·150	414≈ 3·138
4	571≈ 4·143	519≈ 4·130	604≈ 4·151	542≈ 4·136
5	718≈ 5·144	632≈ 5·126	759≈ 5·152	666≈ 5·133

HYDROGEN IN CUBIC LAVES PHASES

Cubic Laves phases are binary intermetallic compounds AB_2 with a fcc Bravais lattice and an atomic basis of two species, where atoms of species A are located on a sublattice with diamond structure, i.e. the regular fcc-lattice sites and one of the two tetrahedral-site sublattices. Each four atoms of species B form regular tetrahedra centered at the other tetrahedral-site sublattice. Within this structure there are three types of interstitial sites, which can be occupied by H isotopes (see, e.g., ch. 4 in [2], vol. I): The b sites are formed by B_4 tetrahedra, the e sites by AB_3 and the g sites by A_2B_2. Per formula unit there are one b, four e and twelve g sites. All these sites constitute a complex network for hydrogen diffusion.

In this work [10] cubic Laves phases with A=Zr and a series B=V, Cr, Fe, Co are investigated. The compounds ZrV_2 and $ZrCr_2$ are able to accomodate considerable amounts of H, e.g. up to ZrV_2H_6, and rather detailed experimental informations are available for these model systems of H storage materials. For instance, H occupies the g sites [14], whereas the b sites can be excluded

because of its much smaller local volume. Also no evidence for e-site occupations was found. Empirical rules were formulated to rationalize these observations (see, e.g. [15,16]). The "chemical" criterion states that sites surrounded by as much Zr as possible are preferred because pure Zr forms more stable hydrides than pure V, Cr, Fe or Co. According to the "geometrical" criterion the interstitial site with the largest local volume is preferred. These rules as well as empirical heat-of-solution calculations [17] lead to the general expectation that g sites should always be preferred in ZrM_2 Laves phases.

The compounds $ZrFe_2$ and $ZrCo_2$ absorb less amounts of H, e.g. $ZrFe_2H_{1/2}$, and hence are not very relevant materials for H storage. Scientifically, however, studies of these materials are important because neutron diffraction experiments on hydrogenated $ZrFe_2$ by Rudnev et al. [18] gave evidence that e instead of g sites are occupied by H. This result, which is in contradiction to all experience and empirical rules for Laves-phase hydrides ZrM_2H_x, is commonly considered suspect [17] and thus deserves further clarification.

The topic of our work is an investigation of energy differences between the three sites for H in the series of Laves-phase compounds via ab-initio total-energy calculations for the formula unit $ZrM_2H_{1/2}$, with one H atom per fcc unit cell. In the calculations structural relaxations were included in several steps, starting from the H atom located at the geometrical center of each one of the three sites in the ideal lattice of ZrM_2, and ending with the unit-cell volume and with all atomic positions fully relaxed. Zero-point energies of H at the three sites in $ZrCr_2$ and $ZrFe_2$ were obtained by calculating vibrational H states in adiabatic potentials of optic Γ modes of the H sublattice in the same manner as for the dihydrides in the previous section.

The first result, in accordance with all previous experience, is that b-site occupations can be ruled out because of considerably higher (potential-minimum + zero-point) energies of proton states centered at b sites. For the other two sites, it turned out that in volume-relaxed unit cells the g site is energetically preferred over the e site, as expected, by 0.34 eV and 0.31 eV in ZrV_2 and $ZrCr_2$, respectively. In $ZrFe_2$ and $ZrCo_2$, however, the e sites were found to be energetically lower than the g sites by 0.15 eV. Despite all further effects of relaxation and zero-point motion for $ZrFe_2H_{1/2}$, the g-e energy difference remained at 0.11 eV in favour of the e site, giving theoretical support to the experimental observation of Rudnev et al. [18].

To understand this behaviour a detailed analysis of the atomic and electronic structures was deemed necessary [10]. In the ZrM_2 series with M from V to Co the local interstitial-site volumes shrink, but by H addition the crystal cohesion becomes stronger. For M=V, Cr the metal atoms Zr and M have similar valence-electron structures. Hence the type of neighboring atoms to an interstitial site is not so important. The decisive feature here is the local volume, and this makes the g sites most preferable. For M=Fe, Co the Zr and M atoms have more different electron configurations. First, Fe and Co are more electronegative than Zr. This leads to greater delocalization of Zr-centered electron states, and the Zr atoms loose some attraction to H. Second, because of the higher number of valence electrons, antibonding d orbitals are additionally filled in $ZrFe_2$ and $ZrCo_2$. Some depletion of these antibonding states of M-M pairs by the addition of H makes the strengthening of the crystal cohesion plausible. A larger number of neighboring M-M pairs from which antibonding electrons can be taken to screen the H atom, seems to be more important than the smaller local volume. This is further supported by the result that the energetic separation in the adiabatic potential between the b site with four surrounding M atoms and the g site with two M atoms is reduced from 1.25 eV in $ZrCr_2H_{1/2}$ to 0.58 eV in $ZrFe_2H_{1/2}$. But the b site is so small that here electronic effects are not yet sufficient to overcome the volume constraint.

Altogether, our ab-initio study shows that a change of the most stable interstitial site for H in cubic Laves-phase compounds may happen from the g site in $ZrCr_2$ to the e site in $ZrFe_2$. The results of total-energy calculations can be rationalized by changes in the electronic structure. They support the experimental observation of Rudnev et al. [18] for H in $ZrFe_2$ and predict the same behaviour for $ZrCo_2$.

SUMMARY

In the present contribution the capability of ab-initio total-energy techniques for studies of microscopic structural and vibrational properties of metal–hydrogen compounds has been illustrated by two examples. In the first example vibrational quantum states of protons in transition-metal dihydrides were calculated, giving excitation energies, which agree well with INS spectra, and detailed information about the shape of the underlying local vibrational potentials. In the second example significant differences in the interstitial-site preference of H in cubic Laves-phase compounds were found, which may help to reconsider the ranges of validity of commonly used empirical rules.

ACKNOWLEDGEMENTS

The authors gratefully acknowledge valuable discussions with K. M. Ho and C. T. Chan, enabled through the NATO collaborative research grant No. 910439.

REFERENCES

[1] Hydrogen in Metals, edited by G. Alefeld and J. Völkl, volumes I+II, Springer, Berlin, 1978.
[2] Hydrogen in Intermetallic Compounds, edited by L. Schlapbach, volumes I+II, Springer, Berlin, 1988 and 1992.
[3] Y. Fukai, The Metal-Hydrogen System, Springer, Berlin, 1993.
[4] P. Hohenberg and W. Kohn, Phys. Rev. **136**, B864 (1964); W. Kohn and L. J. Sham, Phys. Rev. **140**, A1133 (1965).
[5] K.-M. Ho, H.-J. Tao and X.-Y. Zhu, Phys. Rev. Lett. **53**, 1586 (1984); H.-J. Tao, K.-M. Ho and X.-Y. Zhu, Phys. Rev. B **34**, 8394 (1986).
[6] C. Elsässer, K. M. Ho, C. T. Chan and M. Fähnle, Phys. Rev. B **44**, 10377 (1991); C. Elsässer, K. M. Ho, C. T. Chan and M. Fähnle, J. Phys.: Condens. Matter **4**, 5207 (1992).
[7] A. I. Kolesnikov, I. Natkaniec, V. E. Antonov, I. T. Belash, V. K. Fedotov, J. Krawczyk, J. Mayer and E. G. Ponyatovsky, Physica B **174**, 257 (1991).
[8] C. Elsässer, Ab-initio-Elektronentheorie für Übergangsmetall-Wasserstoff-Verbindungen, Habilitationsschrift, Universität Stuttgart, 1994 (in german).
[9] S. G. Louie, K.-M. Ho and M. L. Cohen, Phys. Rev. B **19**, 1774 (1979); C. Elsässer, N. Takeuchi, K. M. Ho, C. T. Chan, P. Braun and M. Fähnle, J. Phys.: Condens. Matter **2**, 4371 (1990).
[10] S. Schweizer, Ab-initio-Berechnung der Eigenschaften von Wasserstoff in kubischen Laves-Phasen, Dissertation, Universität Stuttgart, 1995 (in german).
[11] D. R. Hamann, M. Schlüter and C. Chiang, Phys. Rev. Lett. **43**, 1494 (1979); D. Vanderbilt, Phys. Rev. B **32**, 8412 (1985).
[12] C.-L. Fu and K.-M. Ho, Phys. Rev. B **28**, 5480 (1983).
[13] S. Ikeda and N. Watanabe, Physica **120**B, 131 (1983); S. Ikeda and N. Watanabe, J. Phys. Soc. Japan **56**, 565 (1987).
[14] J. Didisheim, K. Yvon, P. Fischer and D. Shaltiel, J. Less-Common Met. **73**, 355 (1980); D. Fruchart, A. Rouault, C. Shoemaker and D. Shoemaker, J. Less-Common Met. **73**, 363 (1980).
[15] D. G. Westlake, J. Less-Common Met. **91**, 1 (1983).
[16] D. G. Ivey, D. O. Northwood, J. Mater. Sci. **18**, 321 (1983).
[17] I. Jacob and D. Shaltiel, J. Less-Common Met. **65**, 117 (1979).
[18] I. I. Rudnev, V. N. Bykov and V. I. Shcherbak, Fiz. Metal. Metalloved. **34**, 856 (1972).

Neutron-scattering study of the impulse approximation in ZrH_2

A. C. Evans* and D. N. Timms
Division of Physics, Portsmouth University, Park Building, King Henry I Street, Portsmouth PO1 2DZ, United Kingdom

J. Mayers and S. M. Bennington
Rutherford Appleton Laboratory, Chilton, Didcot, Oxfordshire OX11 0QX, United Kingdom
(Received 14 August 1995)

We report inelastic-neutron-scattering measurements of the neutron Compton profile, $J(y)$ in polycrystalline ZrH_2 over a range of momentum transfers between 35 and 109 $Å^{-1}$. The measurements were performed using an inverse geometry spectrometer at a pulsed-spallation neutron source. The experimental results are compared with simulations calculated from a measurement of the density of states of the hydrogen vibrations in ZrH_2. Deviations from impulse approximation (IA) scattering and a form of the IA proposed by Stringari have been investigated. The deviations are manifest as both an asymmetry and a shift in centroid of $J(y)$. Both effects become less significant as the momentum transfer is increased and the IA limit is approached. At high momentum transfers the symmetrization procedure of Sears successfully removes final-state effects from these data. We conclude that the neutron Compton scattering technique can provide accurate information about the behavior of tightly bound proton systems such as ZrH_2.

I. INTRODUCTION

In recent years neutron Compton scattering (NCS) or deep inelastic neutron scattering (DINS) has become established as a technique for probing directly the momentum distribution of atoms in a variety of condensed matter systems. The technique was suggested by Hohenberg and Platzmann[1] almost 30 years ago and is analogous to the measurement of electron momentum by Compton scattering.[2] As with Compton scattering, the interpretation is based on the validity of the impulse approximation (IA) which is exact when both the energy and momentum transferred to the target atom are infinite.[3] Deviations of the dynamic scattering function from that derived under the IA occur at finite values of the momentum transfer **q**. Those arising as a consequence of the scattered neutron interacting with neighboring atoms are known as final-state effects (FSE's) while those arising from the bound state of the atom are known as initial-state effects (ISE's).[4] The question of when the IA may be deemed valid is still a matter of contention. A number of theories have been developed for calculating the form and magnitude of departures from the IA in helium[5–7] and Sears[8] has developed a treatment for FSE's which is applicable to a wide range of systems. It has been shown[9] that ISE's become significant at low temperatures and in quantum systems they are largely responsible for observed deviations from IA behavior. In nonquantum systems the IA is reached when the momentum transfer to the atom far exceeds the root-mean-square momentum of the atom. The derivation of the IA makes two assumptions. The first is that the momentum transfer is sufficiently large for the scattering to be incoherent and the second is that the struck atom gains sufficient energy from the neutron that its recoil appears to be that of a "free" atom. Deviations from the IA are usually attributed to FSE's but Stringari[10] pointed out that the standard form of the IA does not correctly treat the bound nature of the initial state. In this paper we examine the validity of the IA in zirconium hydride (ZrH_2) and test a form of the IA proposed by Stringari.

The NCS technique has already proved successful in determining atomic momentum distributions and in obtaining directly values for the mean atomic kinetic energies of a number of light elements, for example, solid[11,12] and liquid helium,[13,14] other noble gases in both solid and liquid phases,[15,16] hydrogen bonds,[17,18] metals,[19] liquid and solid hydrogen,[20] glasses,[21] and graphite.[22] Deviations from the IA are most significant at lower **q** where the spectrum of scattered neutrons does not exhibit the characteristic features expected for recoil scattering from a "free" target atom. For example, the determined momentum distribution is neither symmetric nor centered at zero momentum and interpretation follows the application of detailed correction procedures. Deviations from the IA are reduced by moving to larger **q** but they are not eliminated. Experiments on superfluid helium-4 performed with $\mathbf{q}>50$ $Å^{-1}$ still fail to observe the sharp signature expected for the Bose condensate fraction, showing that FSE's are still present.[23] Despite the theoretical interest in this subject experimental investigations are limited to helium and other noble gas systems.

High momentum transfers can be achieved with inverse-geometry spectrometers receiving electron-volt neutrons from pulsed-spallation neutron sources. Electron-volt spectroscopy is still in its infancy and as the reliability and accuracy of the technique improves the interpretation of results will become more reliant on the procedures used to correct for FSE's. Accurate measurements on tightly bound proton systems such as molecular hydrogen are only possible with electron-volt spectroscopy where energy transfers much greater than the vibrational frequency of the molecule are required before the IA can be reliably used to determine $n(\mathbf{p})$. A comprehensive assessment of the validity of the IA is essential if the NCS technique is to be routinely employed to investigate the momentum distribution of such tightly bound systems. Zirconium hydride was chosen for this investigation because (i) it is a strongly bound system, (ii) the incoherent

 © 1996 The American Physical Society

neutron cross section of hydrogen is large at the very high momentum transfers used, (iii) its high Debye temperature ensures that the hydrogen is effectively in the ground state at room temperature, (iv) the harmonic approximation is valid and permits an exact calculation of $S_{\mathrm{IA}}(\mathbf{q},\omega)$ from a measurement of the vibrational density of states (DOS), and (v) the hydrogen and zirconium scattering are well separated by the kinematic mass separation of the NCS technique.

II. THEORETICAL BACKGROUND

A. Scattering within the impulse approximation

The double-differential scattering cross section for scattering from a system of N identical atoms at zero temperature is given by[24]

$$\frac{d^2\sigma}{d\Omega\ dE_1}=Nb^2\frac{|\mathbf{k}_i|}{|\mathbf{k}_f|}S(\mathbf{q},\omega), \tag{1}$$

where b is the scattering length, E_1 the energy of the scattered neutron, $\mathbf{k}_i$ and $\mathbf{k}_f$ are the initial and final neutron wave vectors, respectively, $\mathbf{q}$ is the neutron wave-vector transfer ($\mathbf{q}=\mathbf{k_i}-\mathbf{k_f}$), and $\hbar\omega$ is the energy lost by the neutron in the scattering process. The dynamic structure factor $S(\mathbf{q},\omega)$ can be written as

$$S(\mathbf{q},\omega)=\frac{1}{N}\sum_i g_i\left|\sum_n \langle i|\exp(-i\mathbf{q}\cdot\mathbf{r}_n)|f\rangle\right|^2\delta(\omega+E_i-E_f), \tag{2}$$

where $|i\rangle$ and $|f\rangle$ are the initial and final quantum states, $\mathbf{r}_n$ is the position coordinate of atom n, g_i is the Boltzmann factor for occupation of quantum state $|i\rangle$, and Σ_i performs a thermal average. The IA is reached in the limit of large wave-vector transfers where coherent processes are assumed minimal. Then incident neutrons scatter from individual nuclei independently and therefore respond only to a single-particle momentum distribution $n(\mathbf{p})$. The dynamical structure factor can then be written as

$$S_{\mathrm{IA}}(\mathbf{q},\omega)=\int_{-\infty}^{+\infty}n(p)\,\delta\left(\omega-\frac{(\mathbf{p}+\mathbf{q})^2}{2M}+\frac{p^2}{2M}\right)d\mathbf{p}, \tag{3}$$

where $S_{\mathrm{IA}}(\mathbf{q},\omega)$ is the dynamic scattering function in the IA, M is the atomic mass, and where $n(\mathbf{p})$ satisfies the normalization condition

$$\int_{-\infty}^{+\infty}n(\mathbf{p})d^3\mathbf{p}=1 \tag{4}$$

and the δ function restricts the integration to those states that are accessible with energy and momentum conservation. The average recoil energy transferred to the scattering particle is given by

$$\hbar\omega_R=\frac{\hbar^2q^2}{2M}. \tag{5}$$

Choosing $\mathbf{q}$ along the z axis of a Cartesian coordinate system gives

$$S_{\mathrm{IA}}(\mathbf{q},\omega)=\frac{M}{q}J(y), \tag{6}$$

where

$$y=\frac{M}{q}\left(\omega-\frac{q^2}{2M}\right) \tag{7}$$

and

$$J(y)=\int_{-\infty}^{\infty}n(p_x,p_y,y)dp_x\ dp_y. \tag{8}$$

The quantity $J(y)$ is often termed the "neutron Compton profile" (NCP), the one-dimensional projection of $n(\mathbf{p})$ along the direction of the scattering vector. The properties of $S(\mathbf{q},\omega)$ which follow from Eqs. (6)–(8) are known as y scaling and the degree to which the data obey this scaling law is a measure of the validity of the IA. For an isotropic momentum distribution it can be shown that

$$qS_{\mathrm{IA}}(\mathbf{q},\omega)=2\pi M\int_{|y|}^{\infty}pn(\mathbf{p})d\mathbf{p} \tag{9}$$

and the mean kinetic energy of the target particle, $\langle E_k\rangle$, may be determined from $J(y)$ from the second moment of the NCP,

$$\langle E_K\rangle=\frac{3}{2M}\int y^2J(y)dy. \tag{10}$$

B. The harmonic approximation

In the harmonic approximation, the atomic momentum distribution is identical to that of a free gas, except that the temperature is replaced by an effective temperature given by $\hbar^2\sigma^2=MT^*$ and Eq. (8) becomes

$$J(y)=\frac{1}{\sqrt{2\pi MT^*}}\exp\left(\frac{-y^2}{2MT^*}\right), \tag{11}$$

where T^* is the effective temperature defined by[4]

$$T^*=\frac{1}{2}\int\omega Z(\omega)\coth\left(\frac{\omega}{T}\right)d\omega \tag{12}$$

and $Z(\omega)$ is the phonon density of states. We define the variance of the momentum distribution along q as $\sigma=(MT^*)^{0.5}$. In this paper, energies and temperatures are measured in meV, momenta in Å^{-1} and masses in amu unless stated otherwise. In this system of units, $\hbar=2.044\,58$ Å meV$^{1/2}$ amu$^{1/2}$.

C. The Stringari formulation

The Stringari formulation[10] is obtained from the IA by replacing the $p^2/2M$ term with the mean kinetic energy $\langle E_k\rangle$ and the modified dynamical structure factor $S_s(\mathbf{q},\omega)$ is given by

$$S_s(q,\omega)=\int_{-\infty}^{\infty}n(p)\,\delta\left(\omega-\left(\frac{\mathbf{p}+\mathbf{q}}{2M}\right)^2+\langle E_k\rangle\right)d\mathbf{p}. \tag{13}$$

For an isotropic momentum distribution it can be shown that

$$qS_s(\mathbf{q},\omega)=2\pi M\int_{|y_1|}^{\infty} pn(\mathbf{p})d\mathbf{p}, \tag{14}$$

where

$$y_1=\sqrt{2M(\omega+\langle E_K\rangle)}-q \tag{15}$$

is the scaling variable, which should be compared with the IA scaling variable y given in Eq. (7). This predicts a negative shift of magnitude $\langle E_k\rangle$ in the peak energy of $S_s(\mathbf{q},\omega)$ from the IA value of $\hbar^2q^2/2M$.

D. Sears expansion

To account for deviations from the IA Sears[8] proposed a series expansion of $J(y)$ which contained symmetric and antisymmetric terms,

$$J_0(y)=J_{\mathrm{IA}}(y)-A_3\left[\frac{d^3J_{\mathrm{IA}}(y)}{dy^3}\right]+A_4\left[\frac{d^4J_{\mathrm{IA}}(y)}{dy^4}\right]-\cdots \tag{16}$$

where $J_0(y)$ is the observed NCP without instrument resolution and $J_{\mathrm{IA}}(y)$ is the NCS derived in the IA. The coefficients of the first symmetric and antisymmetric terms in the expansion are given by

$$A_3=\frac{M\langle\nabla^2V\rangle}{36\hbar^2q} \quad\text{and}\quad A_4=\frac{M^2\langle F^2\rangle}{72\hbar^4q^2}, \tag{17}$$

where V is the interatomic potential and $\langle F^2\rangle$ is the mean-squared force on the target atom during the scattering. The terms are corrections to the IA arising from FSE's and predict the magnitude and $\mathbf{q}$ dependence of deviations from the IA.

III. EXPERIMENTAL PROCEDURE

The measurements reported here were performed using the eVS at the ISIS facility, which is situated at the Rutherford Appleton Laboratory. The eVS is an inverse-geometry filtered-beam spectrometer which uses a foil with a strong cross section for neutron absorption to define the scattered neutron energy. A pulsed white beam of neutrons with energies in the range 1–100 eV is incident on the sample, and the time-of-flight (TOF) spectrum of the scattered beam is measured by an array of fixed detectors. A resonant foil difference technique is used to yield a set of TOF spectra for those neutrons scattered into a fixed energy and through fixed angles. A full description of the eVS can be found in the literature.[25]

At the time of the experiment reported here, the spectrometer had six banks of 10-atm ^{3}He neutron detectors arranged in pairs symmetrically about the incident beam and covering angles in the ranges 36°–54°, 57°–77°, and 125°–137°, respectively. The detectors were arranged with their axes vertical and centered at the beam height. Forty detectors were arranged at forward-scattering angles ($\theta<90°$) and a further ten at backward-scattering angles.[26] For scattering from hydrogenous systems the dynamics of the interaction restricts the scattering to scattering angles $\theta<90°$ and only data from detectors at forward scattering angles were useful in this investigation. Thirty of these were at angles suitable for hydrogen scattering and for convenience these are represented in this work as three banks—bank A (covering the angular range 36°–44°), bank B (46°–54°), and bank C (57°–66°). In Fig. 1 we show the TOF scans in $(\mathbf{q},\omega)$ space which were available with banks A, B, and C using a gold analyzer. The shaded region is bounded by the full width at half maximum (FWHM) of the response from a hydrogen atom in ZrH_2 (having a momentum distribution with a FWHM of 9 Å^{-1}). It should be noted that the energy and momentum transfers available on resonance filter spectrometers are much greater than those attainable on any other neutron instrument and it can be seen from Fig. 1 that on eVS, for H scattering at the recoil peak position, $2.5<\omega<23$ eV and $35<q<105$ Å^{-1}. At such high momentum and energy transfers, corrections to the IA are expected to be small, but as we shall show they are not negligible. The incident and transmitted beam intensities were monitored using glass scintillation detectors placed before and after the sample.

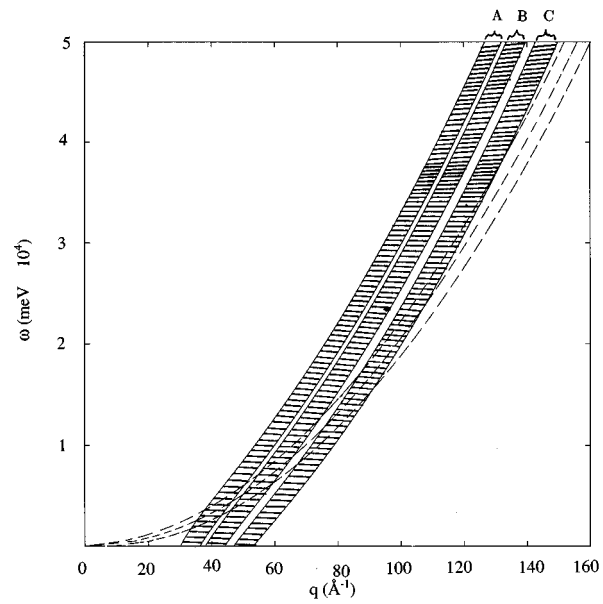

FIG. 1. Detector scans on eVS through $(\mathbf{q},\omega)$ space. In this work the eVS had 40 detectors at forward-scattering angles. 30 of these were at angles useful for hydrogen scattering, which are considered for convenience grouped together in three banks of detectors 36°–44° (bank A), 46°–54° (bank B), and 57°–66° (bank C). Each detector scan for each bank lies in the shaded region A, B, or C marked on the figure. The dashed curves represent the peak position and FWHM of the response of a hydrogen atom in ZrH_2 which has a momentum distribution with a FWHM of 9 Å^{-1}.

The sample was placed in a square aluminum can mounted on the end of an aluminum stick and positioned perpendicular to the beam. Detector saturation was avoided by limiting the total scattering to 5% of the incident beam. The beam tubes and the sample chamber were evacuated to minimize air scattering. The samples were manufactured at the Department of Physics of the University of Warwick from powdered samples of zirconium obtained from Goodfellow Metals (Cambridge). The grain size and purity of the powdered sample of zirconium were 150 μm and 99.50%, respectively. The percentage of hydrogen absorbed was carefully monitored during hydriding and the resulting composition was determined to be ZrH_x, $x=1.96\pm0.04$.

Gold foils were mounted on a cylindrical aluminum support which surrounded the sample chamber and placed in the scattered beam. The foils are automatically cycled in and out of the scattered beam every 5 min by means of pneumatic pistons. The constant cycling of the resonant foil minimizes systematic errors which result from changes in the relative efficiency of the detectors to neutrons of different energies. Two types of measurement were made: one with the resonant foils in and one with the resonant foils out of the scattered beam. The TOF spectra corresponding to the ''foil in'' and ''foil out'' measurements were collected in separate areas of the instrument computer memory. The gold foil has a strong absorption cross section of Lorentzian shape, centered at 4917.6 meV and with a half width at half maximum (HWHM) of 143.1 meV. By taking the difference between spectra collected with ''foil in'' and ''foil out'' the count rate for neutrons scattered with energy 4917.6 ± 143.1 meV was determined.

The isotropic nature of the sample means that data from groups of detectors may be added together to increase the statistical accuracy. Summing data over banks of detectors with similar scattering angles results in a NCP of high statistical accuracy which covers a range of momentum transfer. Measurements were performed at both 20 and 290 K although the proton is effectively restricted to the ground state at both these temperatures. Furthermore, ZrH_2 exists in the ϵ phase at both these temperatures. This was confirmed by analysis of diffraction data which are recorded simultaneously with NCS data but in a different region of TOF (NCS 100–700 μs; diffraction 1000–20 000 μs). Diffraction peaks corresponding to d spacings greater than 1 Å were identified and the (002) peak due solely to the ϵ phase was observed.

Shown in Fig. 2 are typical TOF ''foil out'' and ''foil in'' spectra (each normalized to the incident beam) for scattering from ZrH_2 collected at a scattering angle of 36°. Shown in Fig. 3 is the difference of these two measurements for a series of detectors in one of the low-angle banks. The difference spectrum yields those neutrons absorbed by the analyzer foil. The broad peak is the hydrogen scattering, while the narrow peak is the combined scattering from the zirconium and the aluminum sample holder. Note how the separation of the two peaks and the width of the hydrogen peak become larger at higher scattering angles.

IV. ANALYSIS

The data analysis procedures for the eVS are described fully elsewhere[25] and only a summary is given here. The ''foil in'' and ''foil out'' TOF spectra obtained by each detector were suitably normalized and then subtracted. The aluminum can scattering was determined by an empty can measurement and then subtracted from the data. The zirconium scattering was removed by fitting an appropriate Voigt function (convolution of a Gaussian and a Lorentzian) to each TOF data set, the parameters of the Voigt function being determined by the instrument resolution and the Gaussian width of the zirconium recoil scattering. The TOF spectrum from each detector was then transformed into y space using either the IA or the Stringari scaling expressions, Eqs. (7) and (15), respectively.

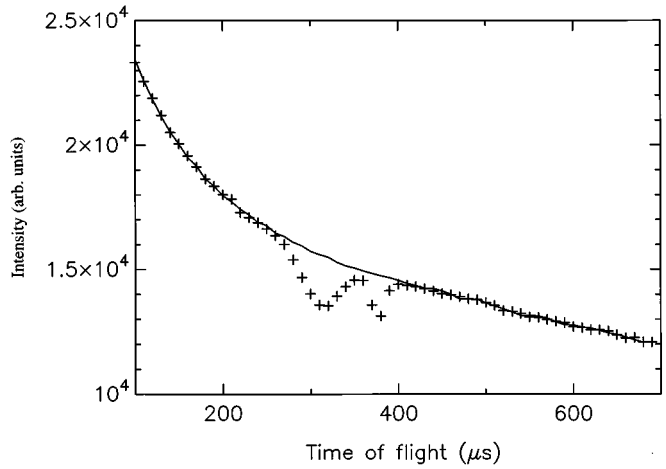

FIG. 2. Foil in (crosses) and foil out (line) time-of-flight measurements of ZrH_2 on eVS. The scattering angle for these measurements was 36°.

Analytical expressions for the components of the instrument resolution function in y space[27] were used to calculate the resolution components and the results for detector bank C are given in Fig. 4. The contributions are independent and originate from the distribution of the initial and final flight paths (σ_0 and σ_1, respectively), and scattering angles and incident energy values allowed by the instrument geometry, σ_θ, and the analyzer foil, σ_E. In all cases the dominant contribution is σ_E although the angular term σ_θ is significant for scattering from hydrogenous systems and was determined for all detectors from the line shape of powder diffraction peaks. The intrinsic energy width of the gold resonance was previously determined for each detector, both analytically and experimentally by measurements of recoil scattering from heavy systems such as lead and tin, and is well described by a Lorentzian function. All other resolution components are well described by Gaussian functions. The resultant resolution function is therefore a Voigt function.

The mean atomic kinetic energy was determined by fitting each individual momentum-space difference spectrum with a Gaussian, of the form given in Eq. (18) below, convoluted with the appropriate resolution function

$$J(y) = \left(\frac{1}{\sqrt{2\pi\sigma_y^2}} \right) \exp\left(\frac{-(y-y_m)^2}{2\sigma_y^2} \right). \tag{18}$$

Two fitting parameters were used; the profile centroid y_m and standard deviation σ_y. The mean atomic kinetic energy was determined from the value of σ_y whereas deviations of y_m from zero were used to test the validity of the IA and to investigate the significance of FSE's. Values of σ_y were averaged to give a single value for each detector bank. These values were further averaged and used to determine the Debye-Waller factor used to calculate the density of states.

V. DENSITY OF STATES

As mentioned in Sec. II, exact simulations of $J(y)$ can be performed by calculating the scattering function $S(\mathbf{q},\omega)$ for an isotropic harmonic solid using the density of states. Although ϵ-phase ZrH_2 has been studied in great detail, we

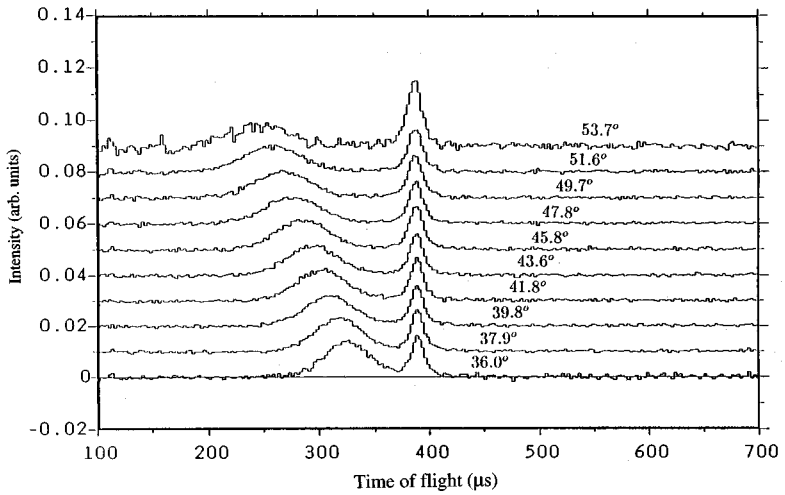

FIG. 3. A series of time-of-flight difference measurements of ZrH_2 measured on one of the low-angle detector banks on eVS. The broad peak is scattering from hydrogen, while the narrow peak is scattering from aluminum (in the sample holder) and zirconium. Note how the separation of the two peaks and the width of the hydrogen peak both become larger at high scattering angles.

know of no previous attempt to derive the phonon density of states explicitly. The theoretical results required for our analysis are detailed below.

An exact calculation of both the single-particle $S(\mathbf{q},\omega)$ and $n(\mathbf{p})$ from the density of states is possible within the harmonic approximation.[28] For an isotropic system, the single-particle incoherent scattering in the harmonic approximation is given by[24]

$$S_H(\mathbf{q},\omega)=\left[\frac{1}{2\pi\hbar}\right]\int_{-\infty}^{\infty}dt\ \exp(-i\omega t)\exp\left(\frac{\hbar^2q^2}{2M}\right)\times[\gamma(t)-\gamma(0)], \tag{19}$$

where

$$\gamma(t)=\int_{-\infty}^{\infty}d\omega[Z(\omega)/\omega]n(\omega)\exp(-i\omega t). \tag{20}$$

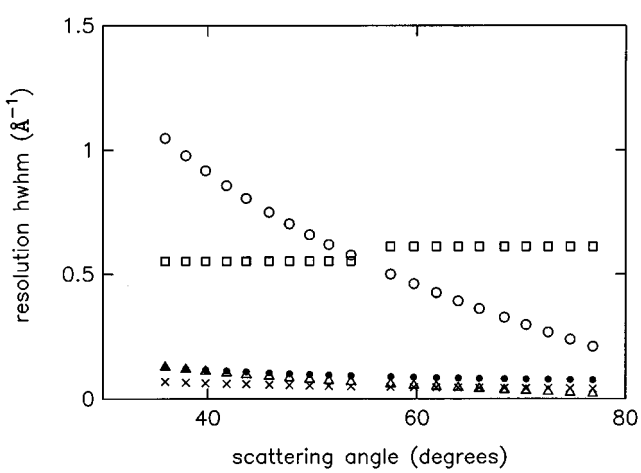

FIG. 4. Calculated resolution components of eVS for hydrogen scattering over all forward-scattering detectors (banks A, B, and C) obtained from separate measurements on heavy elements. The different resolution components arise from the analyzer foil, σ_E (open circles), the scattering geometry, σ_θ (squares), the uncertainty of the measurement in time of flight (crosses), and the distribution of the initial and final flight paths, σ_0 (open triangles) and σ_1 (solid circles), respectively.

The one-phonon contribution to $S_H(\mathbf{q},\omega)$ can be obtained from (19) by expanding the exponential term $\exp(-i\omega t)$ and is given by

$$S_{H,+1}(\mathbf{q},\omega)=\frac{1}{2M}\,q^2\exp[-2W(\mathbf{q})]\left[\frac{Z(\omega)}{\omega}\right][n(\omega)+1], \tag{21}$$

where the subscript $+1$ refers to phonon creation, $Z(\omega)$ is the normalized phonon density of states, $W(q)$ is the Debye-Waller factor, and $n(\omega)$ is the Bose-Einstein occupation factor $n(\omega)=[\exp(\hbar\omega/k_BT)]^{-1}$ where k_B is Boltzmann's constant. At low $\mathbf{q}$, $S(\mathbf{q},\omega)$ is dominated by one-phonon scattering and the density of states can be derived directly from Eq. (21). Following the method used by Andreani[29] for a polycrystalline sample the density of states $g(\omega)$ is given by

$$g(\omega)=\lim_{q\to 0}\ g'(\mathbf{q},\omega)=\frac{S_{H,+1}(\mathbf{q},\omega)}{q^2}\,2M\omega\,\frac{\exp 2W(\mathbf{q})}{[n(\omega)+1]}. \tag{22}$$

For a cubic Bravais lattice $W(\mathbf{q})=q^2/2\sigma^2$ and if $W(\mathbf{q})$ is known $g(\omega)$ can be calculated from a measurement of $S(\mathbf{q},\omega)$. $W(\mathbf{q})$ was determined using a value of $\sigma=4.18$ Å^{-1} and $S(\mathbf{q},\omega)$ was measured using the MARI spectrometer at ISIS. A complete account of the experimental procedure and a discussion of the MARI results will be given elsewhere[30] and only a brief description is included here.

MARI is a direct-geometry chopper spectrometer operating in TOF.[31] It has a very large array of neutron detectors distributed over a wide range of angles which allow $S(\mathbf{q},\omega)$ to be measured over a range of values in $(\mathbf{q},\omega)$ space with a resolution that is typically 1–2 % of the incident energy. The energy of the incident pulses of neutrons is determined by the rotational speed of the Fermi chopper, phased to the neutron burst time. This energy sets the maximum energy of the region of $(\mathbf{q},\omega)$ space to be observed. The maximum momentum transfer available on MARI for scattering from hydrogenous samples is about 20 Å^{-1}, compared to about 100 Å^{-1} for eVS.

Multiple-scattering effects were investigated by performing three experiments, all at 20 K with two different sample geometries and two different incident energies (220 and 450

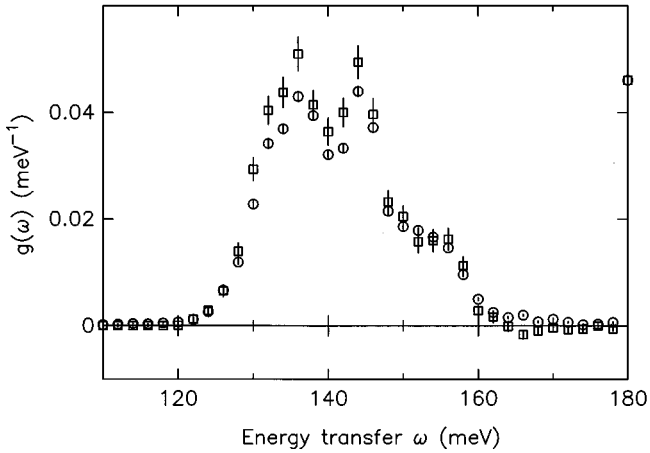

FIG. 5. The vibrational density of states of H in ZrH_2 obtained from the measurement of $S(\mathbf{q},\omega)$ with a slab sample geometry (circles) and that obtained with a cylindrical sample geometry (boxes). Both runs were made with an incident energy of 220 meV. The similarity of the derived density of states for these two different geometries indicates that multiple-scattering effects are small.

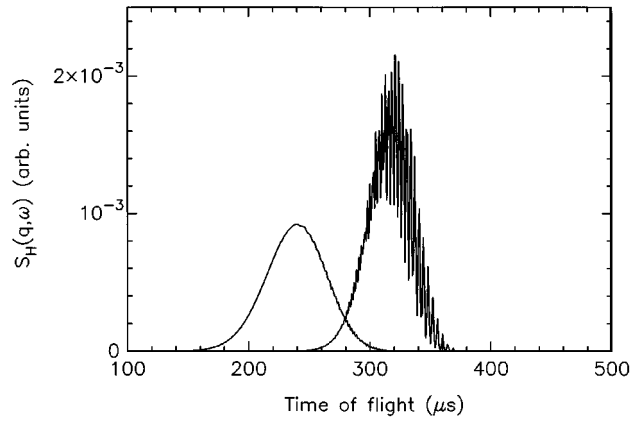

FIG. 6. Simulations of eVS time-of-flight spectra for scattering from hydrogen in ZrH_2. The simulations are based on the measurement of the vibrational density of states (incident energy 220 meV) and are an exact numerical simulation in the harmonic incoherent approximation. The simulations shown are for detectors at scattering angles of 36.0° and 53.7°. The individual multiphonon excitations are visible in the peak centered at about 310 μs. At the higher momentum transfers reached at 53.7°, the individual excitations merge together. The data shown are not resolution convoluted.

meV). To minimize systematic errors in the derived density of states it is important to ensure that multiple scattering does not adversely affect the data at low $\mathbf{q}$. In each measurement the scattered intensity was of the order of 5%, low enough to ensure that multiple scattering was not significant. If significant, the different combinations of sample geometry and incident energy would yield significantly different results for the derived vibrational density of states. This was not the case. There is the advantage that the exact form of the vibrational density of states does not affect the form of the NCP at large $\mathbf{q}$. The width of the NCP should only depend on the mean kinetic energy of the system, and therefore on the density of states via the effective temperature, Eq. (12).

The MARI data were in the form of a rectangular grid of values of $S(\mathbf{q},\omega)$. A series of constant-ω cuts were made at intervals of between 0.5 and 1.0 meV. Each of the data sets so obtained was converted to a value defined here as $g'(\omega,\mathbf{q})$. By extrapolating $g'(\omega,\mathbf{q})$ to $\mathbf{q}=0$ for each value of ω, and normalizing to unity, $g(\omega)$ was obtained. A weighted least-squares straight-line fit was used to perform the extrapolation. Once the extrapolated values were obtained in the region 100–200 meV, they were normalized to unity. Figure 5 shows the derived density of states, corresponding to MARI data obtained with an incident energy of 220 meV and slab and cylindrical sample geometries (circles and boxes respectively). The density of states obtained with the higher incident energy was of poorer resolution and is not shown.

VI. EXPERIMENTAL RESULTS AND SIMULATIONS

Simulations of the measured neutron Compton profiles of ZrH_2 in TOF were performed using the density of states shown in Fig. 5 as boxes (see Ref. 9). The slab geometry measurement had the best counting statistics and this density of states was used to simulate eVS data. Data were simulated using the calibration parameters appropriate to each of the 30 detectors used in the measurements. Three profiles were created by adding simulated data corresponding to detectors in each of the three detector banks A, B, and C. The simulated TOF spectra were convolved with the resolution function for each detector, converted to momentum space, and then analyzed in the same way as the "real" eVS data. A value of 143.1 meV was used for the full width at half maximum of the Lorentzian resolution contribution from the analyzer foil. Simulations in TOF for scattering angles of 35.96° and 53.68° are shown in Fig. 6 before convolution with the instrument resolution. The individual multiphonon excitations are visible. Higher momentum transfers are reached at the larger scattering angle of 53.68° and the individual excitations merge together. After convolution with the resolution function there was no sign of the individual excitations for even the lowest scattering angle (lowest momentum transfer).

The results of the simulations of the measured NCP for detector banks A, B, and C are compared to eVS measurements in Figs. 7(a), 7(b), and 7(c). The y scaling procedure [Eq. (7)] was used to convert the TOF data to momentum space. The profiles measured by each of the ten detectors in each bank have been summed and normalized to unity. The momentum transfer ranges sampled by banks A, B, and C were 35.3–46.6 Å^{-1}, 50.0–65.8 Å^{-1}, and 75.7 and 108.6 Å^{-1}, respectively. The simulations based on the measured vibrational density of states are shown as solid lines. Shown also is the sum of four measurements of hydrogen in ZrH_2. Three of these measurements were the results of a previously unpublished experiment on a commercially supplied sample of ZrH_2 (Ref. 32) and the other used the sample prepared for the density of states measurement. Good experimental consistency is observed. The difference between the simulation and the IA result calculated directly from the density of states is shown as the lower solid line. In both the simulation and the eVS data an asymmetry is observed. As expected, at finite values of $\mathbf{q}$, the peak position is shifted to negative values of momentum space. Both the asymmetry and peak

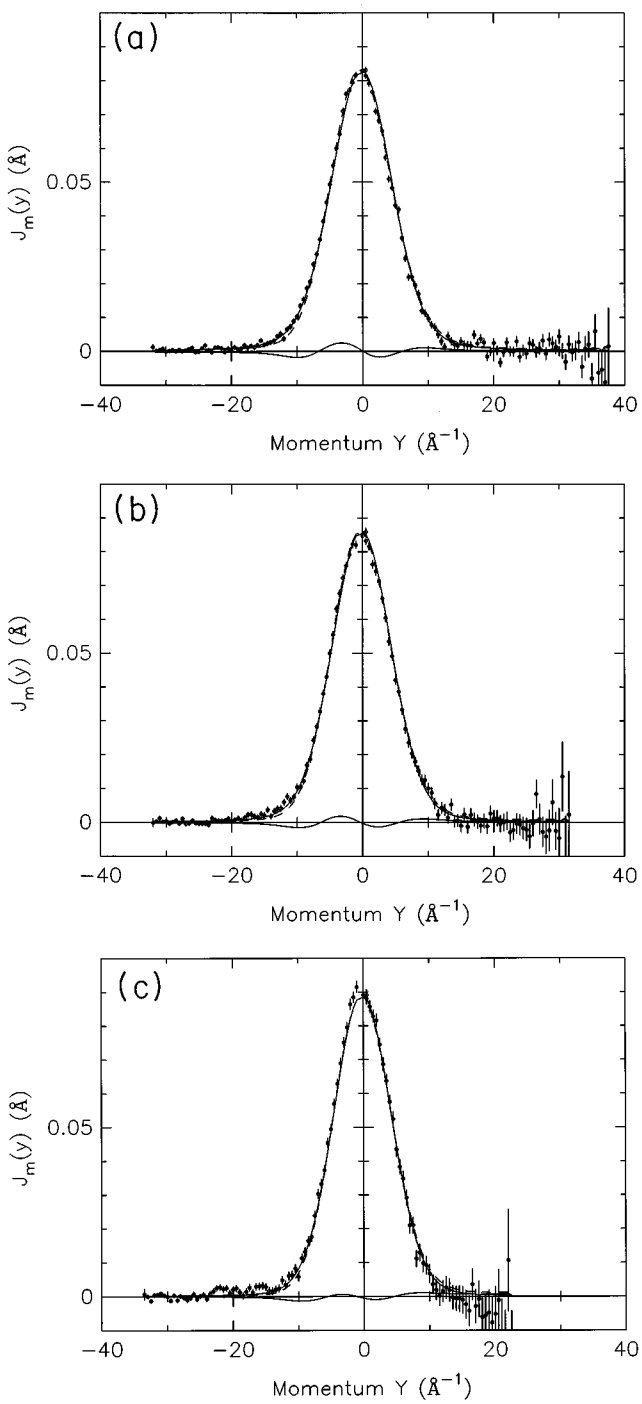

FIG. 7. Comparison of measurements of $J_m(y)$ made at average momentum transfers of (a) 40.8 Å^{-1} (bank A), (b) 57.6 Å^{-1} (bank B), and (c) 91.2 Å^{-1} (bank C), respectively, on eVS (+) compared to exact simulations of the data based on the density of states of the hydrogen vibrations measured with the MARI spectrometer (solid line). The form of $J_m(y)$ reached in the impulse approximation is also shown (dashed line). The difference between this and the simulation is shown as the lower solid line. The conventional y scaling was used to transform from time of flight to momentum space.

shift are attributed to the presence of FSE's. To demonstrate the approach to the IA as **q** increases, the measured peak position of each profile was determined. The peak position was not affected by the resolution function as this is symmetric. Figure 8(a) shows the peak shifts in the y scaled eVS

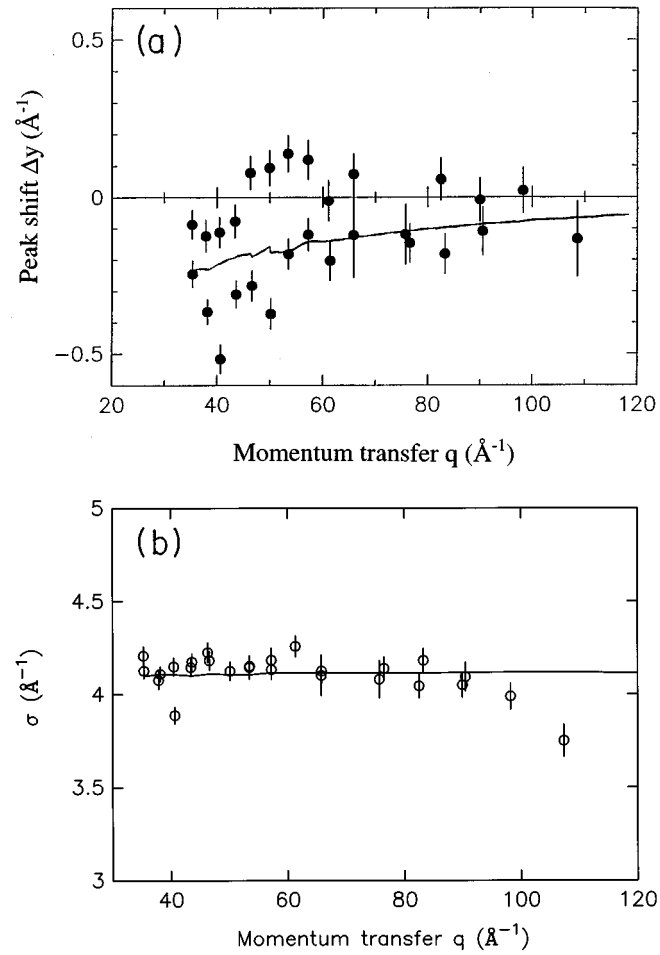

FIG. 8. (a) The positions of the recoil peaks in y space are shown for the eVS measurements (circles) as a function of the momentum transfer of the measurements. Also shown (solid line) is the same for the numerical simulation. (b) The σ values determined from the eVS measurements (circles). They are plotted against the σ values determined from the numerical simulation from the vibrational density of states (solid line).

data and the derived peak shifts of the simulated data plotted as a function of y. The peak positions as a function of y are also shown for the simulated data. The peak shifts become progressively smaller as the momentum transfer is increased, in accordance with the limiting behavior of the IA. This observation is reinforced by returning to Fig. 7 where the difference between the IA and simulation is reduced as the momentum transfer is increased from banks A to C.

Figure 9 corresponds to Fig. 7 except that the Stringari y_1 scaling variable has been used to convert from TOF to momentum space. The difference is clear. The measured neutron Compton profiles are distinctly more asymmetric than the y-transformed data.

The mean atomic kinetic energy $\langle E_k \rangle$ can be deduced by fitting with a model having the form of Eq. (18) and using $\langle E_k \rangle = 3\sigma_y{}^2/2M$. Figure 8(b) shows the fitted values of σ_y as a function of y for the eVS data (circles) and the results obtained from the simulation (solid line). The dependence of σ_y on the form of the density of states was tested by repeating the simulations for ZrH_2 using a slightly different density of states and with σ_y values of 4.14 and 4.17 Å^{-1}, respec-

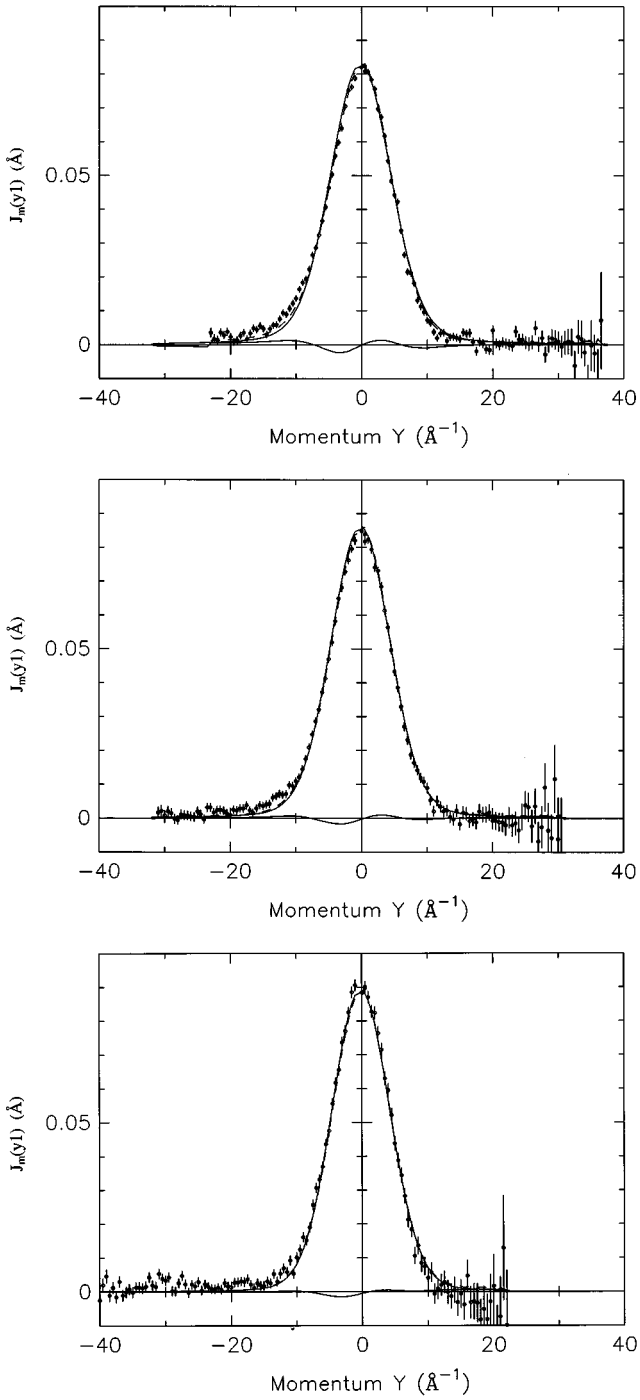

FIG. 9. This is the analogous diagram to Fig. 7 except in this case y_1 scaling was used to convert from time of flight to momentum space.

tively. The values extracted from the two simulated profiles were 4.123±0.002 and 4.141±0.002 Å^{-1}. The difference in these values (1%) indicates the sensitivity of the derived value to the mean value of the density of states used in the simulations. However, the form of the density of states has little bearing on the simulations. After applying the Sears symmetrization procedure outlined in Sec. II the symmetrized y-transformed simulation gave a value of σ=4.154 Å^{-1}, which agrees well with the value of 4.14 Å^{-1} derived from the density of states.

The sensitivity of σ_y to the half width at half maximum of the Lorentzian contribution to the resolution function was determined by repeating the y-transformed simulations using values of ΔE_R=126 and 143.1 meV. For the hydrogen simulations, the two analyses gave values of 4.146±0.002 and 4.123±0.002 Å^{-1}, respectively, a difference of about 0.75% or just under 1.44% in the mean kinetic energy. This is comparable to the statistical accuracy of the measurement, and so is not of great significance. This justified the value of ΔE_R=140 meV used consistently in the analysis.

Table I gives σ_y determined from the density of states directly, through Eq. (12) (the harmonic approximation), from the symmetrized and unsymmetrized neutron Compton profiles simulated from the density of states, and from the symmetrized and unsymmetrized measured neutron Compton profiles. Values obtained using both y and y_1 scaling are given for the simulated and measured data. The Stringari IA (SIA) transformation generally leads to an overestimation of the mean kinetic energy compared with that calculated directly from the density of states. This is consistent with the asymmetry observed in Fig. 9. FSE's also result in a profile asymmetry which can be corrected by symmetrization of $J(y)$. This procedure removes FSE's of order $\mathbf{q}^{-1}$ and is applicable to these data because FSE's are expected to be small at the high momentum transfers used. The values for σ_y thus obtained are typically 1% larger than the unsymmetrized values. For the symmetrized y-transformed simulations, the results agree within error with the value of 4.14 Å^{-1} calculated directly from the density of states. The values measured at the low and intermediate momentum transfer (banks A and B) are also in agreement. The small underestimation at higher $\mathbf{q}$ (bank C) may be attributed to a systematic error resulting from instability in the measurement at very short times of flight.

VII. CONCLUSIONS

We have used neutron Compton scattering from ZrH_2 to test the validity of the IA and SIA in scattering from hydrogenous systems. We find that using the Stringari scaling variable y_1 introduces a significant asymmetry in $J(y_1)$ and the extracted kinetic energy is significantly larger (2%) than the value determined from the density of states directly. Our data suggest that y scaling is more appropriate for tightly bound hydrogenous systems such as ZrH_2. FSE's are manifested in our data by shifts in the peak position to negative y values and as a profile asymmetry. Both effects are reduced at high $\mathbf{q}$ as the IA is approached. For $\mathbf{q}$>40 Å^{-1} symmetrization removes FSE's to the accuracy of these data. At lower $\mathbf{q}$ we believe effects of order $\mathbf{q}^{-2}$ remain. We conclude that electron-volt spectroscopy with the energy and momentum transfers currently available can be used to obtain accurate results on tightly bound hydrogenous systems.

It is perhaps not surprising that the y_1 scaling is inaccurate in zirconium hydride. It has been shown[9] that y_1 scaling is a preferable description to y scaling in an infinite square-well potential. In this case, the energy of the particle is entirely kinetic and the replacement of the initial energy by the kinetic energy E_k is exact. Stringari also showed that y_1 scaling provides an accurate description of deviations from the

TABLE I. The variance σ_y of $J(y)$ (unsymmetrized) of hydrogen in ZrH_2 determined from exact numerical calculations described in the text ($\sigma_{\rm sim}$) and measurements made on the eVS spectrometer (σ_m) for three ranges of momentum transfer. The results of the symmetrized calculations and measurements are also given ($\sigma_{S\rm sim}, \sigma_{Sm}$). Values are compared to $\sigma_{\rm DOS}$ determined from the density of states directly through Eq. (12). The numbers in parentheses are the errors.

Profile widths (Å^{-1})	Bank A $q_{\rm mean}$=40.8 Å^{-1}		Bank B $q_{\rm mean}$=57.6 Å^{-1}		Bank C $q_{\rm mean}$=91.2 Å^{-1}	
Scaling variable	y[a]	y_1[a]	y	y_1	y	y_1
$\sigma_{\rm sim}$	4.106(0.007)	4.149(0.008)	4.112(0.005)	4.159(0.005)	4.117(0.005)	4.165(0.005)
$\sigma_{S\rm sim}$	4.151(0.005)	4.149(0.006)	4.160(0.004)	4.169(0.004)	4.169(0.003)	4.192(0.003)
σ_m	4.12(0.01)	4.17(0.02)	4.16(0.02)	4.21(0.02)	4.03(0.06)	4.06(0.03)
σ_{Sm}	4.15(0.01)	4.20(0.01)	4.17(0.01)	4.21(0.01)	4.03(0.02)	4.09(0.02)
$\sigma_{\rm DOS}$	4.14		4.14		4.14	

[a] y and y_1 scaling variables are described in the text.

impulse approximation in liquid helium. The interatomic potential in liquid helium is similar to the square-well potential in that it is weak, except at short interatomic distances. The effect of a longer-range interatomic potential, such as the harmonic potential in zirconium hydride, is to reduce shifts in the peak position of $J(y)$, compared with the predictions of y_1 scaling. Thus the type of scaling which is observed will depend on the nature of the interatomic potential.

ACKNOWLEDGMENTS

This research was supported in part by the U.K. Science and Engineering Research Council under Contract Nos. GR/H97161 and GR/H03919. We are grateful to the SERC for the provision of beamtime and research support at the ISIS neutron factility. The ZrH_2 sample was manufactured at the University of Warwick with the assistance of Dr. G. Styles.

*Present address: Rutherford Appleton Laboratory, Chilton, Didcot, Oxfordshire OX11 0QX, UK.

[1] P. C. Hohenberg and P. M. Platzmann, Phys. Rev. **152**, 198 (1966).
[2] *Compton Scattering*, edited by B. Williams (McGraw-Hill, New York, 1977).
[3] V. F. Sears, Phys. Rev. A **5**, 452 (1971); **7**, 340 (1973); J. J. Weinstein and J. W. Negele, Phys. Rev. Lett. **49**, 1016 (1982).
[4] J. Mayers, C. Andreani, and G. Baciocco, Phys. Rev. B **39**, 2022 (1989).
[5] C. Carraro and S. E. Koonin, Phys. Rev. Lett. **65**, 2792 (1990).
[6] A. Belic and V. R. Pandharipande, Phys. Rev. B. **45**, 839 (1992).
[7] R. N. Silver, Phys. Rev. B **37**, 3794 (1988); **38**, 2283 (1988); **39**, 4022 (1989).
[8] V. F. Sears, Phys. Rev. B **30**, 44 (1984).
[9] J. Mayers, Phys. Rev. B **41**, 41 (1990).
[10] S. Stringari, Phys. Rev. B **35**, 2038 (1987).
[11] R. O. Hilleke, P. Chaddah, R. O. Simmons, D. L. Price, and S. K. Sinha, Phys. Rev. Lett. **52**, 847 (1984).
[12] R. C. Bladsdell, D. M. Ceperley, and R. O. Simmons, Z. Naturforsch. Teil A **48**, 433 (1993).
[13] H. Mook, Phys. Rev. B **37**, 5806 (1988); W. M. Snow, Y. Yang, and P. E. Sokol, Europhys. Lett. **19**, 403 (1992).
[14] K. H. Anderson, W. G. Stirling, A. D. Taylor, S. M. Bennington, Z. A. Bowden, I. Bailey, and H. R. Glyde, Physica B **181**, 865 (1992).
[15] D. A. Peek, I. Fujita, M. C. Schmidt, and R. O. Simmons, Phys. Rev. B **45**, 9680 (1992); M. A. Fradkin, S. X. Zeng, and R. O. Simmons, *ibid.* **49**, 3197 (1994); D. N. Timms, A. C. Evans, J. Mayers, M. Boninsegni, D. M. Ceperley, and R. O. Simmons (unpublished).
[16] D. A. Peek, M. C. Schmidt, I. Fujita, and R. O. Simmons, Phys. Rev. B **45**, 9671 (1992).
[17] P. Postorino, F. Fillaux, J. Mayers, J. Tomkinson, and R. S. Holt, J. Chem. Phys. **94**, 4411 (1991).
[18] J. Noreland (private communication).
[19] A. C. Evans, J. Mayers, D. N. Timms, and M. J. Cooper, Z. Naturforsch. Teil A **48**, 425 (1993); S. Fulton, R. A. Cowley, and A. C. Evans, J. Phys. Condens. Matter **6**, 2977 (1994); A. C. Evans, J. Mayers, and D. N. Timms, *ibid.* **6**, 4197–4212 (1994).
[20] W. E. Langel, D. L. Price, R. O. Simmons, and P. E. Sokol, Phys. Rev. B **38**, 275 (1988); K. W. Herwig, J. C. Gavilano, M. C. Schmidt, and R. O. Simmons, *ibid.* **41**, 96 (1990); J. Mayers, Phys. Rev. Lett. **71**, 1553 (1993).
[21] F. J. Bermejo, F. J. Mompeán, A. Srinivasan, J. Mayers, and A. C. Evans, Phys. Lett. A **189**, 333 (1994).
[22] M. P. Pauli and R. S. Holt, J. Phys. C **21**, 3633 (1988); H. Rauh and N. Watanabe, Phys. Lett. **100A**, 244 (1984).
[23] R. S. Holt, L. M. Needham, and M. P. Pauli, Phys. Lett. **126**, 373 (1987).
[24] S. W. Lovesey, *Theory of Neutron Scattering from Condensed Matter* (Oxford University Press, New York, 1987).
[25] J. Mayers and A. C. Evans (unpublished).
[26] For an example of a typical setup, see A. C. Evans, J. Mayers, and D. N. Timms, J. Phys. Condens. Matter **6**, 4197 (1994).
[27] C. Andreani, G. Baciocco, R. S. Holt, and J. Mayers, Nucl. Instrum. Methods Phys. Res. Sect. A **276**, 297 (1989).
[28] J. M. F. Gunn, C. Andreani, and J. Mayers, J. Phys. C **19**, L835 (1986).
[29] C. Adreani, Mol. Phys. **73**, 737 (1991).
[30] A. C. Evans, D. N. Timms, J. Mayers, and S. M. Bennington (unpublished).
[31] S. M. Bennington and R. S. Eccleston (unpublished).
[32] A. C. Evans (private communication).

J. Phys.: Condens. Matter 6 (1994) 8989–9000. Printed in the UK

Inelastic neutron scattering study of ordered γ-ZrH

A I Kolesnikov†‡, I O Bashkin†, A V Belushkin§‖, E G Ponyatovsky† and M Prager‡

† Institute of Solid State Physics of the Russian Academy of Sciences, 142432 Chernogolovka, Moscow District, Russia

‡ Institut für Festkörperforschung, Forschungszentrum Jülich KFA, D-52425 Jülich, Germany

§ Frank Laboratory of Neutron Physics, Joint Institute for Nuclear Research, 141980, Dubna, Moscow District, Russia

‖ Rutherford Appleton Laboratory, Chilton, Didcot, Oxon OX11 0QX, UK

Received 7 July 1994

Abstract. Lattice dynamics of the ordered γ-ZrH phase was studied by inelastic neutron scattering (INS). It was found that the hydrogen optical peak in the INS spectrum had three maxima at energy transfers of 141.5, 148.7 and 156.3 meV. The peak was accurately described using the Born–von Kármán model. Anharmonicity of hydrogen vibrations was evident in the high-energy range of the spectrum from a strong sharp peak at $E = 269.7$ meV and broader features below the bands of free-multiphonon scattering. These anharmonic phenomena were attributed to the bound multiphonon states (biphonon, triphonon, tetraphonon and their combinations), and the values of the binding energies of biphonons and triphonons were obtained from the experimental data.

1. Introduction

The structure and lattice dynamics of γ-ZrD have been studied recently using neutron diffraction and inelastic neutron scattering (INS) [1]. It was found that γ-ZrD had approximately stoichiometric composition and had a face-centred orthorhombic metal sublattice with axial ratios $b/a \simeq 1.015$ and $c/a \simeq 1.091$. Deuterium atoms occupied the tetrahedral interstices on alternate {110} planes, and the space group was $Cccm$ rather than $P4_2/n$ assumed earlier [2]. Thus, the γ-ZrD structure proved to be similar to that of γ-TiH(D) [3–5].

The γ phase in the Ti–H and Zr–H systems is unique among the hydride phases. The H–H distance along the crystal c-axis is shorter than those in the ab plane by a factor of $\sqrt{2}/1.09 \simeq 1.3$. Therefore, this phase can be considered as a hydride where the H–H interaction is essentially one dimensional.

Previous INS experiments have shown that H(D) vibrations in γ-TiH, γ-TiD [6–8] and γ-ZrD [1] were highly anharmonic. Each spectrum had a peak below the band of free two-phonon scattering, and somewhat broader features were observed below the higher-harmonic multiphonon bands. These anharmonic effects have been discussed in terms of bound multiphonon states, i.e. biphonon, triphonon and tetraphonon excitations, which were proposed for a lattice dynamic description of systems with large anharmonicity (for a review see [9]).

In this work we measured the INS spectrum of $(\alpha+\gamma)$-$ZrH_{0.68}$ which contains just one hydride phase, γ, the rest being α-Zr. The anticipated splitting of the hydrogen optical peak

as well as the anharmonic features at the multiphonon bands are found. Their nature and the isotope effects are discussed.

2. Experimental

To prepare the sample, a Zr ingot of 99.96 at.% purity was heated in a vacuum of $\sim 7 \times 10^{-3}$ Pa to 1070 K and allowed to absorb gaseous hydrogen which was obtained by thermal decomposition of TiH_2. The hydrogen content was determined from the weight gain, $x = H/Zr = 0.68 \pm 0.01$. The hydrogenated sample was aged at ambient temperature for nine years. Six plates of $23 \times 45 \times 0.6\,mm^3$ size were then spark-cut from the $ZrH_{0.68}$ ingot, mechanically polished and etched in $HF+HNO_3$. An x-ray test demonstrated that the $ZrH_{0.68}$ sample thus prepared consisted of two phases, γ and α. The α phase (space group $P6_3/mmc$) has a HCP lattice with a hydrogen content close to zero at helium temperature [2].

INS measurements were carried out at 4.5 K using the time-focused crystal analyser (TFXA) spectrometer [10] at the spallation neutron source, ISIS, Rutherford Appleton Laboratory, UK. The spectrometer provided an excellent resolution, $\Delta\omega/\omega \leqslant 2\%$, in the range of energy transfer 2–500 meV. The data were transformed to $S(Q, \omega)$ against energy transfer (meV) using standard programs. The background from the empty can in the cryostat was measured under the same conditions and subtracted from the experimental data.

To control the phase content of the sample, neutron diffraction was measured at the TFXA spectrometer simultaneously with INS. It also confirmed that the sample consisted of two phases only, γ-ZrH and α-Zr.

3. The INS spectrum

The experimental INS spectrum $S(Q, \omega)$ for the $(\alpha+\gamma)$-$ZrH_{0.68}$ sample is shown in figure 1 (points). Excitations are observed at various different energy transfers: (i) the lower range, 0–30 meV, is usually associated with vibrations of heavy metal atoms in the hydrides; (ii) the medium range, 135–160 meV, is due to hydrogen optical modes in γ-ZrH; and (iii) the range above 250 meV is related to multiphonon processes of neutron scattering on the hydrogen atoms.

3.1. Multiphonon contributions to the one-phonon spectrum

The contribution from multiphonon neutron scattering was calculated in the harmonic isotropic approximation up to four-phonon processes by an iterative technique using multiconvolution of the one-phonon spectrum [6, 11]. Experimental data in the energy range of the lattice and hydrogen optic phonons, 2–160 meV, were accepted at the first iterative step as the one-phonon spectrum of hydrogen vibrations. To take into account only the contribution from hydrogen atoms, the intensity of the spectrum in the range of lattice vibrations was multiplied by a factor of 0.60. This factor appeared for the following reason. Calculation of the γ-ZrH lattice dynamics in section 3.2 showed that the ratio of integrated partial intensities $S(Q, \omega)$ for zirconium and hydrogen atoms is equal to 0.45 in the range of lattice vibrations. The same efficiency was assumed for the contribution of Zr atoms in the α phase. The above factor 0.60 was then obtained from the phase content in the sample, 32% α and 68% γ.

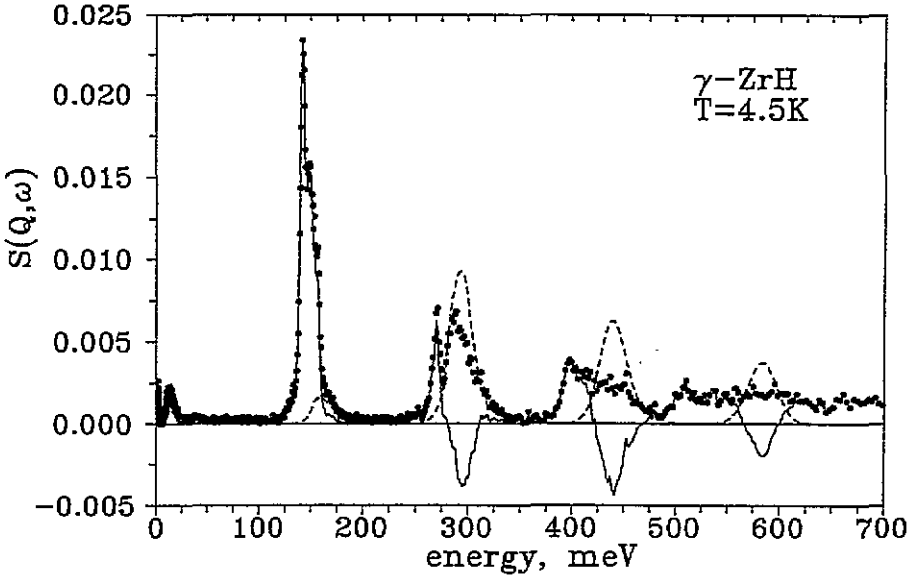

Figure 1. The INS spectrum $S(Q,\omega)$ of the $(\alpha+\gamma)$-$ZrH_{0.68}$ at 4.5 K (points). The calculated multiphonon contribution is shown as a broken curve; the full curve represents the difference between the experimental data and the calculated multiphonon spectrum.

At the next iterative step the calculated multiphonon contributions were subtracted from the initial experimental spectrum, and the result was accepted as a new one-phonon spectrum (in the energy range 2–160 meV). Convergence was achieved in three iterations.

The results of the calculation are shown in figure 1, where the contributions from the multiphonon neutron scattering are plotted as a broken curve and the difference between the experimental and multiphonon spectra is drawn as a full curve.

3.2. *Hydrogen optic modes*

For the sake of quantitative comparison, the fundamental hydrogen peak in the γ-ZrH spectrum was treated as a sum of three Gaussians (short-dash broken curve in figure 2). The parameters of the fitted Gaussians are listed in table 1. The table also includes similar data for the γ-ZrD spectrum measured at TFXA [1]. It follows from the data that ratios $\omega_i^{\mathrm{H}}/\omega_i^{\mathrm{D}}$ for all three components of the peaks are smaller than $\sqrt{m_{\mathrm{D}}/m_{\mathrm{H}}}=\sqrt{2}$, as should be the case for a harmonic oscillator. This deviation from the square-root mass ratio is indicative of anharmonicity of H(D) vibrations in γ-ZrH(D), and it is of nearly the same magnitude as for titanium monohydride, γ-TiH(D) [6–8].

Many INS experiments were performed with the other phases of the Zr–H system. A very broad peak due to hydrogen vibrations has been observed on HCP α-ZrH_y, $y=0.03$–0.05, at an energy of 143–144 meV [12, 13]. The FCC δ phase in ZrH_y, $0.54\leqslant y\leqslant 1.56$, showed a broad peak at 130–140 meV [14–20]. The FCT ε-ZrH_y, $1.9\leqslant y\leqslant 2$, had a split peak with maxima at energies 136–138 meV and 143–145 meV and with a high-energy shoulder at 154 meV [19–21]. The shoulder was related to the multiphonon processes which combined optical and acoustic vibration [21]. Thus, the optical peak in the γ phase has the highest energy compared to the other phases of the Zr–H system. This is systematically related to the metal-to-hydrogen distances in zirconium hydrides. The distance in the γ phase

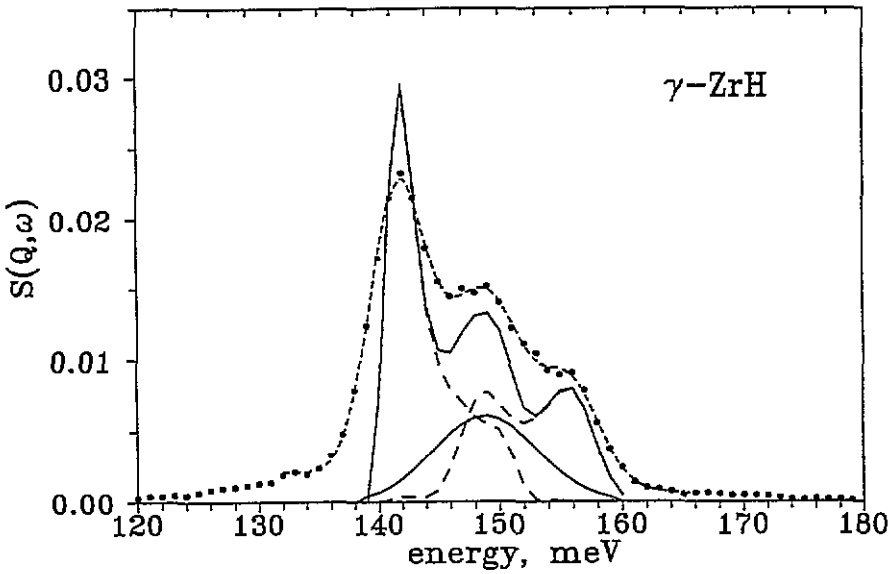

Figure 2. Experimental (points) and calculated (top full curve) $S(Q,\omega)$ spectra of the γ phase in the range of hydrogen optical modes (calculated multiphonon contributions are subtracted from the experimental data). The calculated spectrum was convoluted with the model resolution function of the TFXA spectrometer (a triangle with a width at half-maximum of $\Delta E = 0.02\omega$). The contributions to the calculated spectrum from vibrations of H atoms in the *ab* plane and along the *c* axis are shown as long-dash broken curves (left and split right peaks, respectively). The peak below (full curve) represents the states that form bound multiphonon states.

Table 1. Peak positions, ω_i (meV), full widths at half-maximum, δ_i (meV), and peak amplitudes, H_i (arbitrary units), of Gaussians that describe the H and D optical bands in the INS spectra of γ-ZrH (present data) and γ-ZrD [1]. The line $\omega_i^{\mathrm{H}}/\omega_i^{\mathrm{D}}$ shows deviation from the harmonic value $\sqrt{m^{\mathrm{D}}/m^{\mathrm{H}}} = \sqrt{2}$.

	γ-ZrH			γ-ZrD		
	$i=1$	$i=2$	$i=3$	$i=1$	$i=2$	$i=3$
ω_i	141.6	148.8	156.0	103.4	108.0	112.7
$\omega_i^{\mathrm{H}}/\omega_i^{\mathrm{D}}$	1.37	1.38	1.38			
δ_i	5.5	7.8	5.4	4.4	4.9	4.8
H_i	0.50	0.33	0.16	0.37	0.27	0.20

is $R_{\mathrm{Zr-D(H)}} = 2.041$ Å [1], but increases to 2.070 Å and 2.082 Å in the δ and ε phases, respectively [2].

Another dependence of the hydrogen optical frequency is observed for α and γ phases. The interatomic distance in the α phase, $R_{\mathrm{Zr-H(D)}} = 2.011$ Å at 873 K [2], is shorter than in γ-ZrH, but the energy of hydrogen vibrations is lower than in the γ phase.

The $\omega(R_{\mathrm{M-H}})$ dependence in other M–H systems is usually described by the $1/R^n$ law, where $1 \leqslant n \leqslant 2$ [22–26]. This law is also valid for the series of α-ZrH_y, δ-ZrH_y and ε-ZrH_y. The $\omega(R_{\mathrm{Zr-H}})$ behaviour becomes anomalous when γ-ZrH is included in the series. This indicates that the potential for hydrogen atoms in the γ-ZrH is steeper than in any other Zr–H phase.

The structure of the optical band in the γ-ZrH spectrum is very similar to that in γ-ZrD [1]. A good description of the γ-ZrD optical band was given within the Born–von Kármán model [1]. A similar calculation was carried out here for γ-ZrH on the basis of γ-ZrD interatomic force constants.

Each pairwise interaction was described with two parameters, i.e. the longitudinal (L) and transverse (T) force constants. Five kinds of pairs were involved in the calculation, i.e. the nearest Zr–Zr and Zr–D atoms and the first-, second- and third-nearest D–D neighbours. The interatomic distances for the D–D pairs were $c/2$ along the crystal c-axis, $\sqrt{a^2+b^2}/2$ in the ab plane and $\sqrt{a^2+b^2+c^2}/2$ in the (111) direction, respectively. The interatomic force constants used in this work are based on those obtained for γ-ZrD [1], but adapted to the Zr–H system. The Zr–H interaction determines the average energy of hydrogen vibrations. It was necessary, therefore, to take into account the observed anharmonicity of the H(D) vibrations. The energies of the main features in the peak of H(D) vibrations in the experimental spectra relate as $\omega_1^{\mathrm{H}}/\omega_1^{\mathrm{D}} \simeq 1.37$ (table 1) rather than $\sqrt{2}$ required for a harmonic crystal. Since force constants are proportional to ω^2, the Zr–H and Zr–D force constants should relate as $(1.37/\sqrt{2})^2 \simeq 0.94$. Therefore, the Zr–D force constants were reduced in the present calculation by a factor of 0.94. The total set of model constants is given in table 2.

Table 2. The longitudinal (L) and transverse (T) force constants (in $\mathrm{N\,m^{-1}}$) in the Born–von Kármán model calculations.

	First neighbour		Second neighbour		Third neighbour	
	L	T	L	T	L	T
H–H = D–D	3.0	1.5	−1.5	0.	1.0	0.
Zr–H = 0.94× (Zr–D)	29.5	14.8				
Zr–Zr	8.0	0.				

The UNISOFT program [27] was used for the calculations. The weighted densities of phonon states were obtained according to

$$G_i(\omega) = \frac{1}{3Nm_i}\sum_{j,q}|e(i|qj)|^2\delta(\omega-\omega_j(q)) \tag{1}$$

where $\omega_j(q)$ and $e(i|qj)$ are eigenvalues and eigenvectors of the dynamical matrix corresponding to the phonon state qj, and m_i is the mass of atom i. The summation runs over $N = 1728$ points in the q-space distributed uniformly over the reduced Brillouin zone. To compare with the experimental spectrum, we transformed the calculated data to

$$S(Q,\omega) = (\hbar Q^2/6\omega)\sum_i \exp(-2\mathrm{DW}_i)\sigma_i G_i(\omega)[n(\omega)+1] \tag{2}$$

where Q is the neutron momentum transfer, DW_i is the Debye–Waller factor of atom i, σ_i is the neutron scattering cross section of atom i, and $n(\omega)$ is the Bose factor.

The calculated $S(Q,\omega)$ spectrum of γ-ZrH is represented by the top full curve in figure 2. It fits the experimental points with reasonable accuracy. The contribution to the calculated spectrum from H atoms which vibrate in the ab-plane (the left peak) and along the c-axis (the split peak at the right) are shown in figure 2 as long-dash broken curves.

The good correspondence between the calculated and experimental spectra for γ-ZrH as well as for γ-ZrD [1] proves that the force constants both of the H–H interaction and of the D–D interaction are actually the same, in spite of anharmonic behaviour of H(D) vibrations.

It is interesting to compare the optical phonon band of γ-ZrH with the impurity hydrogen vibrations in γ-ZrD (figure 3). A hydrogen impurity of about 0.9% was found in the previous study on γ-ZrD [1]. This impurity hydrogen resulted in a narrow split peak in the γ-ZrD INS spectrum (full points and the broken curve). It was assumed from the intensity distribution and the small width of the peak that the impurity hydrogen vibrations should be discussed in terms of local oscillators rather than optical phonon modes. Two maxima of the split hydrogen peak in the INS spectrum of γ-$ZrD_{0.991}H_{0.009}$ were observed at 147.2 and 154.3 meV [1]. The values of the first H and D optic peaks in the INS spectrum of γ-$ZrD_{0.991}H_{0.009}$ exactly follow the harmonic behaviour. The dispersive optic phonon band in γ-ZrH is very different from the impurity hydrogen peak (figure 3). The average energy of the impurity peak in γ-ZrD is higher than that of the γ-ZrH optic band. This is indicative of larger force constants for the Zr–H interaction in γ-ZrD than in γ-ZrH. Thus, it can be concluded that the pair potential for the Zr–H interaction in the γ phases is somewhat different for zirconium hydride and deuteride.

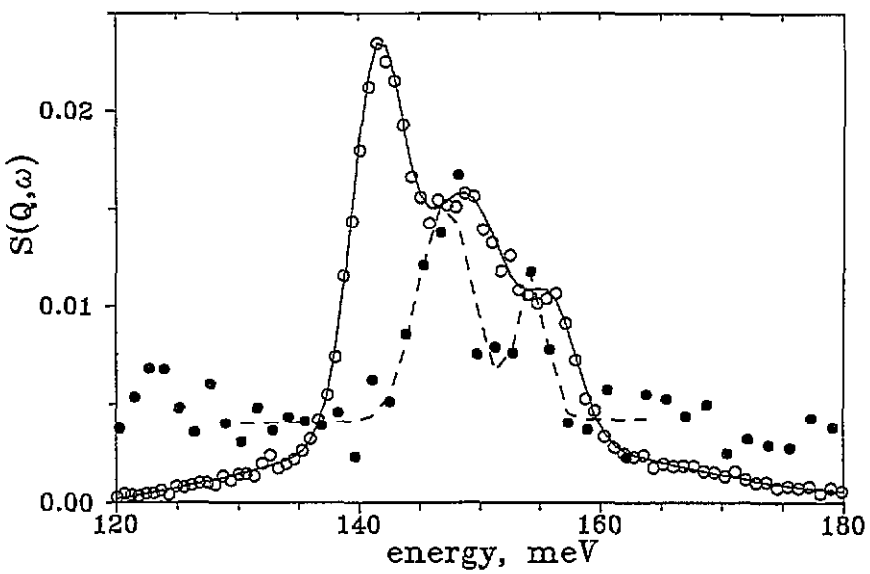

Figure 3. Experimental $S(Q,\omega)$ spectra of γ-ZrH (open points) and γ-$ZrD_{0.991}H_{0.009}$ (full points) [1] in the range of hydrogen optical modes.

3.3. Lattice vibrations

Figure 4 shows the generalized vibrational densities of states $\Theta(\omega)$ in the range 0–30 meV as obtained from the experimental (points) and calculated (full curve) $S(Q,\omega)$ spectra according to

$$\Theta(\omega) = \frac{\exp(2\mathrm{DW})S(Q,\omega)\omega}{Q^2[n(\omega)+1]}. \tag{3}$$

The density of phonon states of α-Zr at room temperature [28] is also presented in figure 4 (short-dash broken curve at the bottom). This density of states is normalized under the assumption that 32% of the content of our sample consist of the α phase, and Zr atoms in both α and γ phases show the same efficiency of neutron scattering. In spite of the rather crude fit of the Zr–Zr force constants for γ-ZrD [1], their use in the present calculations also gives a fairly good agreement with the experiment in the lattice part of the γ-ZrH spectrum.

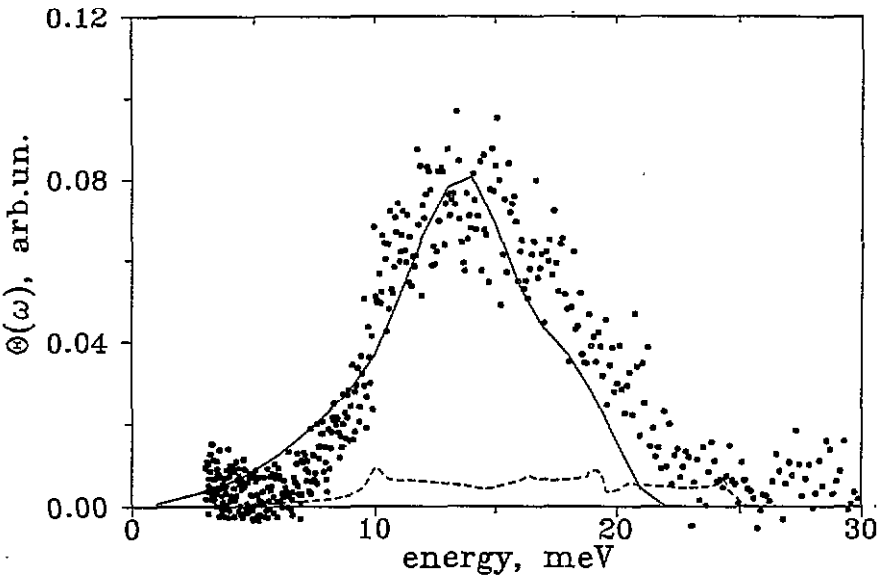

Figure 4. Generalized vibrational densities of states, $\Theta(\omega)$, of $(\alpha+\gamma)$-$ZrH_{0.68}$ in the range of lattice vibrations. Experimental points were calculated from the measured $S(Q,\omega)$ spectrum using (3). The calculated $\Theta(\omega)$ spectrum of γ-ZrH (present work) and the density of phonon states of α-Zr [28] are shown as full and broken curves, respectively.

The calculated generalized vibrational density of states of γ-ZrH in the range of lattice vibrations is compared to that of γ-ZrD in figure 5 (full curves), where both spectra are normalized to unity. There is an evident difference between the spectra. Partial $\Theta(\omega)$ spectra for zirconium atoms in both γ-ZrH and γ-ZrD are the same, and partial $\Theta(\omega)$ for H and D atoms are identical. But $\Theta(\omega)$ for Zr atoms essentially differs from that for H atoms.

Then different contributions from the partial $\Theta(\omega)$ for Zr (short-dash broken curves) and H or D (long-dash broken curves) atoms result in different total spectra. The contribution from Zr atoms dominates in the γ-ZrD spectrum because the weighted density of phonon states for Zr atoms is larger than for D (as well as for H) atoms. But the relation is opposite for γ-ZrH due to the large neutron scattering cross section of H atoms compared to those of Zr atoms.

The obtained ratio of the partial integrated intensities for the lattice part of the $\Theta(\omega)$ spectra for the H and Zr atoms was used for the multiphonon calculations in the section 3.1.

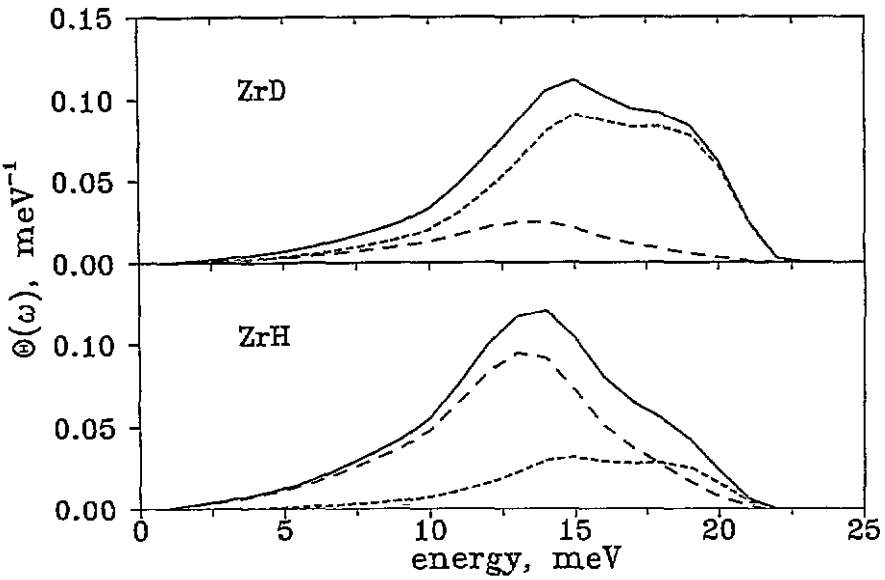

Figure 5. Calculated generalized vibrational densities of states $\Theta(\omega)$ (full curves) for γ phases of ZrH and ZrD in the range of lattice vibrations. The contributions to the spectra from the Zr and H(D) atoms are shown by short-dash and long-dash broken curves, respectively.

3.4. The range of multiphonon scattering

The calculated multiphonon spectrum in figure 1 describes only parts of the experimental data. There are some strong features that remain unattributed in the harmonic approximation. They are clearly seen in the difference curve between the experimental spectrum and the calculated multiphonon contributions (full curve in figure 1). They appear as a peak or a broader band at an energy below a harmonic band followed by a negative peak, i.e. the intensity deficit in the harmonic band of multiphonon scattering. This is further evidence of the essential anharmonicity of γ-ZrH.

The nature of equivalent such extra peaks in γ-TiH(D) and γ-ZrD has been treated in terms of the strong interaction between optical phonons [1, 6–8]. It has been shown theoretically [9, 29–31] that the strong phonon interaction can result in bound multiphonon states (biphonons and triphonons) which do not occur in a harmonic crystal. Such a quasi-particle is characterized by the appropriate energy and wavevector, similar to phonons. The

theory gives a simple relationship between the energies of biphonon and triphonon states and the anharmonicity parameters A and $\tilde{A}$ which determine the strength of the two- and three-phonon interaction [29–31]:

$$E_2 = 2\omega - 2A \qquad E_3 = 3\omega - 6(A + \tilde{A}) \tag{4}$$

where ω is the energy of optical phonons. There is some uncertainty in the value of the energy of the one-phonon mode, ω, because the experimental optic band is rather broad and structured.

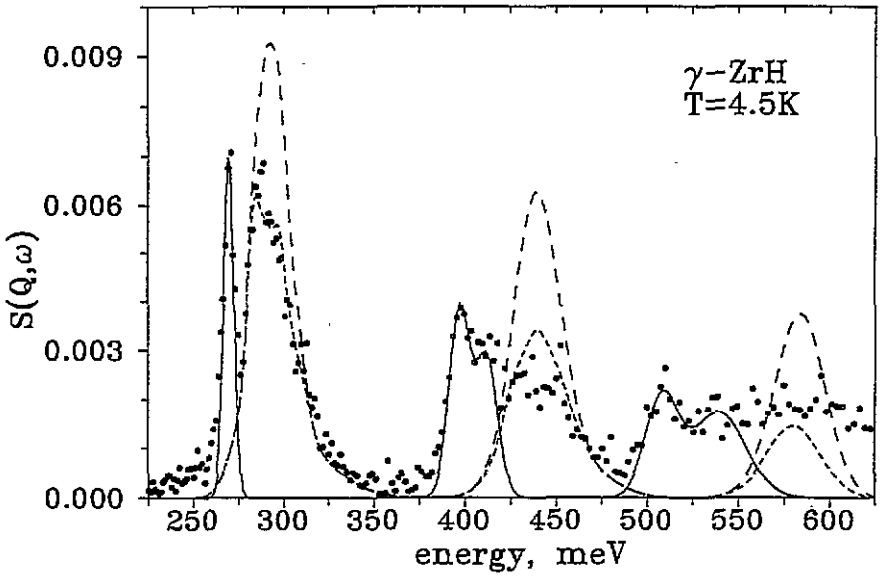

Figure 6. The high-energy range of the INS spectrum of γ-ZrH. Experimental data are shown as points. The long-dash broken curve represents the multiphonon contribution calculated in the harmonic approximation using the experimental one-phonon spectrum in the range 2–160 meV. The short-dash broken curve represents the multiphonon contribution calculated from the one-phonon spectrum with the subtracted 'anharmonic part' (see text). The full curve shows the fit with Gaussians describing the bound multiphonon bands.

The energies of bound multiphonons in γ-ZrH were determined from the positions of extra peaks in the spectrum (figure 6). Several combinations of phonon states can originate at three- and four-phonon neutron scattering when phonon binding is taken into account. Therefore, the anharmonic bands of three- and four-phonon scattering were represented as sums of two Gaussian peaks. The energies and the full widths at half maximum (FWHM, in brackets) of the attributed extra peaks are $E_2 = 269.7$ (6.7), a biphonon; $E_3 = 397$ (13.3), a triphonon, and $E_2 + \omega = 412$ (14.2), a combination of a biphonon and a phonon; $E_4 = 508$ (21), a tetraphonon, and ($E_3 + \omega$ and $2 \times E_2$) = 539 (35), a triphonon plus phonon and two biphonon excitations (all values are in meV). It is worth emphasizing that the bound tetraphonon is observed as a rather distinct peak in the spectrum. But we did

not attempt to give an accurate description of all four-phonon features. For example, a biphonon plus two phonons combination should noticeably contribute to the spectrum at $E_2 + 2\omega \simeq 553$ meV. Data treatment at these energies, however, was troubled due to low statistics of the spectrum, overlapping of the peaks, low spectrometer resolution at energies above 500 meV and the necessity to take into account five-phonon (four optic plus acoustic) contributions.

However, it can be seen from the calculated multiphonon spectrum in figure 1 that this spectrum gives a very good description of the left and right sides of the free two-phonon band as well as of the right side of the three-phonon band. However, there is a poor correspondence between the experimental and calculated intensities in the middle parts of these bands. Rather symmetrical negative peaks occur in the difference curve in these intervals (figure 1). The energies of the minima of the negative peaks are close to multiples of the centre of the second Gaussian, ω_2, in figure 2. We suppose therefore that the bound multiphonon states are due to binding of the 'anharmonic modes' whose energies are about ω_2.

To test this assumption we attempted to describe the harmonic multiphonon bands using a modified one-phonon band. A Gaussian peak was subtracted from the one-phonon spectrum, which was centred at an energy ω close to ω_2. The residual spectrum was used to repeat calculations of the multiphonon spectrum in the harmonic approximation. The best agreement was obtained when the subtracted Gaussian peak was centred at $\tilde{\omega} = 149$ meV and had FWHM = 10 meV, its intensity being 21% of the total intensity of the fundamental band (lower full curve in figure 2). The free two-phonon band thus calculated (short-dash broken curve in figure 6) described the experimental points with good accuracy. There is also fairly good agreement for the free three- and four-phonon bands.

The energy value, $\tilde{\omega} = 149$ meV, was used to obtain the γ-ZrH anharmonicity parameters: $A = 14$ meV and $\tilde{A} = -5.7$ meV. The width of the biphonon peak, 6.7 meV, is much lower than the convoluted width of a double-excited 'anharmonic one-phonon peak', 20 meV. This is indicative of a very resonant character of the bound multiphonons.

The outlined procedure of the data treatment was also applied to revise the analysis of INS data measured on γ-ZrD [1]. The 'anharmonic' Gaussian in the γ-ZrD spectrum had a relative intensity of 13% and $\tilde{\omega} = 107$ meV, FWHM = 4 meV. The γ-ZrD anharmonicity parameters, $A = 6.5$ meV and $\tilde{A} = -2.8$ meV, were about half those of γ-ZrH.

The anharmonicity parameters in question are of the same nature as the energy shift in higher harmonics of an anharmonic oscillator. The latter is known to have the $1/m$ dependence. Here m is the mass of the oscillator. The observed isotope dependence of the parameters A and $\tilde{A}$ for γ-ZrH(D) also follows the $1/m$ behaviour.

4. Conclusions and summary

The lattice dynamics of γ-ZrH was studied by INS. The fundamental optical hydrogen peak was observed at an energy higher than in other phases of the Zr–H system. The peak had three maxima at 141.6, 148.8 and 156.0 meV. The phonon spectrum of γ-ZrH was calculated within the Born–von Kármán model, and a good description of the experimental hydrogen optical peak was obtained. It was found that the H–H interaction in γ-ZrH is essentially the same as the D–D interaction in γ-ZrD.

In the high-energy range of the spectrum, peaks were observed below the free multiphonon bands. They were attributed to the bound multiphonon states (biphonons, triphonons, tetraphonons and their combinations) appearing in anharmonic systems.

The multiphonon contributions calculated in the harmonic approximation were compared to the experimental data. It could be estimated thereby which part of the one-phonon spectrum is responsible for the bound multiphonon states. Thus unique values of the biphonon and triphonon binding energies were obtained.

Acknowledgments

We are pleased to thank the SERC for access to the ISIS pulsed neutron source. We thank Professor V G Glebovsky of the ISSP Russian Academy of Sciences, who supplied high-purity zirconium, and Dr G Eckold (Technische Hochschule, Aachen) for providing the UNISOFT program. The research described in this paper was made possible in part by a grant from the International Science Foundation No REP000. One of us (AIK) thanks the Alexander von Humboldt Foundation for the research grant.

References

[1] Kolesnikov A I, Balagurov A M, Bashkin I O, Belushkin A V, Ponyatovsky E G and Prager M 1994 to be published
[2] Zuzek E, Abriata J P, San-Martin A and Manchester F D 1990 *Bull. Alloy Phase Diagrams* **11** 385–95, 2078–80
[3] Balagurov A M, Bashkin I O, Kolesnikov A I, Malyshev V Yu, Mironova G M, Ponyatovskii E G and Fedotov V K 1991 *Sov. Phys.–Solid State* **33** 711–4
[4] Kolesnikov A I, Balagurov A M, Bashkin I O, Fedotov V K, Malyshev V Yu, Mironova G M and Ponyatovsky E G 1993 *J. Phys.: Condens. Matter* **5** 5045–58
[5] Numakura H, Koiwa M, Asano H and Izumi F 1988 *Acta Metall.* **36** 2267–73
[6] Kolesnikov A I, Prager M, Tomkinson J, Bashkin I O, Malyshev V Yu and Ponyatovskii E G 1991 *J. Phys.: Condens. Matter* **3** 5927–36
[7] Kolesnikov A I, Bashkin I O, Malyshev V Yu, Ponyatovsky E G, Prager M and Tomkinson J 1992 *Physica* B **180 & 181** 284–86
[8] Bashkin I O, Kolesnikov A I, Malyshev V Yu, Ponyatovsky E G, Prager M and Tomkinson J 1993 *Z. Phys. Chem.* **179** 335–42
[9] Agranovich V M and Lalov I I 1985 *Sov. Phys.–Usp.* **28** 484–505
[10] Penfold J and Tomkinson J 1986 *Rutherford Appleton Laboratory Internal Report* RAL-86-019
[11] Kolesnikov A I, Natkaniec I, Antonov V E, Belash I T, Fedotov V K, Krawczyk J, Mayer J and Ponyatovsky E G 1991 *Physica* B **174** 257–61
[12] Khoda-Bakhsh R and Ross D K 1982 *J. Phys. F: Met. Phys.* **12** 15–24
[13] Hempelmann R, Richter D and Stritzker B 1982 *J. Phys. F: Met. Phys.* **12** 79–86
[14] Pelah I, Eisenhauter C M, Hughes D J and Palevsky H 1957 *Phys. Rev.* **108** 1091–2
[15] Andresen A, McReynolds A W, Nelkin M, Rosenbluth M and Whittemore W 1957 *Phys. Rev.* **108** 1092–3
[16] Woods A D 1961 *Inelastic Scattering of Neutrons in Solids and Liquids* (Vienna: IAEA) p 487
[17] Whittemore W L 1965 *Inelastic Scattering of Neutrons* (Vienna: IAEA) **2** p 305
[18] Pan S S and Webb F J 1965 *Nucl. Sci. Eng.* **23** 194–7
[19] Couch J G, Harling O K and Clune L C 1971 *Phys. Rev.* B **4** 2675–81
[20] Ikeda S and Watanabe N 1983 *Physica* B **120** 131–5
[21] Tomkinson J, Penfold J and Robertson S T 1989 *Rutherford Appleton Laboratory Internal Report* RAL-89-074
[22] Ross D K, Martin P F, Oates W A and Khoda Bakhsh R 1979 *Z. Phys. Chem.* **114** 221–30
[23] Sugimoto H and Fukai Y 1982 *J. Phys. Soc. Japan* **51** 2554–61
[24] Fukai Y and Sugimoto H 1981 *J. Phys. F: Met. Phys.* **11** L137–9
[25] Rush J J, Udovic T J, Hempelmann R, Richter D and Driesen G 1989 *J. Phys.: Condens. Matter* **1** 1061–70
[26] Hempelmann R, Richter D, Hartmann O, Karlsson E and Wäppling R 1989 *J. Chem. Phys.* **90** 1935–49

[27] Eckold G, Stein-Arsic M and Weber H-J 1986 *UNISOFT—A Program Package for Lattice-Dynamical Calculations: User Manual* (Jülich: IFF KFA) Jül-Spez-366
[28] Stassis C, Zarestky J, Arch D, McMasters O D and Harmon B N 1978 *Phys. Rev.* B **18** 2632–42
[29] Agranovich V M, Dubovskii O A and Orlov A V 1986 *Phys. Lett.* **119A** 83–8
[30] Agranovich V M and Dubovskii O A 1986 *Int. Rev. Phys. Chem.* **5** 93–101
[31] Agranovich V M, Dubovskii O A and Orlov A V 1989 *Solid State Commun.* **70** 675–81

JPEDAV (2006) 27:548-549
DOI: 10.1361/154770306X136638
1547-7037/$19.00 ©ASM International

H-Zr (Hydrogen-Zirconium)

H. Okamoto

The Zr-H phase diagram in [Massalski2] was evaluated by [1990Zuz] (dashed lines in Fig. 1). Intermediate phases δ and ε are shown. [1999Dup] obtained the Zr-H phase diagram by thermodynamic modeling. The result is shown with dotted lines in Fig. 1.

According to pressure-composition isotherm measurement by [2003Set], the Zr-H phase diagram appears as shown with solid lines. Figure 2 shows the (αZr) phase region in detail. The diagrams of [1990Zuz], [1999Dup], and [2003Set] are similar, but refinement seems to be needed due to disagreement among them.

[2003Set] could not observe the change in the isotherms corresponding to the ε phase. Therefore, the existence of the ε phase must be reexamined.

References

1990Zuz: E. Zuzek, J.P. Abriata, A, San-Martin, and F.D. Manchester, The H-Zr (Hydrogen-Zirconium) System, *Bull. Alloy Phase Diagrams,* **11**(4), 1990, p 385-395

1999Dup: N. Dupin, I. Ansara, C. Servant, C. Toffolon, C. Lemaignan, and J.C. Brachet, A Thermodynamic Database for Zirconium Alloys, *J. Nucl. Mater.,* **275**(3), 1999, p 287-295

2003Set: D. Setoyama and S. Yamanaka, Phase Diagram of Zr-O-H Ternary System, *J. Alloys Compd.,* **370,** 2003, p 144-148

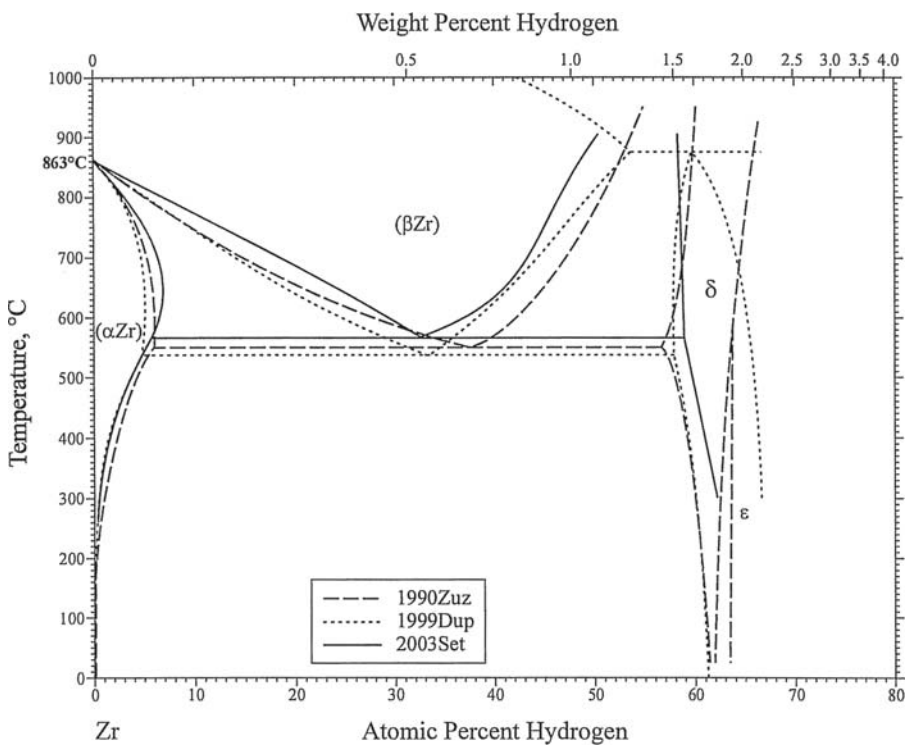

Fig. 1 Zr-H phase diagram

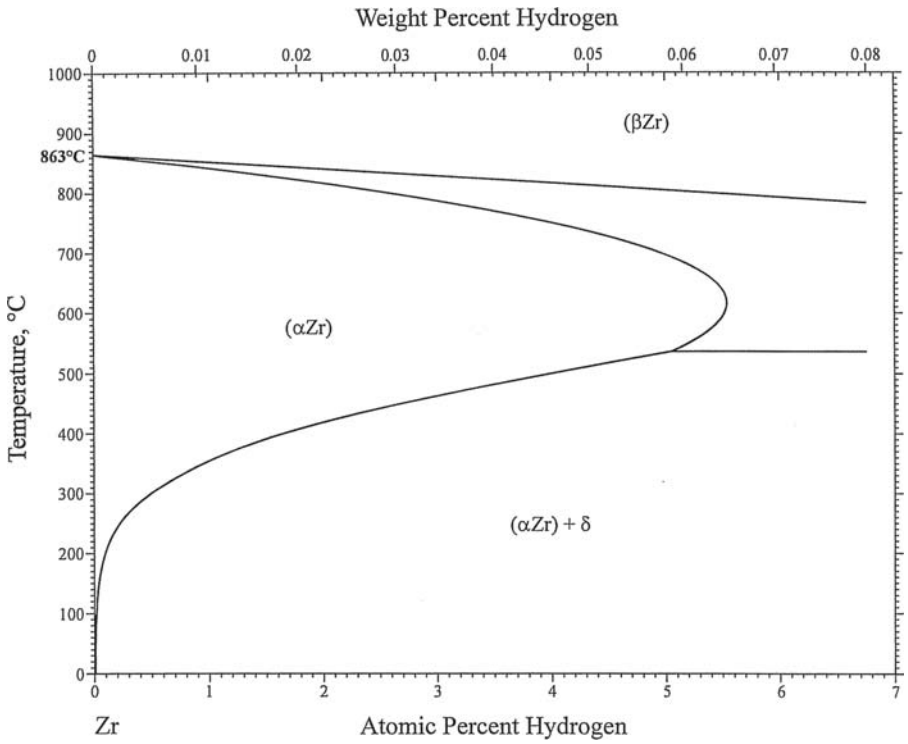

Fig. 2 Detail of the (αZr) phase region

nature COMMUNICATIONS

ARTICLE

Received 6 Jun 2012 | Accepted 4 Sep 2012 | Published 9 Oct 2012

DOI: 10.1038/ncomms2117

Quantum oscillations of nitrogen atoms in uranium nitride

A.A. Aczel[1], G.E. Granroth[1], G.J. MacDougall[1], W.J.L. Buyers[2], D.L. Abernathy[1], G.D. Samolyuk[3], G.M. Stocks[3] & S.E. Nagler[1,4]

The vibrational excitations of crystalline solids corresponding to acoustic or optic one-phonon modes appear as sharp features in measurements such as neutron spectroscopy. In contrast, many-phonon excitations generally produce a complicated, weak and featureless response. Here we present time-of-flight neutron scattering measurements for the binary solid uranium nitride, showing well-defined, equally spaced, high-energy vibrational modes in addition to the usual phonons. The spectrum is that of a single atom, isotropic quantum harmonic oscillator and characterizes independent motions of light nitrogen atoms, each found in an octahedral cage of heavy uranium atoms. This is an unexpected and beautiful experimental realization of one of the fundamental, exactly solvable problems in quantum mechanics. There are also practical implications, as the oscillator modes must be accounted for in the design of generation IV nuclear reactors that plan to use uranium nitride as a fuel.

[1] Quantum Condensed Matter Division, Neutron Sciences Directorate, Oak Ridge National Laboratory, Oak Ridge, Tennessee 37831, USA. [2] Chalk River Laboratories, Canadian Neutron Beam Center, National Research Council, Chalk River, Ontario, Canada K0J 1J0. [3] Materials Science and Technology Division, Physical Sciences Directorate, Oak Ridge National Laboratory, Oak Ridge, Tennessee 37831, USA. [4] CIRE, University of Tennessee, Knoxville, Tennessee 37996, USA. Correspondence and requests for materials should be addressed to A.A.A. (email: aczelaa@ornl.gov) or to S.E.N. (email: naglerse@ornl.gov).

© 2012 Macmillan Publishers Limited. All rights reserved.

The spectrum of elementary excitations in materials is one of the core concepts in modern condensed matter physics. The archetypical example is the set of quantized lattice vibrations in crystalline solids, or phonons[1]. For crystals with more than one atom per unit cell, one expects both acoustic and optic phonon modes and if these are known, one can calculate the lattice contribution to fundamental properties such as the heat capacity. The vibrational spectrum at energies above those of the highest optic phonon mode is generally a complicated many phonon continuum that is often weak and featureless. In sharp contrast, for the binary solid uranium nitride (UN)[2–5], where the nitrogen atoms are very light compared with the uranium atoms, our inelastic neutron-scattering measurements reveal that the high-energy spectrum is greatly simplified and consists of a set of equally-spaced, well-defined modes that can be measured to energies at least ten times as large as that of the optic phonon modes. This data is best explained by assuming that each nitrogen atom behaves as an independent quantum harmonic oscillator (QHO), and the nitrogen motion is therefore a rare experimental realization of an exactly soluble, three-dimensional model in quantum mechanics[6].

The binary uranium systems of the form UX (X = C, N, S, Se, Te, As, Sb) have relatively simple rocksalt crystal structures as illustrated in Fig. 1. They have been extensively studied owing to their vast array of puzzling physical and magnetic properties[7], including unusually high electronic-specific heats and drastic suppression of ordered magnetic moments. Among these systems, UN has received significant attention[8–12] recently owing to its potential use as a high-temperature nuclear fuel[13–15].

The primary magnetic and lattice excitations of UN have been investigated previously via inelastic neutron scattering[2,3,16]. Despite these efforts, several intriguing open questions remain concerning the details of the experimental spectra. Since the initial measurements, significant advances have been made in inelastic neutron scattering using time-of-flight methods. Next-generation chopper spectrometers allow for measurements over much broader energy ($\hbar\omega$) and momentum ($\vec{Q}$) transfer ranges than were previously accessible, with both improved intensity and resolution. For these reasons, the excitations in UN were re-examined using the Fermi chopper spectrometers SEQUOIA[17,18] and ARCS[19] at the Spallation Neutron Source of Oak Ridge National Laboratory. In addition to the expected magnon and phonon modes, this investigation resulted in the unexpected discovery of a series of excitations spaced equally in energy by intervals of ~50 meV, and extending up to at least 500 meV.

Results

Conventional phonons. To perform the measurements, the same UN crystal utilized by Jackman *et al.*[2] was aligned with the (*HHL*) plane horizontal and cooled to a temperature $T = 5$ K. Figure 2a shows representative results obtained at SEQUOIA using an incident neutron energy $E_i = 80$ meV for a typical symmetry direction in reciprocal space. A constant Q-cut through the data, at the position corresponding to the vertical line, is illustrated in Fig. 2b. The solid red curve is a fit to a superposition of Gaussian peaks at the mode positions. The measured phonon dispersion relations are consistent with earlier investigations[2,20]. The black lines in Fig. 2a are obtained from a fit of the data to a simplified model[16] that includes only nearest-neighbour U-N ($65 \pm 2\,\mathrm{N\,m^{-1}}$) and U-U ($50 \pm 4\,\mathrm{N\,m^{-1}}$) force constants. This model suffices for illustrative purposes, although more detailed models[2,8–10,21,22] give a closer match to the observed dispersion. Some of those models also include N-N force constants, although they are found to be negligibly small compared with their U-N and U-U counterparts.

Notably, the optic modes are well separated in energy from the acoustic modes and are weakly dispersive centred around $\hbar\omega$~50 meV[2,20]. Because of the large mass ratio M/m, where M and m are the masses of the U and N atoms, respectively, the eigenvectors of the modes are such that the U atom motions are largely reflected by the acoustic phonons and the optic modes correspond primarily to motions of the N atoms[16]. A weak column of magnetic scattering, previously observed by Holden *et al.*[3], is also visible in Fig. 2a at the antiferromagnetic zone centre (−1 −1 0).

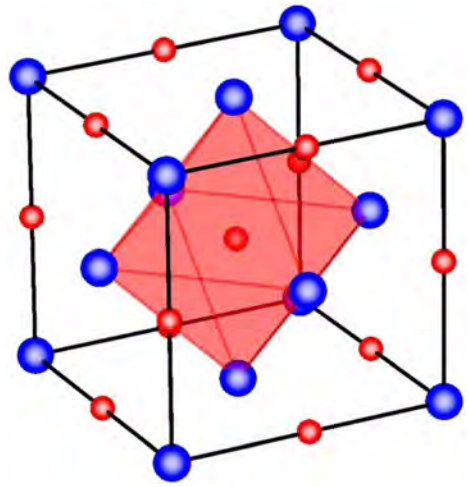

Figure 1 | Rocksalt crystal structure of uranium nitride. Each N atom (small red spheres) is centred in a regular octahedron of U atoms (large blue spheres).

High energy response. The upper and lower panels in Fig. 2c,d show SEQUOIA data taken with $E_i = 250$ meV covering a larger range of energy transfer. The upper panel shows the data averaged over all measured crystal orientations and the lower panel is a plot of intensity versus energy transfer for this data summed over Q. The data is striking and reveals a series of essentially dispersionless excitations extending up in energy from the optic mode, and evenly spaced by ~50 meV intervals. The intensity of each mode increases with increasing momentum transfer over several $\mathrm{Å}^{-1}$ indicating that these excitations are vibrational as opposed to magnetic. These data were extended greatly in both energy and wavevector range by further measurements using the ARCS chopper spectrometer. The larger Q range of this instrument is provided by its wide-angle detector coverage up to 2θ~135°, whereas the maximum 2θ for SEQUOIA is only ~60°. Figure 3a,b show ARCS data with $E_i = 500$ meV plotted on a logarithmic intensity scale. Figure 3c,d show data from the same instrument with $E_i = 800$ meV; the upper panel c has intensity on a linear scale, whereas panel d is also on a logarithmic scale. A series of evenly spaced excitations is clearly visible up to the 10th order at an energy of 500 meV. The well-defined peaks in the orientationally averaged data imply that the modes are localized and isotropic, and the energy widths of these excitations were found to be roughly the same for all orders of n.

QHO model. Some enhanced response at an energy corresponding to twice that of the optic phonon was observed in previous neutron scattering studies of UN and attributed to two-phonon processes[16]. However, the observation of such an extended series of equally spaced and well-defined modes is unprecedented. The most obvious system exhibiting a spectrum consisting of equally spaced modes is the QHO. Here one can postulate that the extremely light mass of the N atom relative to the U atom leads to a situation where high-frequency vibrations in the crystal essentially consist of motions of individual N atoms in a very isotropic and harmonic potential arising from a surrounding regular octahedron of U atoms. Each N atom is then a nearly ideal realization of the QHO in three dimensions, with a fundamental frequency corresponding to an energy

© 2012 Macmillan Publishers Limited. All rights reserved.

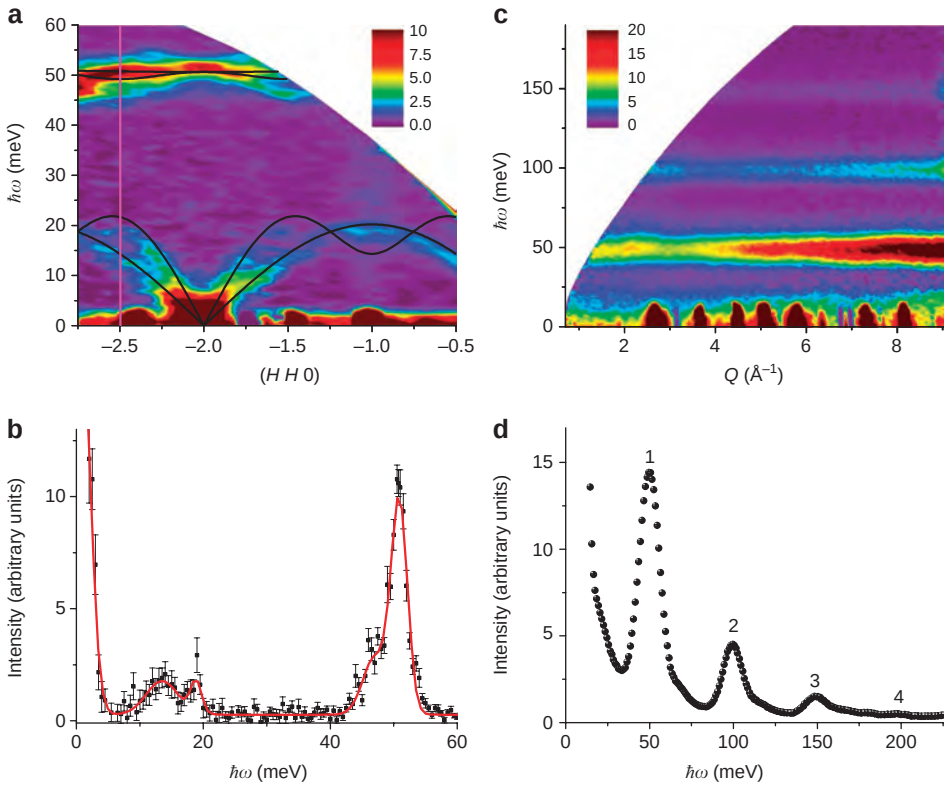

Figure 2 | Inelastic neutron scattering data from UN measured at SEQUOIA for $T = 5$ K. (**a**) Colour intensity plot of the scattering with $E_i = 80$ meV. The vertical axis $\hbar\omega$ denotes the energy transfer, and the horizontal axis the wavevector transfer along high-symmetry direction ($HH0$). The integration ranges for the perpendicular directions ($H\bar{H}0$) and ($00L$) were 0.2 reciprocal lattice units (r.l.u.). The data clearly shows the acoustic and optic one-phonon modes, and the black curves show fits of the phonon dispersion to the two force-constant model described elsewhere[16]. (**b**) A constant Q-cut taken along the vertical line in **a** with an integration range of 0.2 r.l.u. in the ($HH0$), ($H\bar{H}0$) and ($00L$) directions. The error bars represent one standard deviation from the expected signal, and the solid line depicts a fit to a superposition of Gaussian functions. (**c**) Colour intensity plot of the $E_i = 250$ meV data summed over all directions in reciprocal space, with the magnitude of the wavevector, Q, along the horizontal axis. Several modes are evident, evenly spaced in energy by ~50 meV intervals. As discussed in the text, these are attributed to QHO behaviour of the nitrogen atoms in UN. (**d**) Q-integrated data from **c**, clearly showing the oscillator excitations. The error bars, representing one standard deviation from the expected signal, are smaller than the symbols.

$\hbar\omega_o \approx 50$ meV, equivalent to a temperature of 580 K. The QHO is one of the simplest and best understood theoretical models in quantum mechanics[6], and serves as the foundation for understanding diverse phenomena such as the vibrational modes of molecules, the motion of atoms in a lattice and the theory of heat capacity. We show below that the QHO model can quantitatively describe the high-energy vibrational features observed in the UN data.

The neutron-scattering signal expected from the QHO is well known[23]. The dynamical response for $k_B T \ll \hbar\omega_o$ can be written as:

$$S(Q,\omega) = \sum_n S_n(Q,\omega) \tag{1}$$

where the contribution to the intensity arising from the nth oscillator excitation is given by:

$$S_n(Q,\omega) = \frac{1}{n!}\left(\frac{\hbar Q^2}{2m\omega_o}\right)^n \exp\left(\frac{-\hbar Q^2}{2m\omega_o}\right)\delta(\hbar\omega - n\hbar\omega_o) \tag{2}$$

The argument of the exponent resembles a Debye–Waller factor and reflects the zero-point motion of the oscillator. It is interesting to note that the intensity maximum for each mode occurs at the Q position corresponding to the recoil scattering for a free particle of mass m (see Supplementary Discussion Section A and Supplementary Fig. S1 for further details).

Equation (2) reflects the intensity expected for a single inelastic scattering event. As the modes are evenly spaced, in a real experiment multiple scattering events in any combination of elastic and inelastic scattering will also result in intensity at the positions of the modes. Hence, any comparison of the QHO theory to the data must account for the intensity arising from multiple scattering in some fashion. As a first approximation, the measured data for UN was compared with the QHO model by fitting constant energy cuts (20 meV integration range) corresponding to the $n = 1$–7 modes for both $E_i = 500$ meV and 800 meV data to the following functional form:

$$S_n(Q) = A_n Q^{2n} \exp(-CQ^2) + B_n \tag{3}$$

Here the multiple scattering contribution to the observed intensity at each mode position is assumed to be a constant B_n independent of momentum Q: this is the simplest possible assumption. The B_n term and the associated multiple scattering are discussed in more detail in Supplementary Discussion Section B and Supplementary Fig. S2.

Figure 4a shows the Q dependence of the seven lowest oscillator modes for the $E_i = 800$ meV data with solid lines indicating the corresponding fits to equation (3). The fits are excellent over the entire range of measured data and this is also true for the $E_i = 500$ meV data (not shown). Figure 4b plots the ratios of the fitted parameters A_n/A_1 for both data sets. The solid curve

© 2012 Macmillan Publishers Limited. All rights reserved.

NATURE COMMUNICATIONS | DOI: 10.1038/ncomms2117

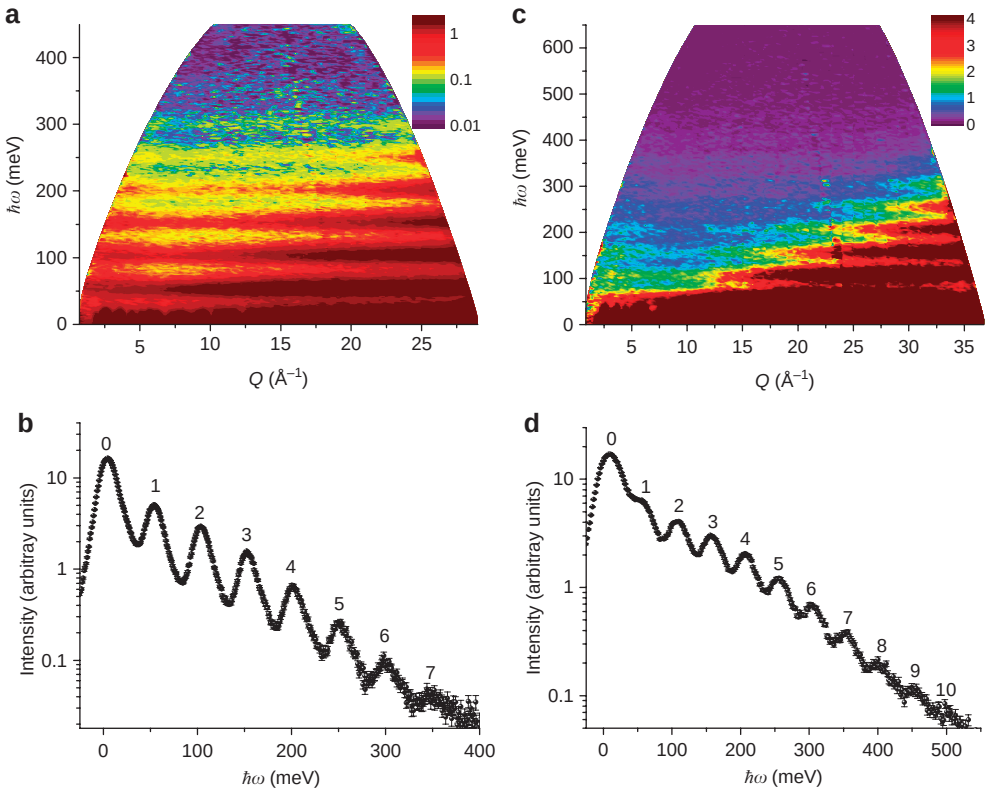

Figure 3 | Inelastic neutron scattering data from UN measured at ARCS for $T = 5$ K. (**a**) Colour intensity plot of the scattering with $E_i = 500$ meV averaged over all measured crystal orientations. (**b**) The scattering in **a** integrated over all Q, with the error bars representing one standard deviation from the expected signal. (**c**) Colour intensity plot of the scattering with $E_i = 800$ meV averaged over all measured crystal orientations. (**d**) The scattering in **c** integrated over all Q, with the error bars representing one standard deviation from the expected signal.

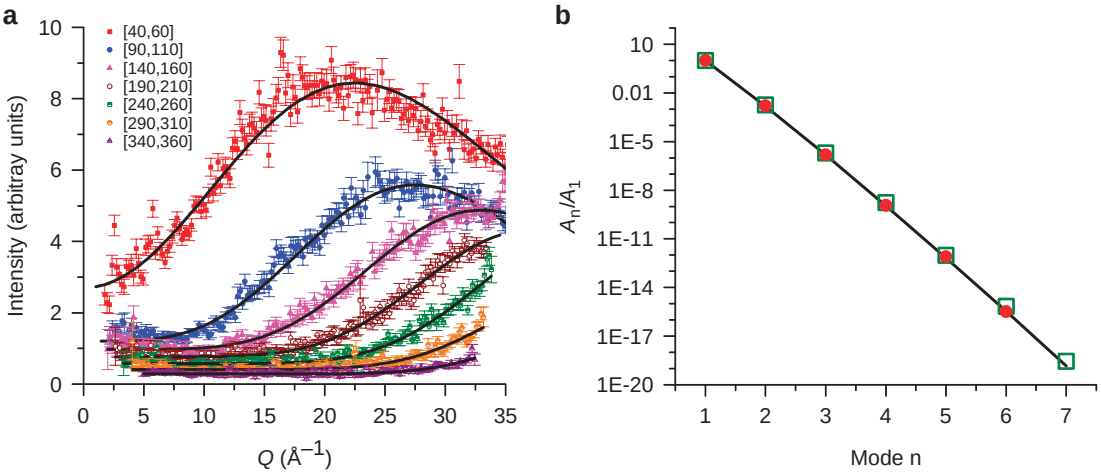

Figure 4 | Fitting results and analysis of the UN oscillator modes. (**a**) The Q-dependence of the intensity for the $n = 1$–7 oscillator modes with $E_i = 800$ meV. The error bars represent one standard deviation from the expected signal, and the legend indicates ranges of integration over energy transfer in meV. The solid lines are fits to the QHO model as described in the text. (**b**) The A_n coefficients for the $n = 1$–7 modes normalized by the values of A_1. The coefficients are extracted from fits to the $E_i = 500$ meV (solid red circles) and 800 meV (open green squares) ARCS data sets, and the error bars, representing one standard deviation, are smaller than the size of the symbols. The solid line is the prediction of the QHO model with $\hbar\omega_o = 50$ meV and m corresponding to the mass of a nitrogen atom. The ratio is plotted on a logarithmic scale and spans almost 20 orders of magnitude.

indicates the prediction of the QHO model for a nitrogen atom with $\hbar\omega_o = 50$ meV, with the non-integer n values interpolated by using $\Gamma(n+1)$ to calculate $n!$. The values obtained from the data agree very well with the model over nearly 20 orders of magnitude. The maximum relative deviation for any one ratio is within a factor of two for the $E_i = 800$ meV data and within 20% for the $E_i = 500$ meV data. Given the large range of values covered and the simple assumption made for the multiple scattering, this is strong confirmation that the QHO picture applies to the nitrogen atoms in the uranium lattice.

© 2012 Macmillan Publishers Limited. All rights reserved.

The parameter C is related to the zero-point energy of the oscillator. For a nitrogen atom in a harmonic potential corresponding to $\hbar\omega_o = 50$ meV, the calculated value of C is 0.003 Å^2. The mean value of C determined from all modes at both incident energies was found to be 0.00275(10) Å^2; this is very close to the calculated value. As a further check, the data for each E_i was analysed using a global fit (see Supplementary Discussion Section B and Supplementary Fig. S3) obtaining values for C of 0.00276(2) Å^2 and 0.00264(2) Å^2 for the $E_i = 500$ meV and 800 meV data sets, respectively, also in good agreement with expectations. The slight discrepancies between the fitted and calculated C values may be due to the simple assumption made for the multiple scattering.

Binary solid model extension. Clearly, the QHO model gives an outstanding description of the data. It should be noted that a calculation of the multiphonon scattering for a single frequency, perfectly dispersionless Einstein model leads to a result that is equivalent to the QHO model[24]. However, the oscillator picture is a simpler and more physically reasonable description for the localized vibrations of N atoms in UN, particularly when one considers that it is not an ideal Einstein solid: the crystalline environment and acoustic modes also affect the scattering. Detailed theoretical predictions exist for the response of a binary harmonic solid consisting of a lattice of diatomic molecules with a light atom of mass m bound to a heavier atom of mass M[25]. In the limit $m \ll M$, appropriate for UN, the finite mass of the U atoms can be accounted for approximately by replacing the delta function in equation (2) with a Gaussian:

$$\exp\left(\frac{-\left(\hbar\omega - n\hbar\omega_o - \frac{\hbar^2 Q^2}{2M}\right)^2}{2\sigma^2}\right) \quad (4)$$

This modification suggests that the oscillator modes should be broadened to a width σ and the position of the nth mode shifted by the uranium recoil to $\hbar\omega = n\hbar\omega_o + \hbar^2 Q^2/2M$. For UN, it is not possible to associate a specific N atom with an individual U atom, nevertheless it is still reasonable to compare the data with the binary solid model. To assess how well this model describes the present data, constant Q-cuts (2 Å^{-1} integration range) from the ARCS $E_i = 500$ meV measurement were fit to a superposition of several Gaussian functions (see Supplementary Fig. S4 for a representative fit). The net result of the fitting shows that the modes have an average intrinsic full-width half-maximum of 26 meV with no systematic behaviour evident as a function of Q or n (see Supplementary Table S1 and Supplementary Fig. S5). The magnitude of the broadening is in agreement with the prediction of the binary solid model[25] that the intrinsic energy width of the $n > 1$ peaks should be of the same order as the bandwidth of the acoustic phonon modes. Inspection of Fig. 2a shows this width to be around 20 meV. Except for a possible small effect on the $n = 1$ mode, the fitting does not reveal a measurable shift of the mode energies as a function of Q. Multiple scattering contributions at the mode positions may mask any shift at higher Q. More details of the binary solid model extension are provided in Supplementary Discussion Section C.

Local potential of the nitrogen atoms. To investigate why the isotropic QHO description is so appropriate for UN, density functional theory (DFT) has been used to calculate the potential energy of the nitrogen atoms relative to their equilibrium positions for displacements along major crystallographic directions. Although DFT often fails to give the true ground state for correlated materials, in fact it has been shown to give a good description of the electronic energies in UN[10]. Moreover, DFT gives highly reliable values for relative energy differences of displaced atoms independent of the precise ground state. The DFT results shown in Fig. 5 verify that the potential is harmonic over a wide energy range, certainly for $E < 1$ eV. At the same time, in this range, the potential energy along different directions is isotropic to within 2%. The *ab-initio* calculations predict an energy spacing for the oscillator modes of 50 meV, corresponding very well to the spacing of the excitations observed in the neutron-scattering measurements.

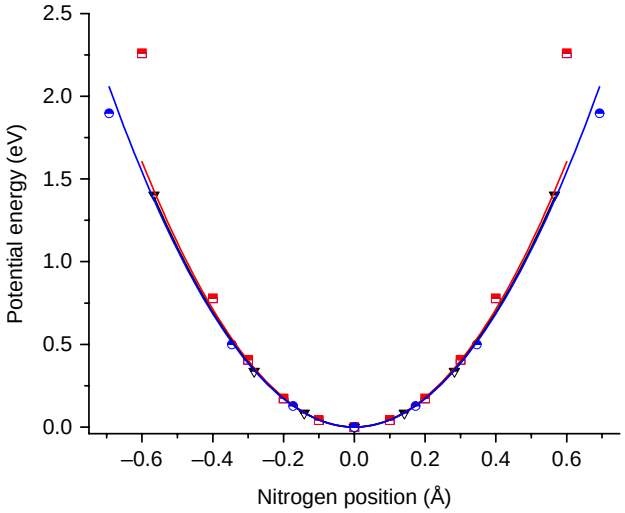

Figure 5 | DFT calculated potential energy of the N atoms in the system UN. The potential energy is shown for atomic displacements relative to the equilibrium position along the [100] (red squares), [110] (black triangles) and [111] (blue circles) directions. The solid lines are fits of the calculated small displacement limit values to parabolic (that is harmonic) potentials. The potential energy is very isotropic and harmonic over a wide range. Deviations are visible above 1 eV, especially along the [100] direction.

Discussion

The QHO behaviour observed here should be visible in many materials where the constituent atoms have greatly different masses. It is also important that there be weak interactions between light atoms sitting in a very harmonic potential. Possible harmonic oscillator behaviour has long been sought and investigated in metallic hydrides, especially for zirconium and titanium systems[26–31]. However, the potentials at the hydrogen sites generally show significant anisotropy or anharmonic effects[32,33]. These features manifest themselves as fine structure and uneven spacing in the hydrogen vibrational modes, and they arise from H–H interactions, crystalline anisotropy and low potential barriers to hopping of the protons. In sharp contrast, the potential at the nitrogen sites of UN is very harmonic and isotropic, leading to evenly spaced nitrogen vibrational modes exhibiting no fine structure within the instrumental energy resolution. To the best of our knowledge, each nitrogen atom in UN is a unique manifestation of a single-atom QHO.

The scattering of neutrons from the oscillator modes may be an important factor in the consideration of UN as a nuclear fuel material. UN has several desirable characteristics for this application, including excellent thermal conductivity and a high melting temperature. For that reason, it is currently under intense consideration for use in proposed Generation IV nuclear reactors[13–15,34], which operate at high temperatures (500–1,000 °C), allowing for improved efficiency in the conversion of heat to electricity.

Nuclear reactor designs require a detailed knowledge of the neutron cross-sections and thermal behaviour of the constituent

© 2012 Macmillan Publishers Limited. All rights reserved.

atoms composing the nuclear fuel. Fermi[35] showed that harmonic oscillations of protons in metals have a significant measurable effect on total neutron cross-sections. In addition to affecting the total cross-section, the oscillator modes in UN could also impact operation via self-moderation of neutrons. The modes will be thermally populated at the proposed Generation IV-operating temperatures and it is necessary to understand if there will be any impact on the thermal conductivity. Given the strong scattering processes shown in the present work, it is clear that the oscillator excitations must be accounted for properly in any detailed Generation IV designs.

Methods

Neutron scattering. For the neutron scattering experiments, the UN single crystal was sealed in an ultrathin Al sample can[36] with He exchange gas and cooled to ~5 K in a closed cycle He refrigerator. For the SEQUOIA[18] measurements, a Fermi chopper with a slit spacing of 3.6 mm and a radius of curvature of 1.53 m was spun at 300 Hz and 360 Hz for $E_i = 80$ meV and 250 meV, respectively, yielding FWHM energy resolutions of 4% and 6% of E_i at the elastic line. The data was accumulated by combining measurements taken with several different incident neutron directions in the [*HHL*] plane. The data from ARCS was obtained using a chopper with an identical radius of curvature and outer dimensions to the SEQUOIA Fermi chopper described above, but with a slit spacing of 0.5 mm. The chopper was spun at 480 Hz ($E_i = 500$ meV) or 600 Hz for ($E_i = 800$ meV) to yield a FWHM energy resolution of 3.5% of E_i at the elastic line. The sample was rotated continuously between the [*HH*0] and [00*L*] directions during data collection. In all measurements, the data was normalized to account for variations of the detector response and solid angle coverage with a vanadium standard. This procedure enabled an accurate determination of the orientationally averaged scattering response. The collection of neutron events is a counting process, therefore we used Poisson statistics for computing uncertainties.

Density functional theory. The electronic structure within the DFT was obtained using the Quantum ESPRESSO package[37]. The calculation was performed using a plane-wave basis set and ultrasoft pseudopotential[38] in a RKKJ scheme[39]. The uranium pseudopotential was obtained from an ionized electronic configuration $6p^6 6d^1 5f^3 7s^1$ with cut-off radii equal to 3.5 atomic units (a.u.), 1.7, 2.6 and 1.6 a.u. for *s*, *p*, *d* and *f* angular momentum. The electronic levels deviate from the all-electron ones by less than 0.1 meV. We used the Perdew, Burke and Ernzerhof[40] exchange-correlation functional. The Brillouin zone (BZ) summations were carried out over a 4×4×4 BZ k-points grid for a supercell containing 64 atoms. The electronic smearing with a width of 0.02 Ry was applied according to the Methfessel–Paxton method. The plane wave energy and charge density cut-offs were 73 Ry and 1054 Ry, respectively, corresponding to a calculation accuracy of 0.2 mRy per atom. The nitrogen atom potential was obtained from the total energy modification of a 2×2×2 supercell when one nitrogen atom was shifted from the equilibrium position in the [100], [110] or [111] directions and the remaining atoms were held fixed in their equilibrium positions.

References

1. Ashcroft, N. & Mermin, D. *Solid State Physics* 451–486 (Holt, Rinehart and Winston, 1976).
2. Jackman, J. A. *et al.* Systematic study of the lattice dynamics of uranium rocksalt-structure compounds. *Phys. Rev. B* **33,** 7144–7153 (1986).
3. Holden, T. M., Buyers, W. J. L., Svensson, E. C. & Lander, G. H. Magnetic excitations in uranium nitride. *Phys. Rev. B* **30,** 114–121 (1984).
4. Solontsov, A. & Silin, V. P. Uranium nitride: a spin polarized weak itinerant electron antiferromagnet with strongly correlated electrons. *Phys. Lett. A* **334,** 453–459 (2005).
5. Samsel-Czekala, M. *et al.* Electronic structure and magnetic and transport properties of single-crystalline UN. *Phys. Rev. B* **76,** 144426 (2007).
6. Shankar, R. *Principles of Quantum Mechanics* 195–231 (Plenum, New York, 1988).
7. Freeman, A. J. & Lander, G. H. (eds) *Handbook on the Physics and Chemistry of the Actinides, Parts I and II* (North-Holland, 1984).
8. Lu, Y., Wang, B.- T., Li, R.- W., Shi, H. & Zhang, P. Structural, electronic and thermodynamics properties of UN: Systematic density functional calculations. *J. Nucl. Mater.* **406,** 218–222 (2010).
9. Modak, P. & Verma, A. K. First principles investigation of electronic, vibrational, elasic, and structural properties of ThN and UN up to 100 GPa. *Phys. Rev. B* **84,** 024108 (2011).
10. Yin, Q. *et al.* Electronic correlation and transport properties of nuclear fuel materials. *Phys. Rev. B* **84,** 195111 (2011).
11. Gryaznov, D., Heifets, E. & Kotomin, E. The first-principles treatment of the electron-correlation and spin-orbital effects in uranium mononitride nuclear fuels. *Phys. Chem. Chem. Phys.* **14,** 4482 (2012).
12. Dubovsky, O. A., Orlov, A. V. & Semenov, V. A. Soliton microdynamics and thermal conductivity of uranium nitride at high temperatures. *Phys. Solid State* **53,** 1963–1974 (2011).
13. Burkes, D. E., Fielding, R. S., Porter, D. L., Meyer, M. K. & Makenas, B. J. A US perspective on fast reactor fuel fabrication technology and experience Part II: ceramic fuels. *J. Nucl. Mater.* **393,** 1–11 (2009).
14. Schriener, T. M. & El-Genk, M. S. Neutronics and thermal-hydraulics analysis of a liquid metal fast reactor for expandable lunar surface power. *Ann. Nucl. Energy* **41,** 48–60 (2012).
15. Petti, D., Crawford, D. & Chauvin, N. Fuels for advanced nuclear energy systems. *MRS Bull.* **34,** 40–45 (2009).
16. Wedgwood, F. A. Actinide chalcogenides and pnictides III: Optic phonon frequency determination in UX and ThX compounds by neutron scattering. *J. Phys. C: Solid State Phys.* **7,** 3203–3218 (1974).
17. Granroth, G. E., Vandergriff, D. H. & Nagler, S. E. SEQUOIA: A fine resolution chopper spectrometer at the SNS. *Physica B* **385–386,** 1104–1106 (2006).
18. Granroth, G. E. *et al.* SEQUOIA: A newly operating chopper spectrometer at the SNS. *J. Phys.: Conf. Ser.* **251,** 012058 (2010).
19. Abernathy, D. L. *et al.* Design and operation of the wide angular-range chopper spectrometer ARCS at the Spallation Neutron Source. *Rev. Sci. Instr.* **83,** 015114 (2012).
20. Dolling, G., Holden, T. M., Svensson, E. C., Buyers, W. J. L. & Lander, G. H. in *Phonons: Proceedings of the International Conference on Lattice Dynamics Paris, 5-7 Sept. 1977*, (ed Balkanski M) 81–89 (Flammarion, Paris, 1978).
21. Jha, P. K. & Sanyal, S. P. Lattice dynamics of uranium chalcogenides and pnictides. *Phys. Rev. B* **46,** 3664–3667 (1992).
22. Jha, P. K. & Sanyal, S. P. Lattice vibrational properteis of uranium pnictides. *Pramana J. Phys.* **42,** 9–14 (1994).
23. Lovesey, S. W. *Theory of Neutron Scattering from Condensed Matter,* Volume 1 86–93 (Oxford University Press, 1986).
24. Izyumov Yu, A. & Chernoplekov, N. A. *Neutron Spectroscopy* 322–358 (Plenum, 1994).
25. Warner, M., Lovesey, S. W. & Smith, J. The theory of neutron scattering from mixed harmonic solids. *Z. Phys. B* **51,** 109–126 (1983).
26. Andresen, A. F., McReynolds, A. W., Nelkin, M., Rosenbluth, M. & Whittemore, W. Neutron investigation of optical vibration levels in zirconium hydride. *Phys. Rev.* **108,** 1092–1093 (1957).
27. Whittemore, W. L. & McReynolds, A. W. Effects of chemical binding on the neutron cross section of hydrogen. *Phys. Rev.* **113,** 806–808 (1959).
28. Kolesnikov, A. I. *et al.* Transfer of hydrogen to octahedral lattice positions in the superconducting titanium hydride phase. *JETP Lett.* **44,** 509–511 (1986).
29. Kolesnikov, A. I. *et al.* Strong anharmonic H(D) vibrations in the δ-phase of titanium hydride: observation of bound multiphonon states. *Physica B* **180–181,** 284–286 (1992).
30. Kolesnikov, A. I., Bashkin, I. O., Belushkin, A. V., Ponyatovsky, E. G. & Prager, M. Inelastic neutron scattering study of ordered γ-ZrH. *J. Phys. Cond. Matt.* **6,** 8989–9000 (1994).
31. Ikeda, S. & Watanabe, N. Local modes and hydrogen potentials in metal hydrides,. *J. Phys. Soc. Jpn.* **56,** 565–576 (1987).
32. Couch, J. G., Harling, O. K. & Clune, L. C. Structure in the neutron scattering spectra of zirconium hydride. *Phys. Rev. B* **4,** 2675–2681 (1971).
33. Elsasser, C., Schweizer, S. & Fahnle, M. Hydrogen vibration in cubic dihydrides MH_2 (M=Ti, Zr) and localization in cubic Laves phases $ZrM_2H_{1/2}$ (M=V, Cr, Fe, Co). *Mat. Res. Soc. Symp. Proc.* **453,** 221–226 (1997).
34. Butler, D. Nuclear power's new dawn. *Nature* **429,** 238–240 (2004).
35. Fermi, E. On the motion of neutrons in hydrogenous substances. *Ric. Scient.* **7,** 13–49 (1936).
36. Stone, M. B., Loguillo, M. J. & Abernathy, D. L. Ultrathin aluminum sample cans for single crystal inelastic neutron scattering. *Rev. Sci. Instrum.* **82,** 055117 (2011).
37. Giannozzi, P. *et al.* QUANTUM ESPRESSO: a modular and open-source software project for quantum simulations of materials. *J. Phys. Cond. Matt.* **21,** 395502 (2009).
38. Vanderbilt, D. Soft self-consistent pseudopotentials in a generalized eigenvalue problem. *Phys. Rev. B* **41,** 7892–7895 (1990).
39. Rappe, A. M., Rabe, K. M., Kaxiras, E. & Joannopoulos, J. D. Optimized pseduopotentials. *Phys. Rev. B* **41,** 1227–1230 (1990).
40. Perdew, J. P., Burke, K. & Ernzerhof, M. Generalized gradient approximation made simple. *Phys. Rev. Lett.* **77,** 3865–3868 (1996).

Acknowledgements

We acknowledge A.I. Kolesnikov, J. Carpenter, E. Iverson and R.J. McQueeney for useful discussions, and A.T. Savici, T.E. Sherline and M.J. Loguillo for technical support. This research was supported by the US Department of Energy, Office of Basic Energy Sciences. A.A.A., G.E.G., G.J.M., D.L.A. and S.E.N. were supported by the Scientific User Facilities Division. G.D.S. and G.M.S. were supported by the Center for Defect Physics and Energy Frontier Research Center. Experiments were

© 2012 Macmillan Publishers Limited. All rights reserved.

performed at the Spallation Neutron Source, which is sponsored by the Scientific User Facilities Division.

Author contributions

A.A.A., G.E.G., G.J.M., W.J.L.B., D.L.A. and S.E.N. participated in the neutron scattering experiments. The density functional theory calculations were performed by G.D.S. and G.M.S. The manuscript was written by A.A.A. with substantial input from G.E.G. and S.E.N. Critical manuscript comments were provided by all authors.

Additional information

Supplementary Information accompanies this paper at http://www.nature.com/naturecommunications

Competing financial interests: The authors declare no competing financial interests.

Reprints and permission information is available online at http://npg.nature.com/reprintsandpermissions/

How to cite this article: Aczel A. A. *et al.* Quantum oscillations of nitrogen atoms in uranium nitride. *Nat. Commun.* 3:1124 doi: 10.1038/ncomms2117 (2012).

© 2012 Macmillan Publishers Limited. All rights reserved.